Doctoral Thesis

High Performance Semitransparent Organic Solar Cells: Materials and Device Design

Hye Rim Yeom

Department of Energy Engineering
(Energy Engineering)

Graduate School of UNIST

2020

High Performance Semitransparent Organic Solar Cells: Materials and Device Design

Hye Rim Yeom

Department of Energy Engineering
(Energy Engineering)

Graduate School of UNIST

High Performance Semitransparent Organic Solar Cells: Materials and Device Design

A thesis/dissertation
submitted to the Graduate School of UNIST
in partial fulfillment of the
requirements for the degree of
Doctor of Philosophy

Hye Rim Yeom

06 / 11 / 2020 of submission

Approved by

Advisor
Jin Young Kim

High Performance Semitransparent Organic Solar Cells: Materials and Device Design

Hye Rim Yeom

This certifies that the thesis/dissertation of Hye Rim Yeom is approved.

06 / 11 / 2020 of submission

signature

Advisor: Jin Young Kim

signature

Tae-Hyuk Kwon: Thesis Committee Member #1

signature

Myoung Hoon Song: Thesis Committee Member #2

signature

Jung Hwa Seo: Thesis Committee Member #3

signature

Dong Suk Kim: Thesis Committee Member #4;

Abstract

Semitransparent organic solar cells (STOSCs) combine the benefits of visible light transparency with light-to-electrical energy conversion. One of the greatest potential applications for STOSCs is their integration into windows and skylights in energy-sustainable buildings. In order to realize this application, we need to study both performance and aesthetic aspects of these solar cells.

So, in this study, we firstly have made various efforts to improve the performance of organic solar cells. i) We have comprehensively studied the effect of various solvent additives (1,8-octanedithiol (ODT), 1,8-diiodooctane (DIO), diphenylether (DPE) and 1-chloronaphthalene (CN)) on the BHJ PSCs based on TQ1:$PC_{71}BM$. And we have found that the addition of 5% CN leads to smoother films, less heterogeneous surface features, and well-distributed TQ1:$PC_{71}BM$ phases, resulting in more balanced charge transport in the devices and a highly efficient power conversion efficiency (PCE) of 7.08%. ii) We have studied about two new polymers incorporating either phenothiazine or its oxidized analogue phenothiazine-S,S dioxide as the donor and benzothiadiazole as the acceptor, namely PPTDTBT and PPTDTBT-SS, respectively. We found that PSCs based on PPTDTBT in a conventional architecture can reach higher PCE, whereas the utilization of its oxidized form, PPTDTBT-SS, in inverted solar cells shows improved performance, when compared to conventional devices. The results obtained here are very helpful for molecular design strategies aimed at creating inverted solar cells with higher device performance. iii) We have researched a p-type photoactive material that replaces thiophenes to selenophene units in PCDTBT, inducing a lower bandgap (1.70 eV) than that of PCDTBT (1.85 eV), while the ideal HOMO energy level (−5.40 eV) is still maintained. Another notable finding comes from our observation of PCDSeBT with a relative wider absorption band, as a result of strong intermolecular Se···Se interactions. This work has provided a feasible strategy for selective fine-tuning of LUMO levels by achieving a high J_{SC} value, while mostly keeping a high V_{OC}. iv) We have studied about the finding optically advantageous metal electrodes for organic solar cells. The reflectivity of each metal electrode was found to considerably influence the light harvesting within the active layer. This study provides guidelines and rational for the selection of appropriate top electrodes in future PSC devices. In addition, the optical properties of each metal were contributed to design the semitransparent electrodes.

Next, we have demonstrated an efficient strategy to achieve high-quality and colorful semitransparent organic solar cells (STOSCs) using Fabry-Pérot etalon-type electrodes composed of an Sb_2O_3 cavity layer and two thin Ag mirrors. This type of Sb_2O_3-based metal/dielectric/metal (MDM) electrode can be deposited by thermal evaporation and can function effectively as both a top conducting electrode and a color filter. By varying the thickness of the Sb_2O_3 layer, the color of the electrodes can be easily and accurately tuned throughout the visible spectrum.

And then, we found colorful (red, green, blue) organic active materials with combinations of various donors and acceptors.

Finally, with the dual-function electrodes, we achieved efficient STOSCs with vivid colors and natural transparency. To achieve saturated colors and low photocurrent losses, active layer materials were selected such that their transmittance peaks matched the transmittance maxima of the electrodes. These strategies for colorful STOSCs enable high performance colorful semitransparent organic solar cells to be realized.

Table of Contents

List of Figures

List of Tables

List of Abbreviations

Abbreviation	Description
FIR	far infrared
UV	ultraviolet
AM	air mass
OSC	organic solar cell
HOMO	highest occupied molecular orbital
LUMO	lowest unoccupied molecular orbital
BIPV	building-integrated photovoltaic
PVSCs	perovskite solar cells
STOSCs	semitransparent organic solar cells
PCE	power conversion efficiency
BHJ	bulk-heterojunction
HTL	hole transport layer
ETL	electron transport layer
EQE	external quantum efficiency
J_{SC}	short circuit current density
V_{OC}	open-circuit voltage
FF	fill factor
Rs	series resistance
R_{sh}	shunt resistance
AVT	average visible transmittance
CRI	color rendering index
SCLC	space-charge-limited current
FET	field-effect transistors
CV	cyclic voltammetry
RMS	root mean square
AFM	atomic force microscopy
SEM	scanning electron microscope
TEM	transmission electron microscopy
GPC	gel permeation chromatography
XRD	X-ray diffraction
PDI	polydispersity index
ITO	indium tin oxide
ZnO	zinc oxide

DCB	dichlorobenzene
CB	chlorobenzene
CF	chloroform
DIO	1,8-diiodoocatne
ODT	1,8-octanedithiol
CN	1-chloronaphthalene
DPE	diphenyl ether
P3HT	poly(3-hexylthiophene)
PEDOT:PSS	poly(3,4-ethylenedioxythiophene) polystyrene sulfonate
TQ1	poly(2,3-bis-(3-octyloxyphenyl)quinoxaline-5,8-dyl-*alt*-thiophene-2,5-diyl)
PCDTBT	poly[n-9'-heptadecanyl-2,7-carbazole-*alt*-5,5-(4,7-di-2-thienyl-2',1',3'-benzothiadiazole]
PPTDTBT	poly(N-(2-decyltetradecyl)-3,7-phenothiazine-alt-5,5(4′,7′-di-2-thienyl-2′,1′,3′-benzothiadiazole))
PPTDTBT-SS	poly(N-(2-decyltetradecyl)-3,7-phenothiazine-S,S-dioxide-alt5,5-(4′,7′-di-2-thienyl-2′,1′,3′-benzothiadiazole))
PCDSeBT	poly(2,7-carbazole-alt-diselenienylbenzothiadiazole)
PTB7-Th	poly[4,8-bis(5-(2-ethylhexyl)thiophen-2-yl)benzo[1,2-b:4,5-b′]dithiophene-co-3-fluorothieno[3,4-b]thiophene-2-carboxylate]
PTB7	poly[[4,8-bis[(2-ethylhexyl)oxy]benzo[1,2-b:4,5-b']dithiophene-2,6-diyl][3-fluoro-2-[(2-ethylhexyl)-carbonyl]thieno-[3,4-b]thiophenediyl]]
PCBM	phenyl-c_{61}-butyric acid methyl ester
$PC_{71}BM$	[6,6]-phenyl-c_{71}-butyric acid methyl ester
PBDB-T-2F (PM6)	poly[(2,6-(4,8-bis(5-(2-ethylhexyl-3-fluoro)thiophen-2-yl)-benzo[1,2-b:4,5-b’]dithiophene))-alt-(5,5-(1’,3’-di-2-thienyl-5’,7’-bis(2-ethylhexyl)benzo[1’,2’-c:4’,5’-c’]dithiophene-4,8-dione)]
BTP-4F (Y6)	2,2'-((2Z,2'Z)-((12,13-bis(2-ethylhexyl)-3,9-diundecyl-12,13-dihydro-[1,2,5]thiadiazolo[3,4-e]thieno[2",3'':4',5']thieno[2',3':4,5]pyrrolo[3,2-g]thieno[2',3':4,5]thieno[3,2-b]indole-2,10-diyl)bis(methanylylidene))bis(5,6-difluoro-3-oxo-2,3-dihydro-1H-indene-2,1-diylidene))dimalononitrile
J52	poly[4-(4,8-bis(5(2-ethylhexyl)thiophen-2-yl)benzo[1,2-*b*:4,5-*b*′]dithiophen-2-yl)5,6-difluoro-2-(2-2hexyldecyl)-7-(thiophen-2-yl)-2*H*-benzo[*d*][1,2,3]triazole]
IEICO-4F	2,2′-((2*Z*,2′*Z*)(((4,4,9-tris(4-hexylphenyl)-9-(4-pentylphenyl)-4,9-dihydro-sindaceno[1,2-*b*:5,6-*b*-dithiophene-2,7-diyl)bis(4-((2-ethylhexyl)oxy)thiophene-5,2-diyl))bis(methanylylidene))bis(5,6-difluoro3-oxo-2,3-dihydro-1*H*-indene-2,1-diylidene))dimalononitrile
NIDCS-HO	(2e,2′e)-3,3′-(2,5-bis(hexyloxy)-1,4-phenylene)bis(2-(5-(4-(n-(2-

	ethylhexyl)-1,8-naphthalimide)yl)-thiophen-2-yl)acrylonitrile)
CO*i*8DFIC	2,2'-[[4,4,11,11-Tetrakis(4-hexylphenyl)-4,11-ihydrothieno[2',3':4,5]thieno[2,3-*d*]thieno[2"",3"":4"',5"']thieno[2"',3"':4",5"]pyrano[2",3":4',5']thieno[2',3':4,5]thieno[3,2-*b*]pyran-2,9-diyl]bis[methylidyne(5,6-difluoro-3-oxo-1*H*-indene-2,1(*3H*)-diylidene)]]bis-propanedinitrile
MDM	metal-dielectric-metal
UPS	ultraviolet photoelectron spectroscopy
AgNWs	silver nanowires
TMM	transfer matrix modeling
CIE	commission internatioinale de l'Éclairage international; international commission on illumination
AVT	average visible light transmittance
FWHM	full width at half-maximum

I. Introduction

1.1 Introduction to Solar Energy and Organic Solar Cells

1.1.1 Unlimited Energy Resource: Solar Energy and Solar Cells

Recently, with the development of electronic devices and the introduction of the IoT (Internet of Things) system, the demand of electric energy has been increasing. Up to now, most of the electrical energy has been supplied from petroleum fuel. However, petroleum fuels have limited reserves and cause a lot of environmental pollution. As a result, the renewable energy needs to be developed actively. Among all renewable energy sources, solar energy is an unlimited and potential energy resource for future energy needs. The sun provides about 120,000 terawatts of energy to the earth's surface per year, which amounts to 6~7 thousand times the world's present energy consumption. Solar cells convert sunlight directly into electrical energy without noise, pollution or mechanical driving parts, so they provide a unique and safe energy resource. In addition, solar cells are suitable for production because they are based on the same principles and materials as semiconductors, which enable the development of computers and communication technologies. **Figure 1.1.1**. shows global energy potential. Comparison of renewable and conventional energy sources. For renewable, the amount of energy is shown per year, while for conventional sources the total reserve is displayed.

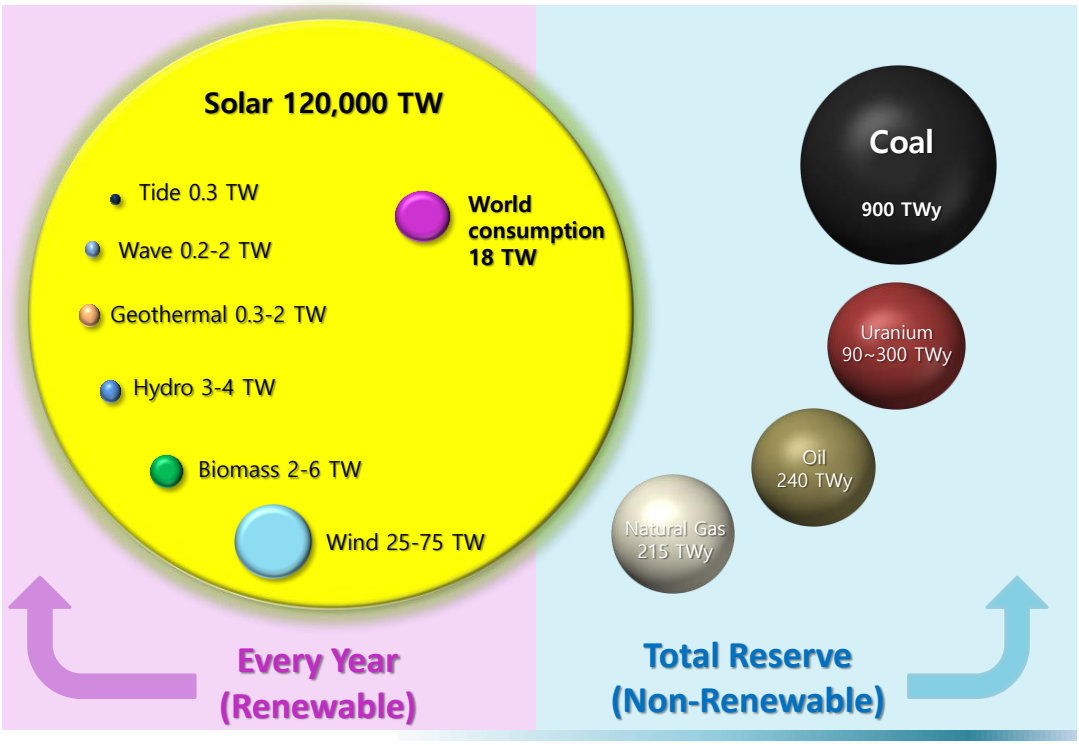

Figure 1. 1. 1. Global energy potential.

1.1.2 Basic of Sunlight

The light that we see every day is only a part of the total energy emitted from the sun that comes to Earth. Sunlight takes the form of 'electromagnetic radiation', and the visible portion of the electromagnetic spectrum is just a tiny portion of the full spectrum, as shown in **Figure 1.1.2**.

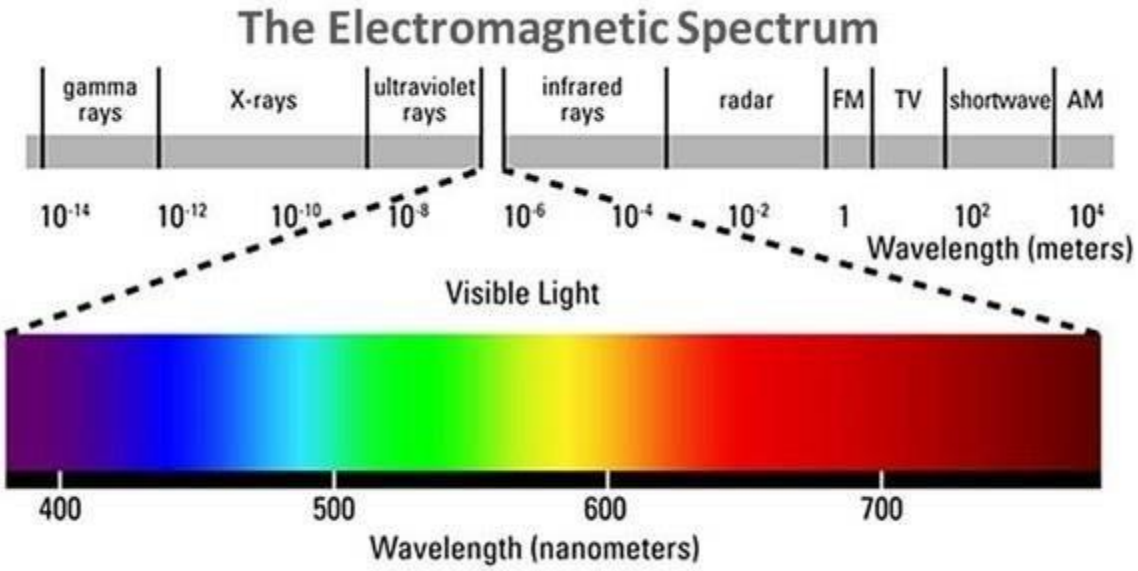

Figure 1. 1. 2. The electromagnetic spectrum.

Sunlight can be separated by passing it through a prism or through a drop of water, as in the case of a rainbow. Different wavelengths show different colors. Light, except the visible range, is invisible to the human eye.

Solar radiation in the atmosphere is relatively constant, but solar radiation on the Earth's surface depends on the absorption and scattering of water vapor, clouds, and pollutants, as well as changes in geographic latitude, season and time of day. As the sunlight passes through the atmosphere, gas, dust, and aerosols absorb the incident photons. In particular, certain gases, such as ozone (O_3), carbon dioxide (CO_2), and water vapor (H_2O), absorb photons close to their combined energy. Far infrared (FIR) light is absorbed by water vapor and carbon dioxide, while most of the ultraviolet (UV) light is absorbed by ozone. Surprisingly, God created the Earth surrounded by the ozone layer, water vapor, and the atmosphere. As a result, the sun's radiation outside of the atmosphere and the sun's radiation to the Earth have slightly different shapes, as shown in **Figure 1.1.3**. The absorption by certain gases in the atmosphere have a relatively minor impact on the overall power. Instead, the main factor that reduces the output of solar radiation is absorption and scattering by air molecules and dust. This absorption process causes reduced power, depending on the path length through the atmosphere. When the sun is directly

overhead, the absorption in the visible spectrum creates a relatively uniform reduction due to these atmospheric elements, so the incident light appears white. But, for long path lengths of sunlight, the absorption and scattering of short wavelengths light is dominant. So, in the morning and evening, the sun appears red in the sky, and its intensity is weaker than in the daytime.

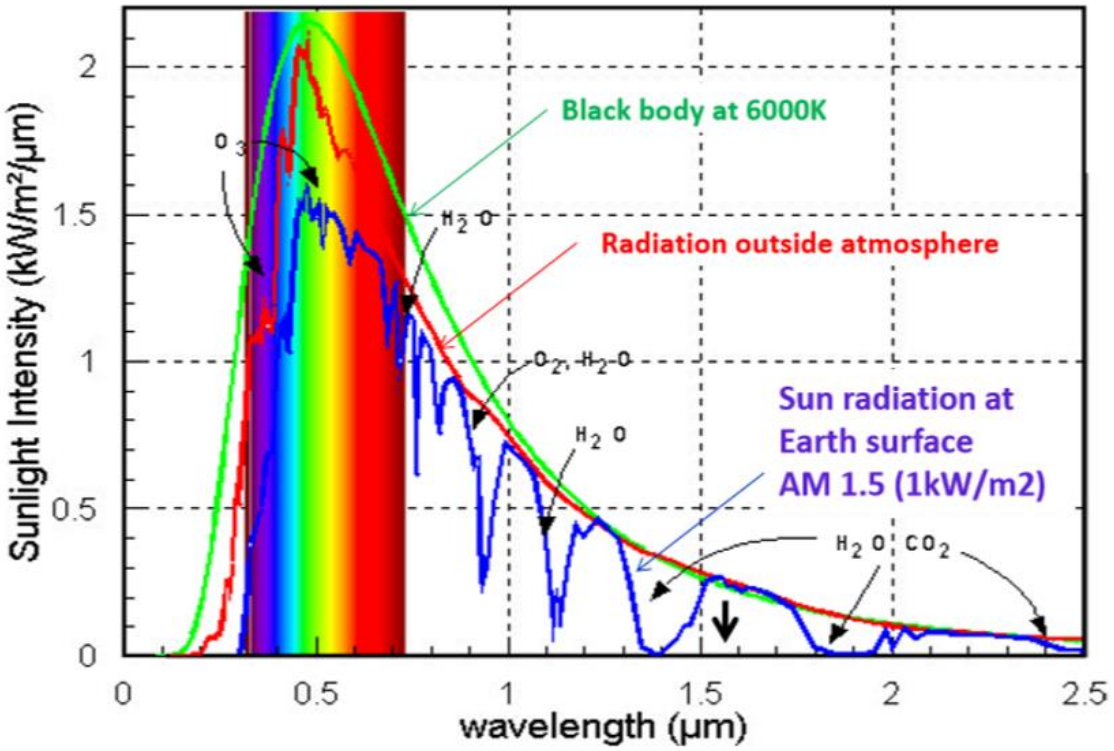

Figure 1. 1. 3. Solar radiation spectrum.

'Air Mass' looks at the length of the shortest path light takes through the atmosphere before reaching earth and uses it determine the amount by which light output decreases as it is absorbed by air and dust. Air Mass is defined by the following equation:

$$AM = \frac{1}{\cos\theta} \tag{1-1}$$

Here, θ is the angle from the vertical line (when the sun is directly overhead) to the surface. When the sun is directly overhead, Air Mass is 1. The standard spectrum of the outside atmosphere is called AM0. The standard spectrum at the surface is AM1.5G.

1.1.3 History of Solar Cells

The photovoltaic effect was discovered by Edmond Becquerel in 1839, The photovoltaic effect occurs when produced power increases when light is shone on two metal electrodes in an electrolyte. In 1873, the photoconductivity of selenium was discovered by Willoughby Smith, and in 1876, William Grylls Adams and Richard Evans Day produced electricity when they exposed selenium to light. In 1905, Albert Einstein published a paper on the photoelectric effect. (In 1921, Albert Einstein won the Nobel Prize for photoelectric effect theory.) Jan Czochralski developed a method of growing highly pure single crystal silicon in 1918. This method has contributed greatly to the commercialization of silicon solar cells. In 1954, photovoltaic technology was started with a 4% efficiency in the United States. This fist silicon photovoltaic (PV) cell was developed by Daryl Chapin, Calvin Fuller, and Gerald Pearson at Bell Labs. The first n-on-p silicon photovoltaic cells were fabricated by T. Mandelkorn, at U.S. Signal Corps Laboratories in 1958. Silicon Sensors, Inc., of Dodgeville, Wisconsin, started producing selenium and silicon photovoltaic cells in 1960. NASA launched the first spacecraft (Nimbus), a satellite powered by a 470watt photovoltaic array in 1964. The world's first photovoltaic powered residences were established by the University of Delaware in 1973. The U.S. Department of Energy launched a solar energy research institute "NREL (National Renewable Energy Laboratory)" in 1977. [1] **Figure 1.1.4**. shows the history of solar cells efficiency in NREL chart. [2]

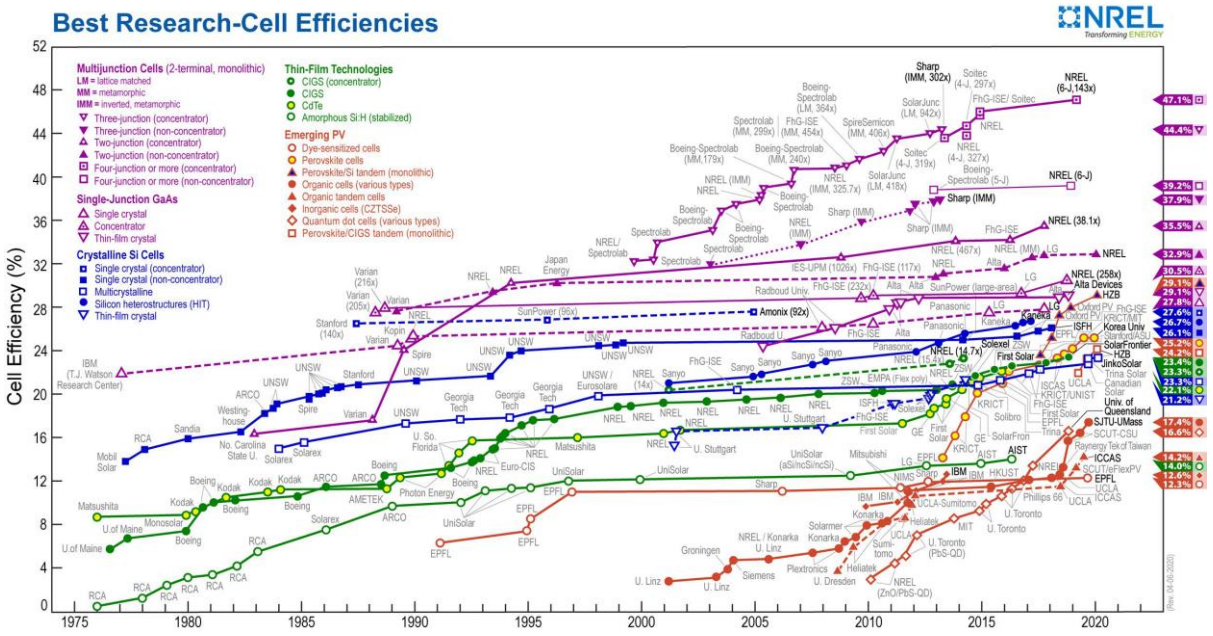

Figure 1. 1. 4. Best research-cell efficiencies (~2020).

As above, before the 1950s, the basic theoretical part of solar cells was studied. The first practical solar power technology was introduced in the 1950s, and solar cells were first spotlighted as a power source for the field of space exploration in the 1960s. Due to the world's growing interest in the Earth's alternative energy source since the 1970s, solar power has been studied as a source of renewable energy. Solar cells using various materials have been developed so far, and the efficiency of each solar cell has been rapidly enhanced so that they can be commercialized. As shown below, the current aspect of the growing solar market means that solar energy is becoming a power source in more applications than ever before. (**Figure 1.1.5**.) [3]

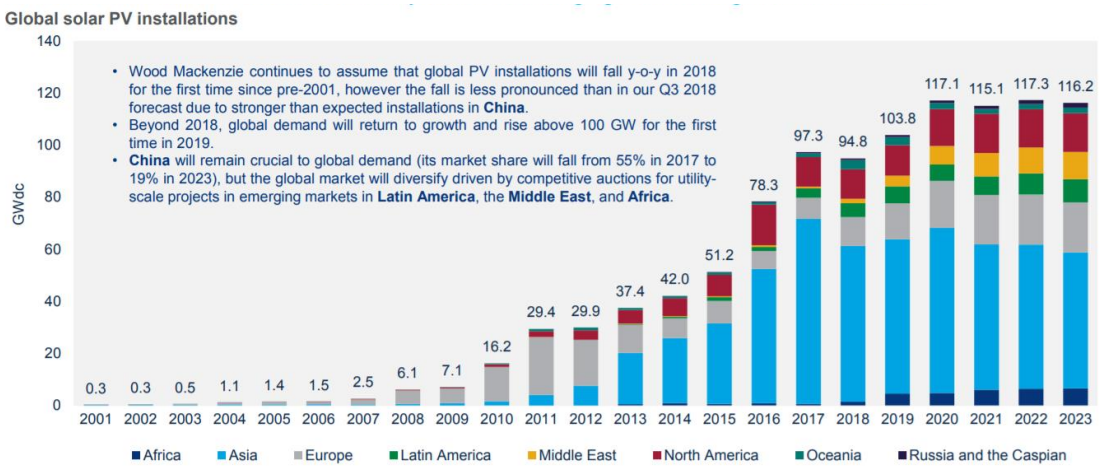

Figure 1. 1. 5. Global solar PV installation status and forecast (2001~2023).

1.1.4 Working Principle of Organic Solar Cells

The working mechanism of organic solar cells is different from that of silicon-based solar cells. Organic solar cells consist of a light absorption layer and charge transfer layer which are stacked in a sandwich structure between an anode and cathode, as shown in **Figure 1.1.6 a**.

The light absorption is based in an organic semiconductor, such as a conjugated polymer or small molecules. The conjugation of the organic materials helps to have conducted or semiconducting properties through delocalized electrons associated with double bonds across the conjugation. These delocalized electrons have higher energies in the lowest unoccupied molecular orbital (LUMO) than valence electrons in highest occupied molecular orbital (HOMO). These energy levels are equivalent to the conduction and valence band in inorganic semiconductor materials (**Figure 1.1.6 b, c**).

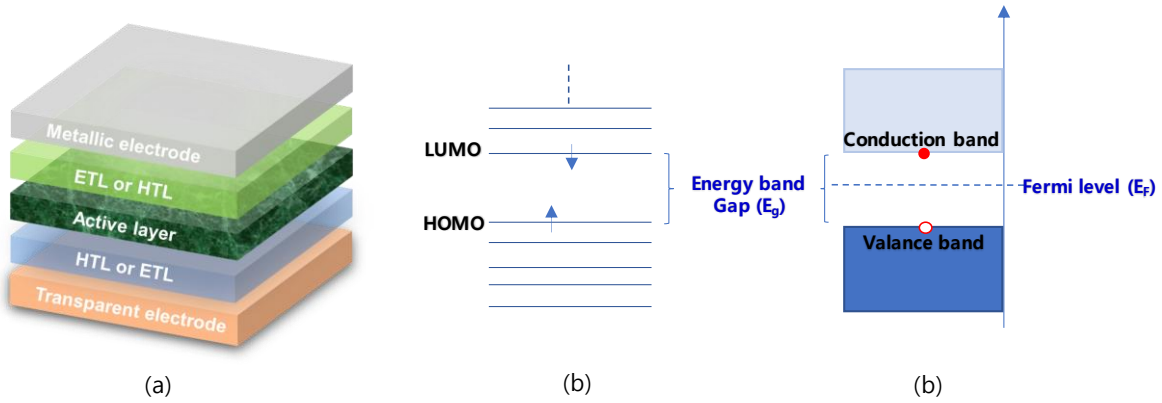

Figure 1. 1. 6. (a) Structure of organic solar cells. Energy band diagram of the (b) organic semiconductor, and (c) inorganic semiconductor.

Two organic semiconductors, called donors and acceptors, each with different properties are used in the light absorbing layer. In most organic solar cells, the light is absorbed by the donor and the electrons in the donor are excited from the ground state (HOMO) to the higher energy state (LUMO). The excited electrons in LUMO and holes that are empty of the electrons in HOMO form electron hole pairs (excitons). The generated excitons diffuse throughout the donor to donor-acceptor interface and dissociate themselves from the charge carrier to become independent electron and holes. However, the excitons are electrically neutral, and so are impervious to the internal electric field and have a short diffusion length (~ 50Å) caused by the short lifetime of organic materials. Therefore, exciton diffusion efficiency is limited, because of the low photocurrent generation of organic solar cells.

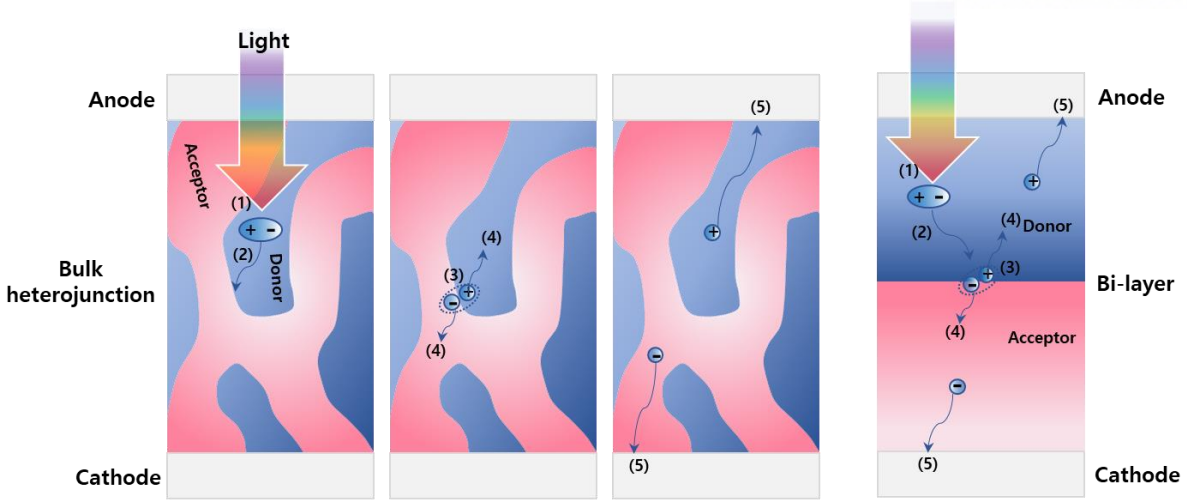

Figure 1. 1. 7. The working principle of organic solar cells in the bulk-heterojunction or bi-layer structures. (1) absorption of light and exciton generation, (2) exciton diffusion to the donor and acceptor interface, (3) charge separation (in the donor/acceptor interface), (4) charge transport, (5) charge collection.

The first organic solar cell was proposed in 1986 by C. Tang as a bilayer structure with a copper pthalocyanine (CuPc) and perylene teracarboxylic derivative.[4] But the efficiency was kept very low by the limited exciton diffusion. In the bilayer structure, in which donor and acceptor are stacked in series, exciton diffusion into the donor/acceptor interface is necessary for exciton dissociation. However, excitons are electrically neutral, as they are unaffected by the internal electric field, and the diffusion length is limited to ~ 50Å due to the short life of excitons in organic materials. The bulk heterojunction structure was proposed in 1992 [5] to solve this problem. In the bulk heterojunction structure, the donor and acceptor organic materials are mixed at the nanoscale level, so that excitons can reach the interface before recombination. Recently, new organic semiconductor materials that have a long exciton diffusion length or that can efficiently dissociate electrons and holes have been developed. Bilayer organic solar cells are therefore gaining attention again. **Figure 1.1.7** shows the working principle of organic solar cells in the bulk-heterojunction or bi-layer structure.

For efficient transportation of electrons and holes, charge carrier transporting layer is inserted between the light absorption layer and electrodes. These layers promote the transport of electrons or holes through favourable energy level positioning, while blocking the other carrier transportation. As such, the electron transport layer is sometimes called the hole blocking layer, and vice versa.

Finally, charge carriers are collected through the electrodes and move along an external circuit to perform electrical work. The electrical properties of the interface between the electrodes and charge transport layers have a significant effect on the charge collection efficiency. In order to improve charge

collection efficiency, buffer layers are developed or a metal that has an appropriate work function is used as an electrode.

1.1.5 Characterization of Organic Solar Cells

The J-V curve of solar cell that shows several important parameters for determine the performance of solar cells such as short circuit current density (J_{SC}) and open-circuit voltage (V_{OC}), fill factor (FF), and efficiency (**Figure 1.1.8.**)

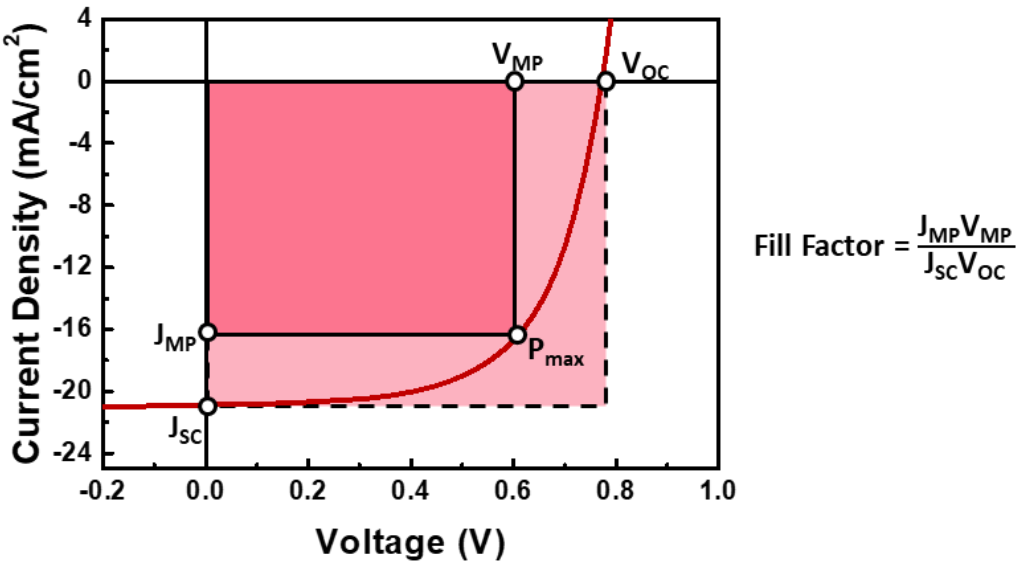

Figure 1. 1. 8. The *J-V* characteristics of solar cell under illumination.

The J-V curve of solar cell follows the modified diode equation. The current density of the solar cell is mostly due to the photo-generated current (J_L). Various factors affect the current value, such as the saturation current of diode (J_S), ideality factor(n), device area(A), series resistance (R_s), and shunt resistance (R_{sh}). Two resistors of R_s and R_{sh} cause parasitic loss while the solar cells are operating.

$$J = J_S\left[\exp\left(\frac{q(V-JR_sA)}{nkT}\right)-1\right]+\frac{V-JR_sA}{R_{sh}A}-J_L \qquad (1\text{-}2)$$

Short circuit current density (J_{SC}) is the current density generated in the solar cell when the voltage across both electrodes is the same (when the solar cell is short-circuited). J_{SC} is the maximum current density that a solar cell can produce. In the case of ideal solar cells with 0 of R_s, and infinite R_{sh}, the

short circuit current is equal to photo-generated current.

The short circuit current density depends on several factors:

1. The number of photons (the power of incident light)
2. The spectrum of incident light
3. The optical properties of the solar cell (absorption and reflection)
4. The probability of carrier collection depends on surface passivation and minority carrier lifetime

The open-circuit voltage (V_{OC}) is the maximum voltage that can be generated from a solar cell, and is the voltage when the net current is zero (when the solar cell is open circuited). V_{OC} can be obtained when the net current is zero in Eq (1-3).

$$V_{oc} = \frac{nkT}{q} \ln \left(\frac{J_L}{J_S} + 1\right) \tag{1-3}$$

The V_{OC} depends on the saturation current (J_S) and the photo-generated current (J_L). While J_L typically has a small variation, the main factor is J_S. The J_S depends on recombination in the solar cell, so open voltage is directly affected by the degree of recombination among the charge carriers.

The J_{SC} and the V_{OC} are the maximum current and voltage that can be obtained from a solar cell respectively. However, at both conditions, the power density (produce of current density and voltage) generated from the solar cell is zero. The "fill factor (FF)" is one of the key parameters that determines the maximum power density generated from a solar cell. The FF is defined as the ratio of the maximum power density (P_{max}) from the solar cell to the product of V_{OC} and J_{SC}.

$$\mathrm{FF} = \frac{P_{max}}{V_{oc} \times J_{sc}} = \frac{V_{mp} \times J_{mp}}{V_{oc} \times J_{sc}} \tag{1-4}$$

J_{SC}, V_{OC} and FF can determine the performance of one commonly used solar cell parameter. The power conversion efficiency(PCE, η) is defined as the ratio of maximum energy generated from the solar cell (P_{max}) to input energy from light (P_{in}). The efficiency depends on the spectrum and intensity of the incident light and the operation temperature of the solar cell. So, evaluation conditions when

measuring the performance of the solar cells must be carefully controlled for accurate performance evaluation. Terrestrial solar cells are measured under AM1.5G conditions at a temperature of 25°C.

$$\mathrm{PCE} = \frac{J_{SC} \times V_{oc} \times FF}{P_{in}} \tag{1-5}$$

1.2 Basic of Semitransparent Solar Cells

1.2.1 Background

In future society, all buildings will combine energy efficient design with renewable energy technology to build a net-zero energy building. The building-integrated photovoltaic (BIPV) technologies are intended to achieve building net zero energy consumption by transforming buildings from energy consumers to sustainable energy producers. BIPV technologies are basically photovoltaic systems that form the integral parts of the building envelope. BIPV is harnessed using a range of advanced technologies such as solar heating, photovoltaic systems, solar thermal energy, and artificial photosynthesis. Among the BIPV technologies, the semitransparent integrated PV is the most used technology in windows and facade of building. Because during the production of electricity, natural light enters the building, creating a good environment. Therefore, it is the most promising future energy system for urban environments. Then, how to make the semitransparent solar cells?

1.2.2 How to Make Semitransparent Solar Cells?

Until recently, semitransparent solar cells markets are mostly based on Si solar cells. Crystalline Si solar cells are usually placed on glass for semi-transparency and are manufactured using partial shading technology. Due to the opacity of crystalline Si solar cells, transparency can be attuned by controlling the space between cells of the panel. However, the semitransparent Si solar cells have limited color control or other aesthetic aspect. [6]

Recently, to overcome these limitations, the development of semitransparent organic solar cells or semitransparent perovskite solar cells, in which various colors can be realized is in the spotlight. Perovskite solar cells (PVSCs) and organic solar cells (OSCs) are highly attractive due to their inherent properties, as shown in **Table 1.2.1.**

Table 1. 2. 1. Comparison of each optimized thickness and absorption properties and charge mobilities between various semiconductor materials.

Photovoltaic Materials	Thickness (μm)	Absorption Properties (cm^{-1})	Charge Mobility ($cm^2V^{-1}s^{-1}$)
c-Si	300	Broad band Absorption coefficient : 10^3	10^3
a-Si	1	Broad band Absorption coefficient : 10^4	10^{-1}
Perovskite	0.3	Broad band Absorption coefficient : 10^5	10^1
Organic materials	0.1	Confined band absorption Absorption coefficient : 10^5 -10^6	10^{-3}

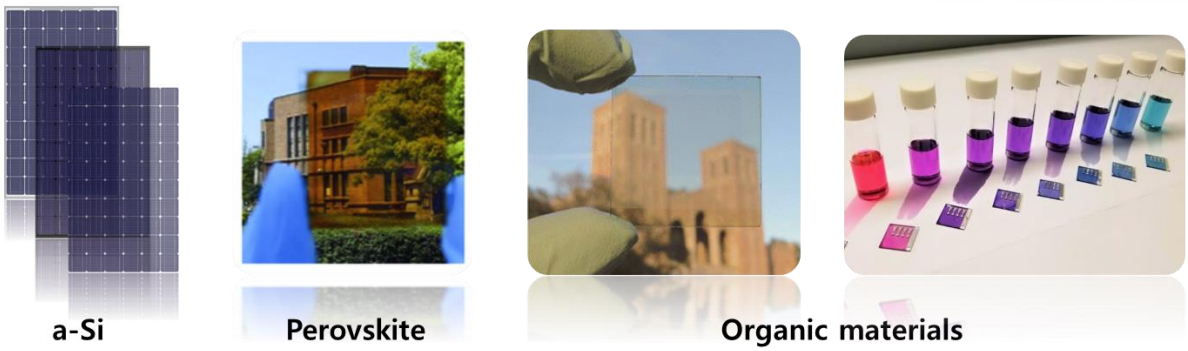

Figure 1. 2. 1. The semitransparent semiconductor materials used in photovoltaic devices.

Among the semitransparent semiconductor materials used in solar cells (**Figure 1.2.1.**), organic materials have low charge carrier mobility, and thus their short diffusion length limits the optimal thickness of the active layer in polymer solar cells (~100nm). So optimized OSCs are inherently semitransparent. Even though the optimized active layer thickness is less than 100nm, due to a high absorption coefficient, it is suitable for manufacturing high performance semitransparent solar cells. Also, another advantage is what can be color tuning by bandgap engineering. For this reason, semitransparent organic solar cells (STOSCs) have been actively studied in recent years.

To realize semitransparent organic solar cells, both semitransparent active materials and semitransparent electrodes need to be studied. **Table 1. 2. 2.** displays a summary of the performances and optical properties in STOSCs using various semitransparent active materials and semitransparent electrodes.

Table 1. 2. 2. Summary of the performances and optical properties in STOSCs

Active materials	electrode	PCE@ AVT(%)	λ@ T_{MAX}(%)	CRI@ CIE(*x*,*y*)	ref
PTB7:$PC_{71}BM$	graphene	3.4 @ 40	-	(0.3109,0.3357)	7
PBDTT-DPP:$PC_{61}BM$	AgNW	4.0 @ 61			8
PBDTT-SeDPP:$PC_{61}BM$	AgNW	4.6 @ 63			9
PCPDTFBT:$PC_{71}BM$	ultrathin film metal (Ag 10nm)	5.0 @ 47.3		99	10
PTB7:$PC_{71}BM$	ultrathin film metal	6.3 @ 24		95.2 @ (0.315,0.316)	
PBDTTT-C-T:$PC_{71}BM$	ultrathin film metal (Ag 6nm)	4.3 @ 35.9		96	11

PCDTBT: $PC_{71}BM$	Ag/1-D photonic crystal	5.3 @ 25.1		97	[12]
PTB7-Th:IHIC	ultrathin film metal (Au 1nm/Ag 15nm)	9.8 @ 36			[13]
PTB7-Th:$PC_{71}BM$	Ag/TiO_x/Ag	4.5 @ -	533 @ 32.1		[14]
PTB7-Th:$PC_{71}BM$	Ag/ITO/Ag	8.1 @ -	584 @ 17.7		[15]
PTB7-Th:$PC_{71}BM$	Au/Ag/WO_3/Ag	9.02 @ -	592 @ 25.7		[16]
PM6:Y6	Sb_2O_3/Ag/ Sb_2O_3/Ag	13.3 @ -	445 @ 24.6		our work

In this paper, we realized a high performance semitransparent solar cells with development of high quality semitransparent electrodes and founding high efficiency colorful active layer through various combinations of donor and acceptor.

1.2.3 Figure of merits of Semitransparent Solar Cells

The transparency and color of semitransparent photovoltaic windows should be provided the aesthetic parts and comfortability when the resident looks out through the window. To optimize the STOSCs, various parameters should be evaluated, such as average visible light transmittance (AVT), transparency color perception, and color rendering index (CRI) as well as PCE.

1. *Average Visible Light Transmittance (AVT)*

The AVT is defined as the average transparency of the cell in the visible wavelength range of 400nm~700nm, considering the spectral response of the human eye. The AVT should be reported as the integration (first moment) of the transmission spectrum and AM 1.5G photon flux weighted against the photopic response of the human eye:

$$\mathrm{AVT} = \frac{\int T(\lambda)\cdot V(\lambda)\cdot AM1.5G(\lambda)d\lambda}{\int V(\lambda)\cdot AM1.5G(\lambda)d\lambda} \quad (1\text{-}6)$$

where $T(\lambda)$ is the transmission spectrum and $V(\lambda)$ is the photopic response.

The transmittance required for semitransparent photovoltaic cells depends on where they are used, but it is generally accepted that 20–30% AVT is the minimum requirement for the window applications. In addition, the colors and transmittance of STOSCs are decided by semitransparent semiconductors and semitransparent electrodes.

2. *Transparency Color Perception*

The color sense that our eyes can detect is very different from the color sense measured using general optical equipment. Our eyes respond better to certain wavelengths, but since optical equipment does not take such matters into consideration, the color sense seen by our eyes and the color analyzed by the equipment show a lot of differences. In order to correct such a point, it is a more accurate method to use STOSCs with a factor applied to the CIE coordinate. The color coordinates can be calculated by the formulas:

$$\begin{cases} X = \int \varphi(\lambda)\bar{x}(\lambda)d\lambda \\ Y = \int \varphi(\lambda)\bar{y}(\lambda)d\lambda \\ Z = \int \varphi(\lambda)\bar{z}(\lambda)d\lambda \end{cases} \tag{1-7}$$

$$\begin{cases} x = \frac{X}{X+Y+Z} \\ y = \frac{Y}{X+Y+Z} \\ z = \frac{Z}{X+Y+Z} = 1 - x - y \end{cases} \tag{1-8}$$

where X,Y,Z are tristimulus values, $\varphi(\lambda)$ is the spectral power distribution of the tested transmittance light, and $\bar{x}(\lambda), \bar{y}(\lambda), \bar{z}(\lambda)$ are color matching functions: their spectra can be seen in **Figure 1. 2. 2.** and **Figure 1. 2. 3.** shows the CIE 1931 chromaticity space.

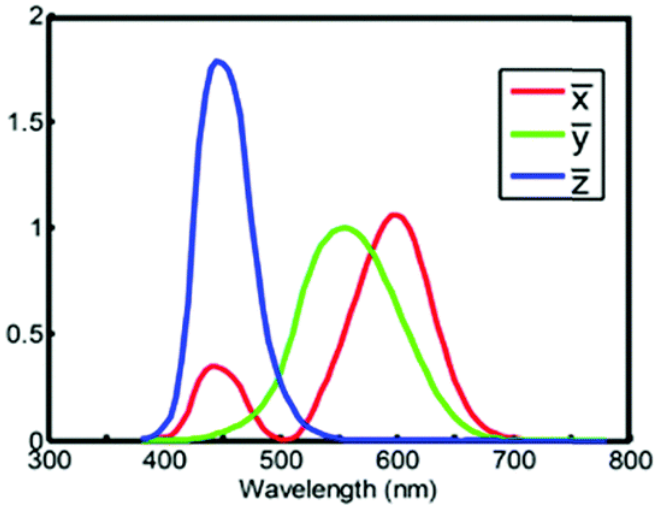

Figure 1. 2. 2. The spectral response of the color matching functions of CIE 1931 *xyz*.

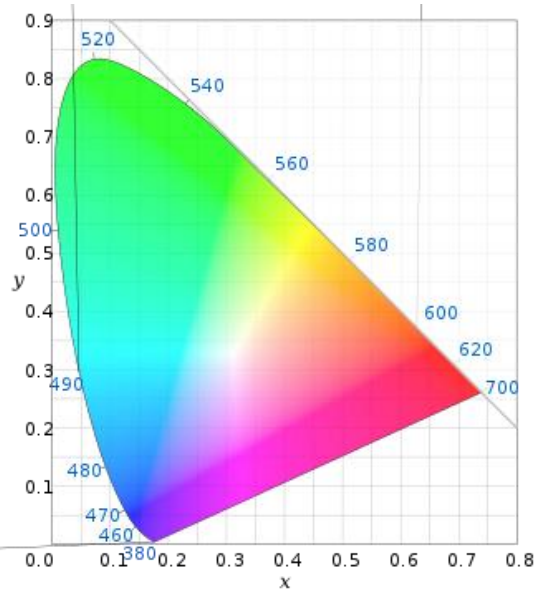

Figure 1. 2. 3. The CIE 1931 chromaticity space.

Standard illuminant D65 and AM 1.5G solar spectrum are commonly used reference for evaluating the factors of STOSCs.

3. *Color Rendering Index (CRI)*

The color rendering feature of STOSCs cannot be expressed simply through transparency perception, so it is necessary to define the CRI index. CRI is derived from transmitted light according to the standard CIE procedure and ranges from 0 to 100. In other words, the higher CRI the more accurately the color is expressed, and a lower CRI shows a lower ability to express color. **Figure 1. 2. 4.** shows a comparison of CRI 75 and 95 strawberry photograph. As shown in the photographs, higher CRI shows more clearer colors, closer to the natural color.

Figure 1. 2. 4. Comparison of CRI 75 and 95 in strawberries photograph.

II. Study on Organic Solar Cells for Improving Performances

2.1. High-Efficiency Polymer Solar Cells with a Cost-Effective Quinoxaline Polymer through Nanoscale Morphology Control Induced by Practical Processing Additives[247]

2.1.1 Research Backgrounds

Bulk-heterojunction (BHJ) polymer solar cells (PSCs) based on conjugated donor polymers and acceptor fullerenes are promising devices for alternative energy sources because of their potential applications in flexible, lightweight, and low-cost large-area devices through roll-to-roll printing. [17-22] Primarily thanks to the development of new low bandgap donor polymers. [23-26] and better control of the nanoscale morphology of the interpenetrating electron donor/acceptor networks, [27-35] great progress has been made in this field, and the power conversion efficiencies (PCEs) of solution-processed PSCs have reached 7-8%. [36] In principle, to push the PCEs of PSCs towards the theoretical limitation, [37] achieving both a high short-circuit current (J_{SC}) and a high open-circuit voltage (V_{OC}) is critical, indeed essential, which has been succeed in using low bandgap polymers with deeper highest occupied molecular orbital (HOMO) levels [38,39] such as PSiFDTBT, [40] PFDTBT [41], and PCDTBT. [42, 43] On the other hand, many largely empirical strategies have been applied to achieve the aforementioned nanoscale morphology, including postproduction annealing [44, 45], solvent annealing [46, 47], and the introduction of processing additives [48]. Alongside higher PCEs, for enhancing the confidence in the commercialization of PSCs, it is of critical importance to synthesize inexpensive polymers as well as to minimize processing cost.

In this regard, we focus our attention to an easily attainable poly(2,3-bis-(3-octyloxyphenyl)quinoxaline-5,8-dyl-*alt*-thiophene-2,5-diyl) (TQ1) that simultaneously possesses HOMO (~ -5.5 eV) and low bandgap (~ 1.7 eV) [49] as required by the proposed 'ideal polymers [50], as well as the processing additives capable of modifying the BHJ organization in that they do not require additional fabrication steps. Despite the initial high PCE of up to 6.0% in a typical BHJ device from TQ1 and [6,6]-phenyl C_{71}-butyric acid methyl ester ($PC_{71}BM$) [51], no attempt has been made to create the optimal blend nanomorphology by using such techniques listed above for more efficient PCE operation.

In this contribution, we have comprehensively studied the effect of various solvent additives (1,8-octanedithiol (ODT), 1,8-diiodooctane (DIO), diphenylether (DPE) and 1-chloronaphthalene (CN)) on

the BHJ PSCs based on TQ1:$PC_{71}BM$. Upon adding 5% (v/v) CN to the BHJ active layer, a PCE as high as 7.08% with J_{SC} of 12 mA/cm^2 and V_{OC} of 0.91 V is achieved. To the best of our knowledge, this is the highest value among quinoxaline-based PCSs reported to date. The techniques of X-ray diffraction (XRD), atomic force microscopy (AFM), and transmission electron microscopy (TEM) have been applied to study the influence of CN on the nanomorphology of TQ1:$PC_{71}BM$ blend. Besides, since long-term stability is another primary area of concern for commercial PSCs, the potential utilization of TQ1:$PC_{71}BM$ into inverted PSCs with ZnO and MoO_3 as electron-selective and hole-selective layers is explored, resulting in a high PCE of up to 5.83%. The inverted device using Au electrode retains over 80% of its original conversion efficiency after 30 days while the conventional one shows negligible photovoltaic activity within 7 days. From a manufacturing perspective, our studies boast a promising pathway for constructing low-cost PSCs with high efficiency as well as long-term stability.

.

2.1.2 Experimental Details

Materials and Characterizations

Unless state otherwise, all reagents were purchased either from Aldrich or Acros and used without further purification. THF was distilled over sodium/benzophenone. ^{1}H NMR spectra were acquired from a VNMRS 600 (Varian, USA) NMR spectrometer. Tetramethylsilane was used as an internal reference with deuterated chloroform as solvent. Gel Permeation Chromatography (GPC) was performed on Agilent technologies 1200 series (UV detector at 500nm). THF and PS was used respectively as eluent and standard for GPC analysis. UV-Vis absorption was measured with Cary 5000 UV/Vis-NIR spectrometer (Varian USA). Cyclic voltammetry measurements were carried out on Solartron electrochemical station (METEK, Versa STAT3) at a scan rate of 100 mV/s at room temperature under argon. A three-electrode setup was used with platinum wire both as counter and working electrode and Ag/AgCl used as reference electrode to be calibrated using a ferrocene/ferrocenium redox couple as an external standard, whose oxidation potential is set at -4.8 eV with respect to zero vacuum level. A 0.1 M solution of *n*-tetrabutylammonium hexafluorophosphate (n-Bu_4NPF_6) in degassed anhydrous acetonitrile was used as supporting electrolyte. The polymer thin film was deposited on PT working electrode.

Fabrication of Photovoltaic Cells

PSC devices were fabricated according to the following procedure: First, the ITO coated glass substrate was cleaned with detergent, then sequentially ultrasonicated in distilled water, acetone and isopropyl alcohol, and then dried overnight in an oven at 100 ^{o}C. Poly(3,4-ethylenedioxythiophene):poly(styrenesulfonate) (PEDOT:PSS) (Baytron PH) was spin-cast at 5000 rpm for 40 s. The substrate was dried at 140 ^{o}C in air for 10 min. Subsequently, it is moved into a glove box for spin-coating the active layer. A mixed solution of TQ1:$PC_{71}BM$ in *o*-dichlorobenzene (*o*-DCB) with various additives (1,8-octanedithiol (ODT), 1,8-diiodooctane (DIO), diphenylether (DPE) and 1-chloronaphthalene (CN)) was spin coated at 1400 rpm for 60 s on the top of the PEDOT:PSS layer to obtain a BHJ film. These samples were brought into a vacuum system (about 10^{-7} Torr), and an Al electrode (100 nm) was deposited on the top of the BHJ layer. In the case of inverted structure cells, ZnO is applied as electron transport layer. ZnO layer was deposited on ITO coated glass by spin coating with 3000 rpm for 40 s and dried at 120 ^{o}C in air for 15 min. The active layer was coated with the same method explained above. Then, a thin layer of MoO_3 film (~5 nm) was evaporated on the top of the active layer. Finally, the anode (Ag or Au, ~95 nm) was deposited on the active layer in a vacuum (about 10^{-7} Torr) thermal evaporator. Measurements were carried out with the solar cells in the glove-box by using a high quality optical fiber to guide the light from the solar simulator equipped with a

Keithley 2635 A source. The solar cell devices were illuminated at an intensity of 100 mW/cm^2. For the accurate information, the IPCE measurements were carried out with QEX7. The device structures of the hole and electron only devices are ITO/PEDOT:PSS/TQ1:$PC_{71}BM$/Au and FTO/TQ1:$PC_{71}BM$/Al, respectively. The space-charge-limited current (SCLC) mobilities were estimated the Mott-Gurney square law $J_{\mathrm{SCLC}} = \frac{9}{8}\varepsilon_{\mathrm{r}}\varepsilon_0\mu(\frac{V^2}{L^3})$, where ε_{r} is the dielectric constant of the material, ε_0 is the permittivity of free space, L is the distance between the cathode and anode, which is equivalent to the film thickness, and V is the applied voltage.

2.1.3 Results and Discussion

Figure 2.1.1a-c present the molecular structures of TQ1, $PC_{71}BM$, and solvent additives used in this study together with the energy level diagrams of the component materials. TQ1 was synthesized by a Stille coupling according to literature reports [52, 53], which shows a relatively high number average molecular weight (M_n) of 48 kg/mol with polydispersity index (PDI) of 3.6, as determined by gel permeation chromatography (GPC). On the basis of the photophysical and electrochemical studies (see **Figure 2.1.2**), as the reduction potentials of TQ1 are out of our scan range, the lowest unoccupied molecular orbital (LUMO) energy level (-3.8 eV) is calculated from the HOMO energy level (-5.5 eV) and the optical band gap (1.7 eV).

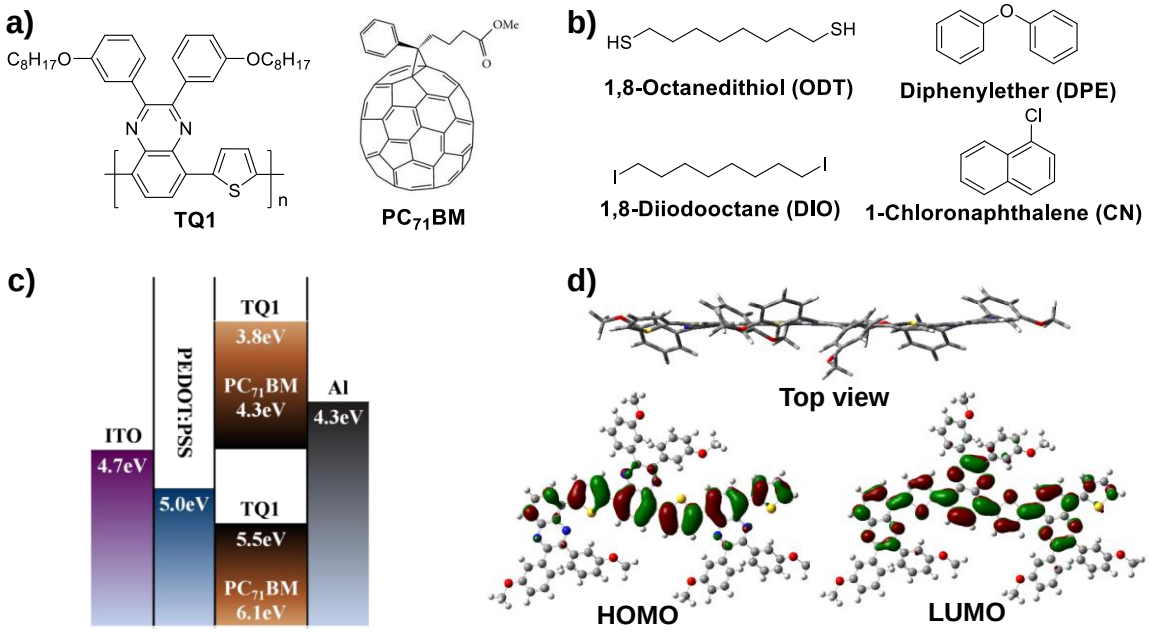

Figure 2. 1. 1. (a) Molecular structures of TQ1, $PC_{71}BM$, and (b) various solvent additives used in this study. (c) Energy level diagram of the components. (d) DFT-optimized geometries and charge-density iso-surfaces for the HOMO and LUMO levels of TQ1 trimer.

Upon utilizing a model trimeric system containing methoxy groups instead of octyloxyl chains for simplicity, the optimized molecular geometry of TQ1 and its molecular orbitals of the calculated HOMO and LUMO iso surfaces were computed by density functional theory (DFT, B3LYP/6-31G) (**Figure 2.1.1d**). Interestingly, the molecular orbital distributions reveal that both the HOMO and LUMO are well spread over the whole conjugated backbone, implying a 'strong donor-weak acceptor' system of TQ1. This contrasts with many other donor-acceptor polymers in which the LUMO is localized upon the electron accepting core of the polymer backbone. The localization can hinder interchain electron transport, since hopping requires good

alignment of the localized LUMO levels [54, 55]. As well, good coplanarity exists between the comonomers (see the top view in **Figure 2.1.1d**).

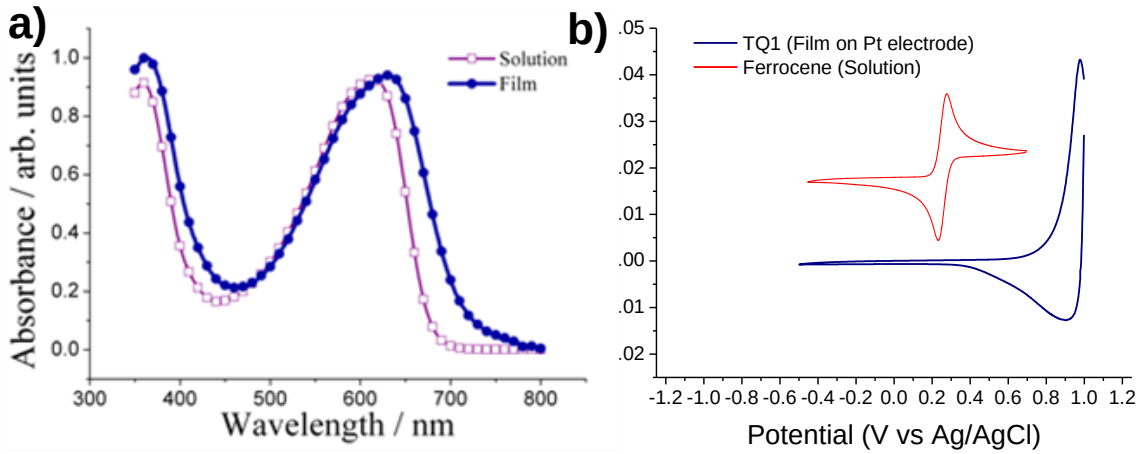

Figure 2. 1. 2. (a) UV-Vis absorption spectra of TQ1 in dilute chloroform solution and thin films on glass plate. (b) Cyclic voltammograms of TQ1 in the films.

Table 2. 1. 1. Photovoltaic parameters of the devices[a]

TQ1:$PC_{71}BM$	J_{SC} [mA/cm^2]	V_{OC} [V]	*FF*	PCE [%]
1:3 (w/w), w/o additives	8.03	0.90	0.54	3.94
1:3 (w/w), with 2% ODT	4.84	0.79	0.51	1.93
1:3 (w/w), with 2% DIO	6.07	0.91	0.59	3.27
1:3 (w/w), with 2% DPE	9.22	0.89	0.58	4.77
1:3 (w/w), with 2% CN	10.9	0.81	0.56	4.94
1:2 (w/w), w/o additives	7.42	0.83	0.59	3.61
1:2 (w/w), with 2% CN	11.8	0.84	0.64	6.38
1:2 (w/w), with 5% CN	12.2	0.91	0.64	7.08
1:2 (w/w), with 7% CN	10.8	0.88	0.61	5.78

[a] 2 wt% from *o*-DCB

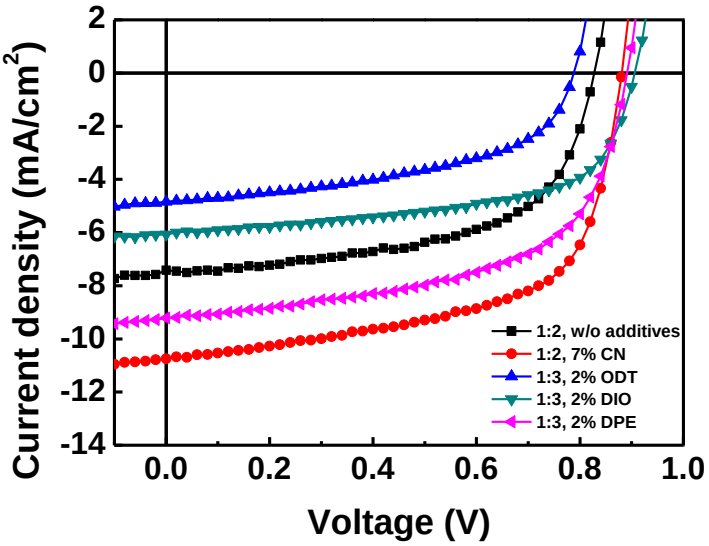

Figure 2. 1. 3. *J-V* characteristics of PSCs based on TQ1:$PC_{71}BM$ without or with various additives.

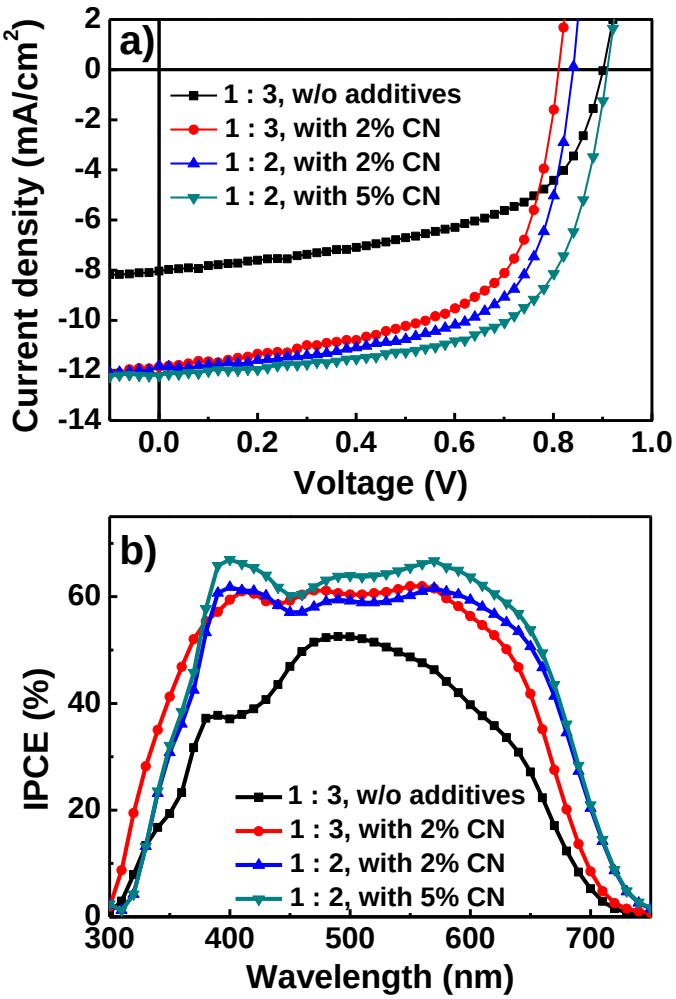

Figure 2. 1. 4. (a) *J-V* characteristics and (b) incident photon-to-current efficiency (IPCE) of PSCs based on TQ1:$PC_{71}BM$ without or with different concentrations of CN.

Photovoltaic effects of TQ1 were investigated in BHJ PSCs with the device structures of the standard configuration glass/ITO/PEDOT:PSS/TQ1:$PC_{71}BM$/Al. The optimized fabrication process of PSCs by casting TQ1:$PC_{71}BM$ in a 1:3 (w/w) ratio from *o*-dichlorobenzene (*o*-DCB) was reported in previous work, and was therefore used to make the PSCs under the same conditions, firstly (see the experimental section for the detailed information). The representative current-density-voltage (*J-V*) characteristics of the devices under the illumination of simulated AM 1.5G conditions (100 mW/cm^2) are shown in **Figure 2.1.4** and the parameters are summarized in **Table 2.1.1**. In this condition, only modest PCE of 3.94% with a V_{OC} of 0.90 V, a J_{SC} of 8.03 mA/cm^2, and a fill factor (*FF*) of 0.54 is obtained. Next, the effect of 2% (v/v) of various solvent additives (1,8-octanedithiol (ODT), 1,8-diiodooctane (DIO), diphenylether (DPE) and 1-chloronaphthalene (CN)) on the TQ1 and $PC_{71}BM$ (1:3 (w/w)) were investigated (see in **Figure 2.1.3**).

Interestingly, among the devices containing solvent additives, we find adding CN into the *o*-DCB solution of TQ1:$PC_{71}BM$ prior to spin coating, the PCE dramatically increased up to 4.94%. The performance of BHJ PSCs could be determined by the morphology of the active thin layer [56]. With large interfacial area and bicontinuous interpenetrating networks, small phase domains enable maximum charge separation from donor polymer to acceptor fullerene derivative and enhance the collection of charge carriers from the active layer to each electrode. In addition, atomic force microscopy (AFM) images were examined to elucidate the effect of additives on the phase separation of thin films of TQ1:$PC_{71}BM$. [57,58] The morphology of the films shows very rough with ODT, DIO, and DPE while the film with CN has small phase domains as shown in **Figure 2.1.5**, where the root-mean-square (RMS) roughness values of each film are 6.08, 1.62, 1.10, and 0.75 nm, respectively. Regardless of a complete mechanistic understanding at this stage, it is evident that CN plays an important role in controlling the optimal morphology and creating a better interpenetrating network in TQ1:$PC_{71}BM$ through the decreased donor and acceptor domain sizes. This is reasonably advocated by the fact that the efficiently induced uniform film morphology with CN displays relative to those with other additives. Therefore, in the course of the planned nanomorphology study, not only do we further investigate the influence of CN on the film morphology and device performance, but also seek to understand the mechanism for improvement and thereby identify guidelines for selecting appropriate solvent additives for use in similar BHJ PSCs. We find that the device performance can be further improved by changing the weight ratios of TQ1:$PC_{71}BM$ as well as different volume fractions of CN.

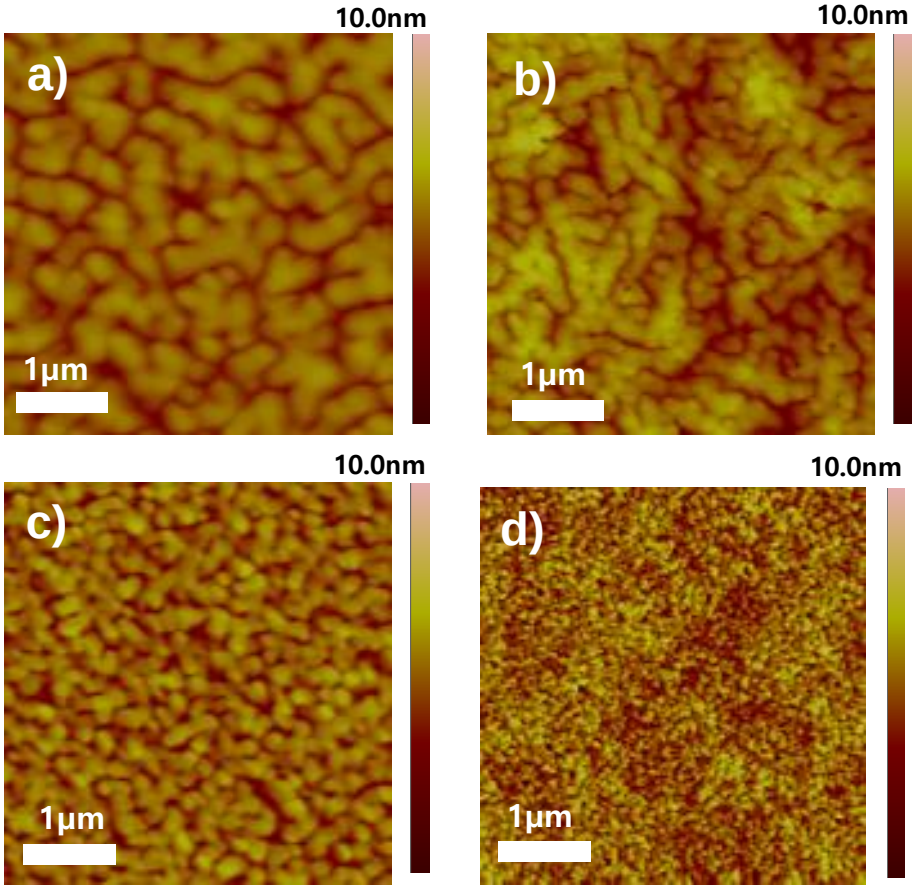

Figure 2. 1. 5. (a) Surface morphology of TQ1:$PC_{71}BM$ blend films; 1:3 w/w with (a) 2% (v/v) ODT (b) 2% (v/v) DIO (c) 2% (v/v) DPE (d) 2% (v/v) CN from tapping mode AFM (the RMS roughness values are 6.08, 1.62, 1.10, and 0.75 nm, respectively.).

Through the fully optimization of the device architecture process, the best device, prepared using 5% (v/v) CN additive with a weight ratio of 1:2, reaches an overall PCE of 7.08%, with V_{OC} = 0.91 V, J_{SC} = 12.2 mA/cm^2, and *FF* = 0.64, which is the highest PCE reported to date for PSCs fabricated polymers containing quinoxaline unit. This work highlights the great potential of the low-cost polymer to realize high-performance PSCs by taking advantage of the practical processing step as an additional driving force to further optimize the active layer nanomorphology. The integrated incident photon-to-electron conversion efficiency (IPCE) for these devices matches the measured short-circuit current to within 1% error (**Figure 2.1.4b**).

The J_{SC} and *FF* values are primarily determined by the charge carrier mobilities and blend morphology when the absorbing materials and film thicknesses are kept constant [59, 60]. Therefore, the mobility and morphology of the BHJ blends with and without CN were investigated to probe the possible origin of the efficiently increased PCE as a function of CN addition. Both the electron and hole mobilities were measured by using the space-charge-limited current (SCLC) method [61, 62], as shown in **Figure 2.1.6** and **Table 2.1.2**.

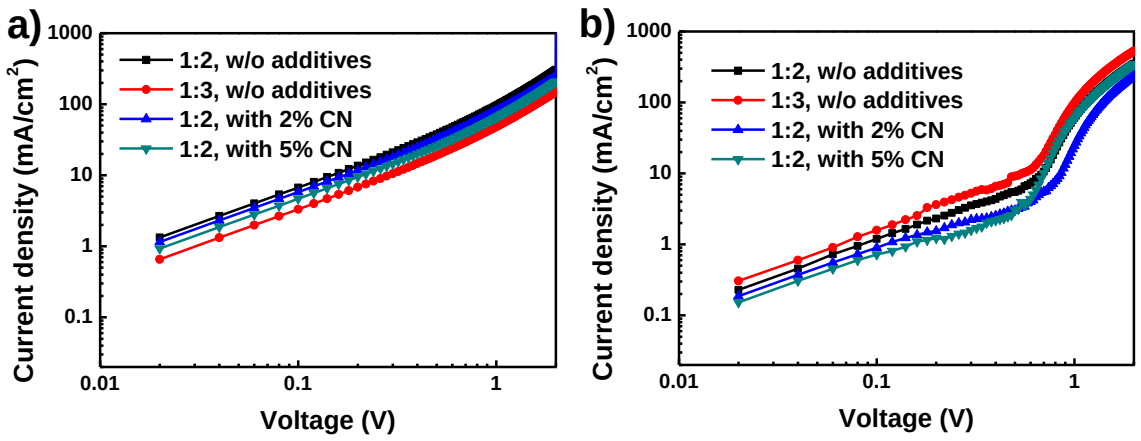

Figure 2. 1. 6. Measured *J-V* characteristics by the space-charge-limited current (SCLC) method with TQ1:$PC_{71}BM$ films under dark conditions without or with different concentrations of CN for hole-only device (a) and electron-only device (b).

Table 2. 1. 2. Calculated electron and hole mobility values for TQ1:$PC_{71}BM$ devices without or with different concentrations of CN.

TQ1:$PC_{71}BM$[a]	Hole mobility [m^2/Vs]	Electron mobility [m^2/Vs]	Hole/Electron ratio
1:3, w/o additives	6.23×10^{-4}	1.27×10^{-3}	0.49
1:2, w/o additives	9.64×10^{-4}	3.62×10^{-4}	2.66
1:2, with CN 2%	9.47×10^{-4}	3.61×10^{-4}	2.63
1:2, with CN 5%	5.97×10^{-4}	5.36×10^{-4}	1.11

[a] 2 wt% from *o*-DCB

In the case of the blend films without CN, the hole mobilities (μ_h) are generally an order of magnitude lower than the electron mobilities (μ_e). Notably, the μ_h for the films containing CN drops slightly, and meanwhile the μ_e is improved, leading to a smaller value between the mobility ratio. This supports the beneficial effect of the CN addition on TQ1:$PC_{71}BM$. We attribute the large increase in J_{SC} and *FF*, at least partially, to the well-balanced charge transport in the optimized blends (TQ1:$PC_{71}BM$ of 1:2 (w/w)) processed with 5% (v/v) CN. [63, 64]

To gain a relatively complete picture of film morphologies in the TQ1:$PC_{71}BM$ blends upon the addition of CN, a combination of X-ray diffraction (XRD), AFM, and transmission electron microscopy (TEM) was utilized. The AFM height images presented in **Figure 2.1.7a-d** show large features with RMS of 1.51 nm when no additive is applied, while the significantly reduced feature sizes are observed upon the addition of CN. This suggests that the majority of CN

additive far leads to rougher surfaces. Note that the surface films made of TQ1:$PC_{71}BM$ (1:2 (w/w)) with 5% (v/v) of CN show the absence of the large domains and the finest features with RMS of 0.47 nm. Thereby, CN is believed to allow much more improved miscibility between TQ1:$PC_{71}BM$ and formation of interpenetrating networks. Based on current understanding of PSCs, the improved morphology can explain the enhanced photocurrents (7.42 vs 12.2 mA/cm^2) and *FF* (0.59 vs 0.64) of the optimized TQ1:$PC_{71}BM$ of 1:2 (w/w) blend processed with CN, when compared to the devices without CN. The effect of CN is further visualized by TEM (**Figure 2.1.7e-h**). Large scale phase separation with a continuous darker phase embedded with discrete micrometer-size light domains (~100-200 nm in diameter) is seen in the films processed without CN additive. In the films, processed with CN, large fullerene domains are absent, indeed, creating elongated nanofibrous networks through the promotion of the demixing of the TQ1 and $PC_{71}BM$, in qualitative agreement with the above AFM results. [65]

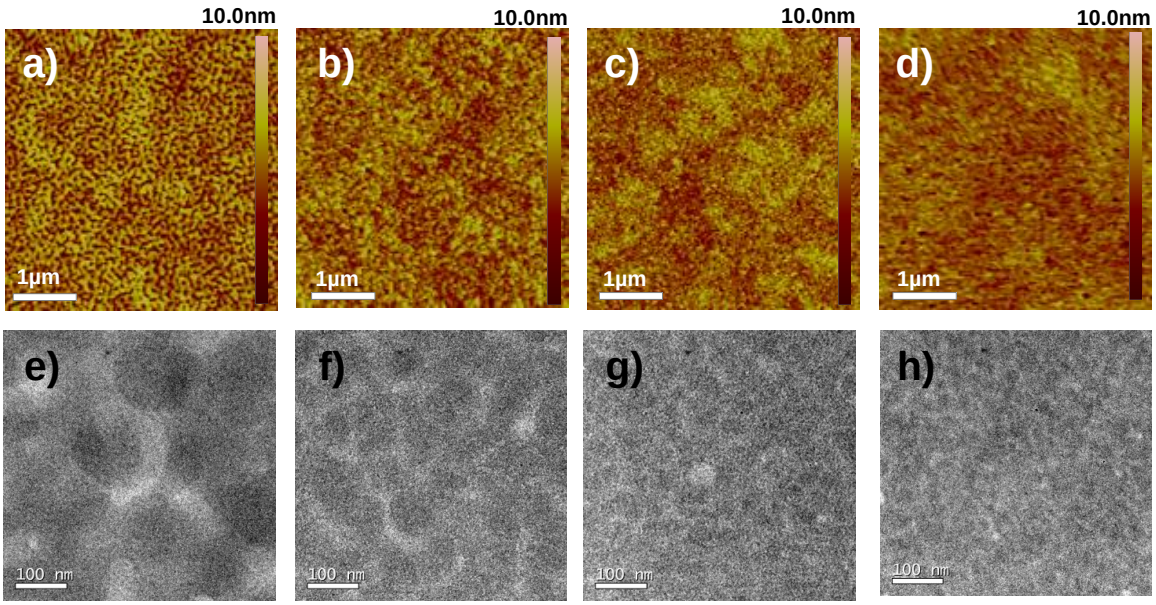

Figure 2. 1. 7. Surface morphology of TQ1:$PC_{71}BM$ blend films; (a)1:3 (w/w) without additives, (b) 1:3 (w/w) with 2% (v/v) CN, (c) 1:2 (w/w) with 2% (v/v) CN, and (d) 1:2 (w/w) with 5% (v/v) CN from tapping mode AFM (the rms roughness values are 1.51, 0.75, 0.68, and 0.47 nm, respectively.). (e-f) The TEM images to corresponding to the AFMs.

To clearly quantify the structural heterogeneity and the dynamics of ordering of TQ1 with $PC_{71}BM$ being forced into the intercrystalline, we monitored the out-of-plane XRD of the films annealed at 120 ^oC corresponding to the images of **Figure 2.1.8**. Distinct primary diffraction (100) features in pure TQ1 films are detected at $2\theta = 3.84°$, corresponding to *d*-spacing of 23.0 Å, indicating that TQ1 is preferentially oriented with their (100) plane perpendicular to the

substrates. However, diffractions originating from either second-order peaks or π-stacking planes cannot be observed. These above XRD results suggest the signature of ordered lamellar packing motif with a presumably edge-on orientation for the pristine TQ1 films. [66, 67]

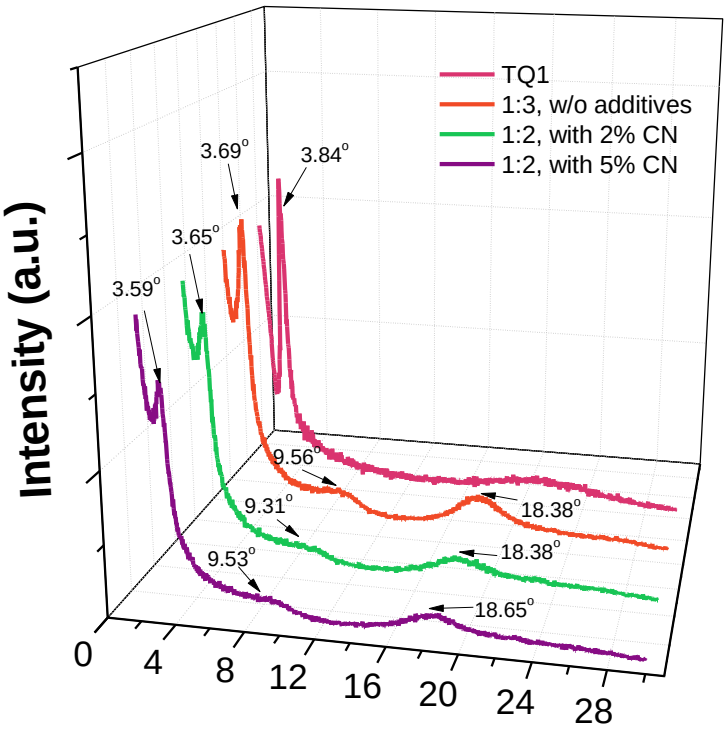

Figure 2. 1. 8. XRD patterns of (a) TQ1 and TQ1:$PC_{71}BM$ blend films with or without different concentrations of CN.

When the $PC_{71}BM$ is mixed with TQ1 processed with and without CN, the *d*-spacing peaks are somewhat shifted, which is expanded by ~1.6 Å. Such an expansion of the lattice is most likely attributed to the intercalation of the $PC_{71}BM$ between the side-chains of the TQ1. [68] Interestingly, the new diffractions emerges at 2θ = ~9.5° (~9 Å) in the blends, which probably arises from the second-order diffraction (200)' of the intercalated TQ1:$PC_{71}BM$ lamellar structure. [69] Another possible explanation for this is that the $PC_{71}BM$ molecules can diffuse through the polymer matrix and form large single crystals. [70-72] Notably, we observe the broad featureless peaks (010) caused by the characteristics of the π-π interchain stacking in the profiles of blended samples, which is probably due to the occurrence of intercalation between the polymer side chains and fullerene. [73, 74] In addition, this implies that the polymer chains in the blends of TQ1:$PC_{71}BM$ have either a slight preference in the face-on orientation or a co-existence of the face-on and other tiled chain orientations.[75] Besides, the (010) peaks of the blend films with the 5% (v/v) of CN shift from 18.38° (π-stacking distance of 4.82 Å) to 18.65° (π-stacking distance of 4.75 Å). The reduction of the interlayer spacing in the blend films cast from

the solvent with additive could be helpful for charge transportation in the corresponding device.[76]

Compared with conventional PSCs, inverted-type devices demonstrate better long-term ambient stability by avoiding the need for the corrosive and hygroscopic hole-transporting PEDOT:PSS and low-work-function metal cathode, both of which are detrimental to device lifetime.[77-79] Therefore, the highly respectable PCE of over 7% for TQ1:$PC_{71}BM$ BHJ conventional devices prompts us to take an initial look at PSCs with using an inverted structure, which may boast the practical applications in future low-cost mass production. The present inverted PSCs architecture (ITO/ZnO/TQ1:$PC_{71}BM$/MoO_3/Ag) employed in this study is shown in **Figure 2.1.9a** (see the experimental section for the detailed fabrication). To mimic BHJ cell fabrication conditions, the optimized active layer components (TQ1:$PC_{71}BM$ of 1:2 (w/w)) processed with 5% (v/v) CN were chosen for the inverted BHJ PSCs. A PCE of up to 5.83% is observed for the inverted PSCs with a V_{OC} of 0.82 V, a J_{SC} of 11.4 mA/cm^2, and a *FF* of 0.62. Note that the measured J_{SC} is in a good agreement with IPCE measurements (**Figure 2.1.9b**).

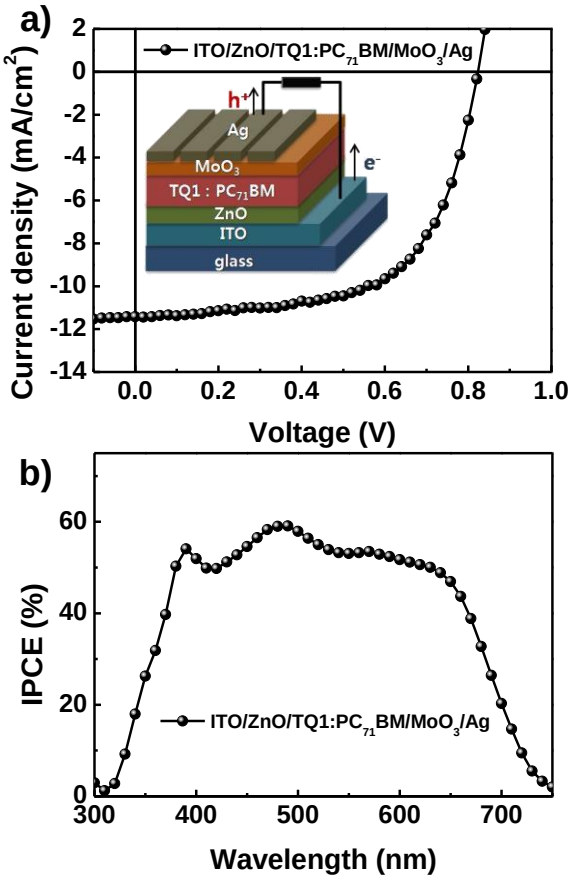

Figure 2. 1. 9. (a) *J-V* characteristics and (b) IPCE of the inverted PSCs (ITO/ZnO/TQ1:$PC_{71}BM$ /MoO3/Ag). Insert; the inverted device architecture.

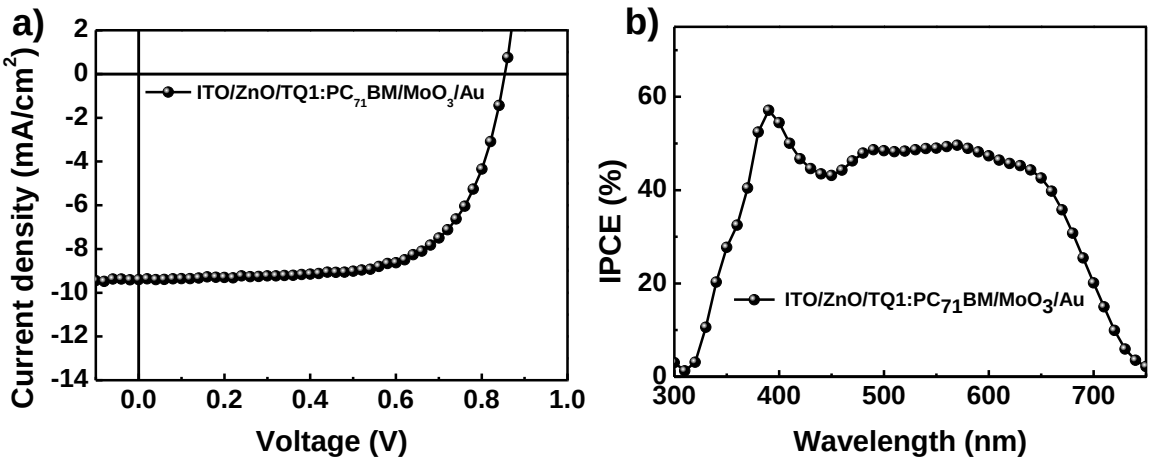

Figure 2. 1. 10. (a) *J-V* characteristics and (b) IPCE of the inverted TQ1:PC71BM PSCs using Au. J_{sc} = 9.40mA/cm2, V_{oc} = 0.85, *FF* = 0.67, PCE = 5.35%

The preliminary results can be comparable with those of the high-performance inverted PSCs. [80-84] However, the PCE of current inverted PSCs based on TQ1:$PC_{71}BM$ is inferior to that of the best conventional PSCs above, due to the reduced J_{SC} and V_{OC}. This implies that the empirically optimized fabrication for the conventional architectures is quite different from that for the inverted cells since PSCs with an inverted device structure are sensitive to the electrical properties of the interfaces between the buffer layer and the photoactive layer. A systematic experimental study of the influences of morphology and thickness of buffer layers on the photovoltaic properties of inverted PSCs will recover the existing J_{SC} and V_{OC} losses, which will be set up as our next task.

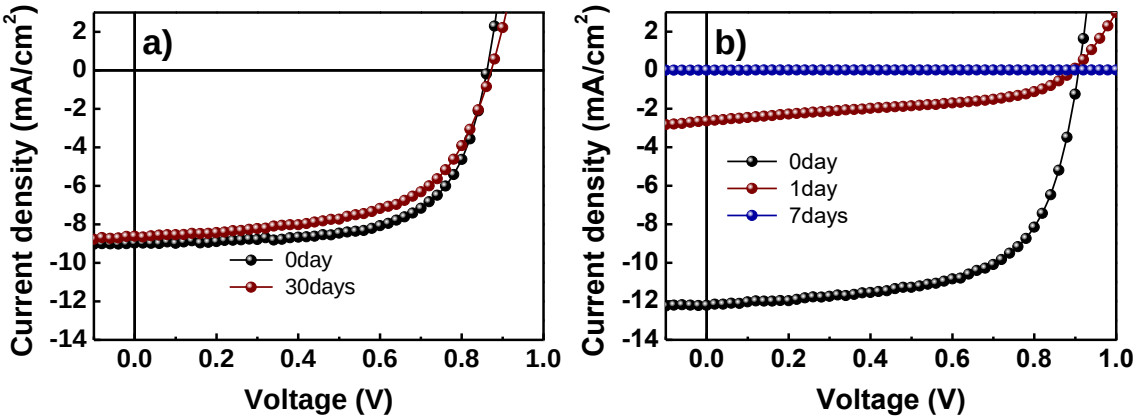

Figure 2. 1. 11. (a) *J-V* characteristics of the un encapsulated inverted PSCs (ITO/ZnO/TQ1:$PC_{71}BM$ /MoO3/Au) and (b) the unencapsulated conventional PSCs over a certain period time in air under ambient conditions.

On the other hand, by replacing the MoO_3/Ag with a MoO_3/Au electrode, other inverted PSCs were fabricated, which would produce more environmentally stable devices due to the inert electrodes. Although the PCE of Au devices is 0.48% smaller than that of Ag devices (see **Figure 2.1.10**), which is typically attributed to the decreased reflectivity in the visible region of Au, [85] the PCS shows high stability in air, retaining more than 83% of its initial efficiency over 30 days of ambient exposure (**Figure 2.1.11a**). In contrast, under the same conditions, the devices with the conventional structure fall to over 85% (from 7.08% to 1.06%) for only 1 day and completely lose their efficiency within 7 days of ambient exposure (see **Figure 2.1.11b**).

2.1.4 Conclusion

As a final note, we have demonstrated high-performance PSCs based on the structure of an easily synthesized low bandgap polymer, TQ1, where solvent additives, such as ODT, DIO, DPE, and CN play a critical role in enhancing their PCEs. A PCE of higher than 7% that doubles to that of the devices processed without the solvent additives has been realized by means of engineering of active layer nanomorphology upon the addition of 5% (v/v) CN. This is the highest efficiency reported for quinoxaline-based polymers and comparable the record champion cell efficiencies for the PSCs in single junction devices. By using a systematic experimental study in the combination with XRD, AFM, and TEM, we find that the addition of CN promotes small scale phase separation, less heterogeneous surface features through the improved miscibility of the TQ1 and $PC_{71}BM$, resulting in well-intercalated polymer/fullerene networks. In addition, without fully optimal morphology control and processing optimization, not only do the corresponding inverted PSCs show still respectable PCE of 5.83%, but also the inverted devices with Au electrode retains over 83% of the original efficiency after 30 days. From an easy and practical perspective, our findings offer a bright future for commercialization of PSCs, although guidelines for selecting an appropriate solvent additive remain relatively unclear in various materials systems.

2.2. Easily Attainable Phenothiazine-Based Polymers for Polymer Solar Cells: Advantage of Insertion of *S,S*-dioxides into its Polymer for Inverted Structure Solar Cells[248]

2.2.1 Research Backgrounds

The dramatic growing need for renewable energy supply is increasing the demand for new technologies for photovoltaic energy conversion. Polymeric solar cells (PSCs) have attracted much attention due to their potentials for low cost, lightweight, and good compatibility with the roll-to-roll process for making flexible large area devices.[86-90] So far, the most efficient polymer solar cell system is built on the concept of bulk-heterojunction (BHJ) structure, which uses a blend of an electron-donor polymer and an electron-acceptor fullerene. Recently, power conversion efficiencies (PCEs) of 6−8% have been realized by using new conjugated polymer donors[91-95] or novel fullerenederived acceptors.[96-98] Aside from achieving higher PCEs, improving the stability of PSCs is equally important. In general, conventional PSCs are comprised of a BHJ active layer sandwiched between an acidic poly(3,4-ethylenedioxythiophene): poly(styrenesulfonate) (PEDOT: PSS) coated indium tin oxide (ITO) anode and a low work-function metal cathode (e.g., Al and Ca). In such a device structure, not only does the cathodes easily oxidize in air but also the acidic PEDOT:PSS-ITO can suffer interfacial degradation over the operating lifetime.[99] As alternative to the regular device configuration, PSCs with an inverted device structure have been developed, which enables the use of stable and printable high work-function metals (e.g., Ag and Au) as hole collecting top electrodes and n-type low work-function

metal oxides (e.g., TiO_x and ZnO) as electron collecting bottom electrodes.[100, 101] Thus, with advances made on the aforementioned efficiency front, the lifetime and reliability of PSCs are also envisaged by utilizing the inverted PSC configuration through the replacement of the low work function metal cathode and the elimination of PEDOT:PSS layer. Recently, several classes of narrow bandgap donor−(D−) acceptor (A) type polymers have been developed to better harvest the solar spectrum with deeper HOMO energies that can be helpful in realizing high open circuit voltage (V_{OC}) and PCEs, as the V_{OC} value of PSCs is directly proportional to the offset between the HOMO level of electron donor and the LUMO level of electron acceptor.[102-104] Among them, poly(2,7-carbazole-alt-dithienylbenzothiadiazole) (PCDTBT) showed particularly interesting achievement of a PCE in excess of 6% from a BHJ cell with V_{OC} value approaching 0.9 V as well as remarkable stability at higher temperature for extended periods of time.[105] More recently, efficient, air-stable inverted BHJ solar cells based on PCDTBT fabricated with a low temperature annealed sol−gel-derived ZnO film as an electron transport layer have also been demonstrated.

However, to prepare the tricyclic 2,7-carbazole monomer, 4,4′-dibromobiphenyl must first undergo a nitration reaction followed by a Cadogan ring closure reaction.[106] The relatively long synthetic routes will limit their future commercial application in PSCs. To realize potentially low manufacturing costs, it is critical to obtain readily synthesized polymers from commercial products. In this regard, we focused our attention to the well-known phenothiazine building block, considering the following: (i) Heterocyclic phenothiazine unit is structurally like the carbazole moiety but it contains an additional sulfur atom. As a more powerful electron-rich molecule, the phenothiazine is better suited for the development of enhanced intramolecular charge transfer (ICT) polymers. In addition, its "butterfly" nonplanar structure impedes π-stacking aggregation and intermolecular excimer formation, resulting in diverse optoelectronic applications.[107-111] (ii) Not only is phenothiazine cheap and commercially available but also it can be easily tailored by connecting solubilizing groups to the N atom to improve solubility. This is important since the barrier for preparation of materials in terms of a cost effectiveness must be overcome to realize the commercial potentials of PSCs. (iii) Following oxidation of phenothiazines to phenothiazine-S,S dioxides, the electron-withdrawing sulfones would reduce the electron density in the polymer backbone, most likely rendering it more resistant toward the oxidation while simultaneously tuning the electronic properties. In particular, we hypothesized that the hydrophilicity of the SO_2 groups can promote the compatibility and low contact resistance through the potential interaction with oxides in the inverted BHJ solar cells integrated with metal oxide materials as an electron transport and an hole transport between the ITO/BHJ and BHJ/metal interfaces.

Herein, we report two new polymers incorporating either phenothiazine or its oxidized analogue phenothiazine-S,S dioxide as the donor and benzothiadiazole as the acceptor, namely poly(N-(2-decyltetradecyl)-3,7-phenothiazine-alt-5,5(4′,7′-di-2-thienyl-2′,1′,3′-benzothiadiazole)) (PPTDTBT) and poly(N-(2-decyltetradecyl)-3,7-phenothiazine-S,S-dioxide-alt5,5-(4′,7′-di-2-thienyl-2′,1′,3′-benzothiadiazole)) (PPTDTBTSS), respectively (**Figure 2.1.1**). These polymers are tested in both conventional and inverted solar cell devices using the fullerene derivative (see **Figure 2.1.1a** and **2.1.1b**). We find that PSCs based on PPTDTBT in a conventional architecture can reach PCE as high as 1.69%, whereas the utilization of its oxidized form PPTDTBT-SS into inverted solar cells shows improved performance (PCE = 1.22%), when compared to that of its conventional devices. The results obtained here are very helpful for molecular design strategies to obtain inverted solar cells with higher device performance.

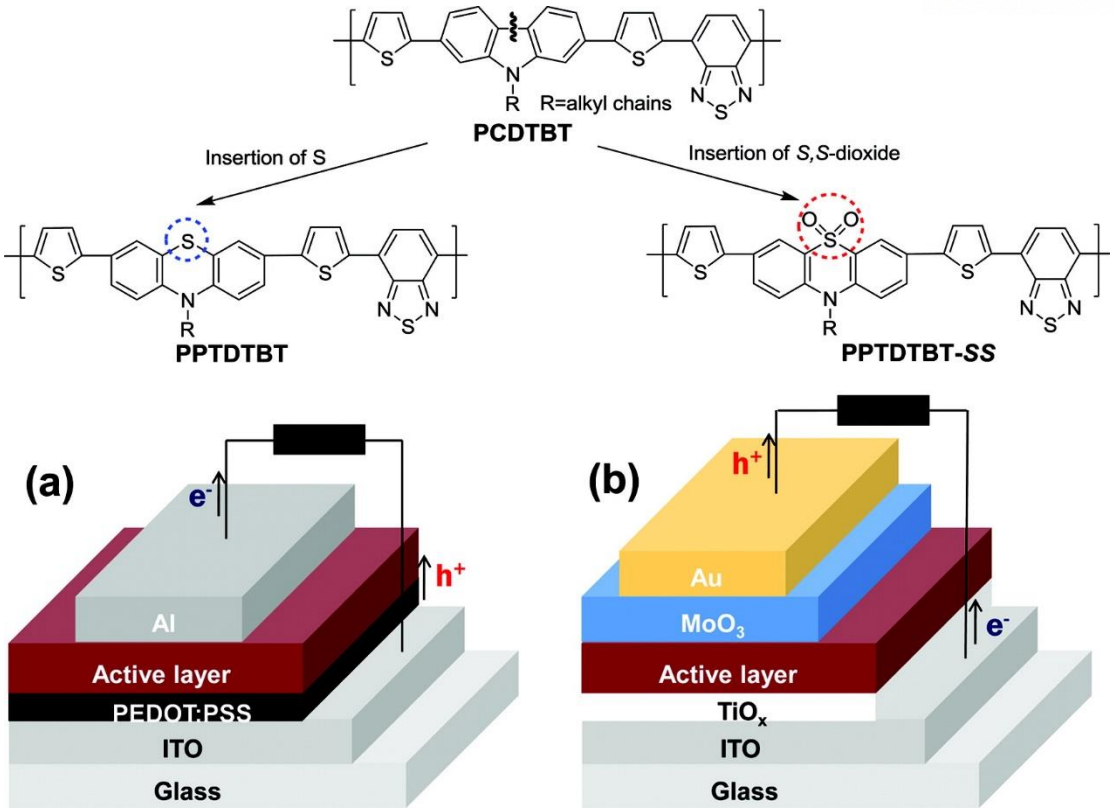

Figure 2. 2. 1. Molecular structures of PCDTBT and phenothiazine-based polymers. Schematic depiction of the conventional structure (a) and inverted structure (b) of the PSCs used by our research group.

2.2.2 Experimental Details

Materials and Instruments. All starting materials were purchased either from Aldrich or Across and used without further purification. THF was distilled over sodium/benzophenone. ^{1}H NMR and ^{13}C NMR spectra were recorded on a Varian VNRS 600 MHz (Varian USA) spectrophotometer using $CDCl_3$ as solvent and tetramethyl silane (TMS) as the internal standard and MALDI MS spectra were obtained from Ultra flex III (Bruker, Germany). UV−vis-NIR spectra were taken on Cary 5000 (Varian USA) spectrometer. Number average (M_n) and weight-average (M_w) molecular weights, and polydispersity index (PDI) of the polymer products were determined by gel permeation chromatography (GPC) with Agilent 1200 HPLC Chem station using a series of mono disperse polystyrene as standards in THF (HPLC grade) at 308 K. Cyclic voltammetry (CV) measurements were performed on AMETEK Versa STAT 3 with a three-electrode cell in a nitrogen bubbled 0.1 M tetra-*n*-butylammonium hexafluorophosphate (*n*-Bu_4NPF_6) solution in acetonitrile at a scan rate of 50 mV/s at room temperature. A used as the Ag/Ag^+ (0.1 M of $AgNO_3$ in acetonitrile) reference electrode, platinum counter electrode and polymer-coated platinum working electrode, respectively. The Ag/Ag^+ reference electrode was calibrated using a ferrocene/ferrocenium redox couple as an internal standard, whose oxidation potential is set at −4.8 eV with respect to zero vacuum level. The HOMO energy levels were obtained from the equation $HOMO = -(E_{ox}^{onset} - E_{(ferrocene)}^{onset} + 4.8)$ eV. The LUMO levels of polymers were obtained from the equation $LUMO = -(E_{red}^{onset} - E_{(ferrocene)}^{onset} + 4.8)$ eV.

OFET Device Preparation and Measurement. All p-type OFETs were fabricated on heavily doped n-type silicon (Si) wafers each covered with a thermally grown silicon dioxide (SiO_2) layer with thickness of 200 nm. The doped Si wafer acts as a gate electrode, and the SiO_2 layer functions as the gate insulator. The active layer was deposited by spin-coating at 2500 rpm. All solutions were prepared at 0.5 wt % concentration in chlorobenzene. The thickness of the deposited films was about 60 nm. Prior to vapor-deposition of source drain electrodes, the films were dried on a hot plate stabilized at 80 °C for 30 min. All fabrication processes were carried out in a glovebox filled with N_2. Source and drain electrodes using Au were deposited by thermal evaporation using a shadow mask. The thickness of source and drain electrodes was 50 nm. Channel length (L) and channel width (W) was 50 μm and 1.5 mm, respectively. Electrical characterization was performed using a Keithley semiconductor parametric analyzer (Keithley 4200) under N_2 atmosphere.

Fabrication of Conventional and Inverted Photovoltaic Cells. Two-type photovoltaic cells were fabricated on ITO-coated glass substrates. The ITO-coated glass substrates were first cleaned with detergent, ultrasonicated in water, acetone and isopropyl alcohol, and dried overnight in an oven. In conventional cells, PEDOT:PSS(Al 4083) was spin-cast on cleaned ITO substrates after a UV-ozone treatment for 15 min and heated at 140 °C for 10 min in air. Subsequently, the active layer was coated

in a glovebox. The solution containing a mixture of PPTDTBT:PC71BM (1:2) in a solvent (chlorobenzene) with a concentration of 11 mg/mL and PPTBTDTSS:PC71BM (1:1.5) in a solvent (dichlorobenzene) with a concentration of 13 g/mL was spin-cast on top of PEDOT:PSS film. After then, the top electrode (Al) was deposited on the active layer in a vacuum ($<10^{-6}$ Torr) thermal evaporator. Inverted solar cells were fabricated on ITO-coated glass substrates. A TiO_x precursor solution was prepared using the sol−gel method. The TiO_x precursor solution was spin-cast on cleaned ITO substrates after a UV-ozone treatment for 15 min and heated at 80 °C for 10 min in air for conversion to TiO_x by hydrolysis. Subsequently, the TiO_x-coated substrates were transferred into a glovebox. A solution containing a mixture of PPTDTBT:PC71BM (1:2) in a solvent (chlorobenzene) with a concentration of 11 mg/mL was spin-cast on top of TiO_x films at 1500 rpm 60 s and PPTBTDT-SS:$PC_{71}BM$ (1:1.5) in a solvent (dichlorobenzene) with a concentration of 13 g/mL was spin-cast on top of TiO_x films at 600 rpm 60 s. Then, a thin layer of MoO3 film (≈5 nm) was evaporated on top of the active layer. Finally, the anode (Au, ≈95 nm) was deposited on the active layer in a vacuum ($<10^{-6}$ Torr) thermal evaporator. The cross-sectional area of each of the electrode defines the active area of the device as 13.5 mm^2. Photovoltaic cell measurements were carried out inside the glovebox using a high quality optical fiber to guide the light from the solar simulator equipped with a Keithley 2635A source measurement unit. The $J-V$ curves for the devices were measured under AM 1.5G illumination at 100 mW cm^{-2}. The IPCE spectra for the PSCs were measured on an IPCE measuring system.

2.2.3 Results and Discussion

Optical and Electrochemical Properties.

The UV−vis spectra of two polymers (PPTDTBT and PPTDTBT-SS) in chloroform solution and solid films on the quartz are shown in **Figure 2.2.2.** PPTDTBT film are characterized with a strong, broad and structureless absorption band at 582 nm, corresponding to the intramolecular charge-transfer (ICT) transition, together with a strong absorption band at shorter wavelength (~ 395 nm) due to higher energy transitions such as π−π* transitions. Notably, such optical features are remarkable similarity to those of the analogous PCDTBT (λ_{max} = 398 and 576 nm), but PPTDTBT has a slightly lower optical band gap (E_g^{opt} = 1.79 eV) from the absorption edge of the thin film than PCDTBT (1.88 eV). Compared to PPTDTBT showing the absorption maxima, PPTDTBT-SS in the solid state exhibits a nearly identical high-energy peak at 387 nm but a hypsochromic shift of the ICT band at 535 nm, resulting in a larger optical band gap (1.95 eV). This indicates that, as expected, the donating strength of phenothiazine-S,S-dioxide that contains the electron-withdrawing sulfonyl group is weaker than that of the phenothiazine moiety, leading to relatively reduced ICT character in PPTDTBT-SS.

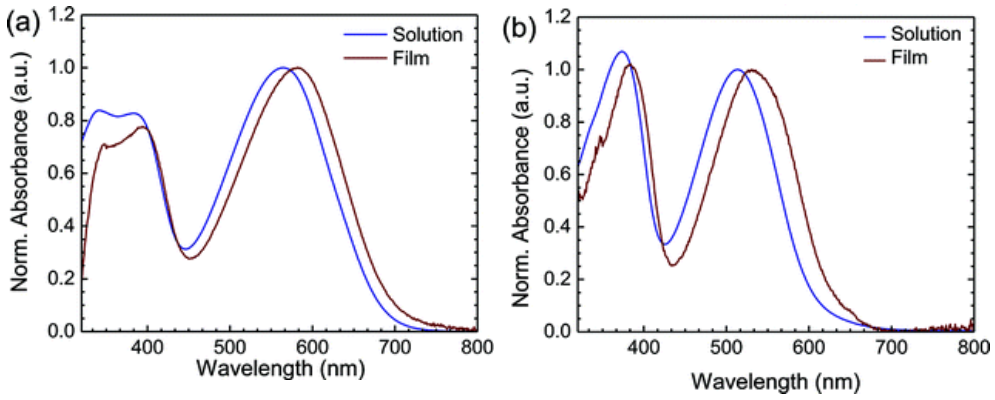

Figure 2. 2. 2. UV-vis absorption spectra of PPTDTBT(a) and PPTDTBT-SS(b).

Electrochemical cyclic voltammetry (CV) was performed to determine the highest occupied molecular orbital (HOMO) and lowest unoccupied molecular orbital (LUMO) energy levels of the polymers (**Figure 2.2.3.**). The CV curves were recorded referenced to an Ag/Ag^+ (0.1 M *n*-Bu_4NPF_6) electrode, which was calibrated by a ferrocene-ferrocenium (Fc/Fc^+) redox couple (4.8 eV below the vacuum level). The HOMO and LUMO energy levels are calculated to be −5.41 and −3.63 eV for PPTDTBT and −5.60 and −3.60 eV for PPTDTBT-SS, respectively. Considering the relatively low HOMO levels of the polymers, a high V_{OC} can be expected.[112-114] The LUMO levels of the polymers are positioned 0.3 eV above the $PC_{71}BM$ (−4.3 eV) to ensure a downhill driving force for charge separation

to $PC_{71}BM$. The electrochemical HOMO−LUMO gaps of the both polymers are very similar to those of optical band gaps. Apparently, the LUMO value of PPTDTBT matches well with that of PCDTBT (−3.6 eV) whereas its higher HOMO level, in comparison with PCDTBT (−5.5 eV), indicates the increase of donor strength due to the insertion of the additional electron-rich sulfur atoms. For PPTDTBT-SS interchanged the phenothiazine with a phenothiazine-S,S-dioxide segment, the HOMO (−5.6 eV) is found to be lower than of that of PPTDTBT owing to the presence of the electron-deficient SO_2 groups in the polymer backbone, which can be beneficial to the better air-stability and higher V_{OC} of the PSCs based on the polymer as donor.[115]

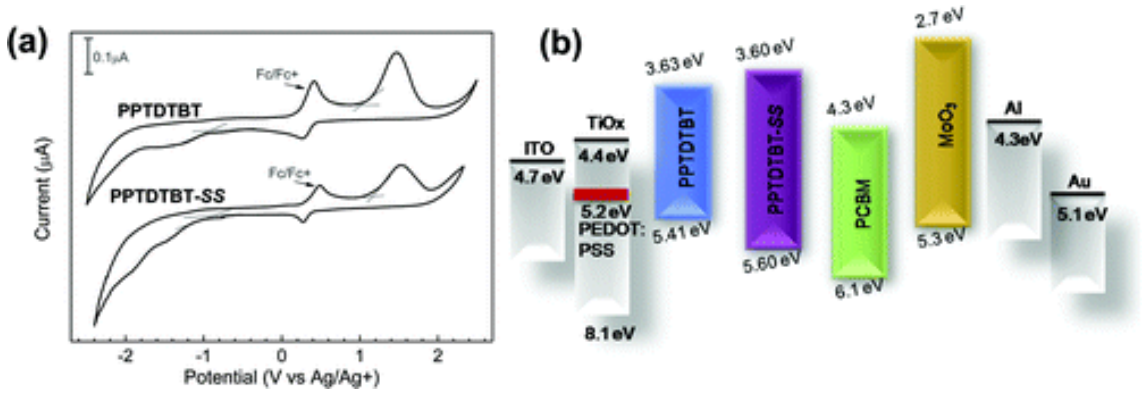

Figure 2. 2. 3. (a) Cyclic voltammograms of PPDTBT (top) and PPDTBT-SS (bottom) thin films on the Pt electrode in 0.1M *n*-Bu_4NPF_6 acetonitrile solution at room temperature. (b) Energy level diagrams of individual layers used in conventional and inverted structure.

X-ray Analyses.

To evaluate the crystallinity of the polymer, X-ray diffraction (XRD) measurements were taken of thick films prepared from chlorobenzene on SiO_2/Si substrate. The thickness of the films was determined to be 1.5−55 μm by profilometry. **Figure 2.2.4.** shows the XRD data of the thin films of PPTDTBT and PPTDTBT-SS, respectively. PPTDTBT-SS reveals a distinct primary diffraction feature at $2\theta = 4.67°$, corresponding to d-spacing of 18.9 Å and a secondary broad peak at $2\theta = 21.2°$ (d = 4.2 Å) related to π−π stacking between the polymer main chains is also observed. Contrastingly, the XRD pattern of PPTDTBT exhibits only the secondary broad peak shifting to 17.51° (d = 5.10 Å). These results suggest a higher structural organization in the solid state for PPTDTBT-SS compared to PPTDTBT.

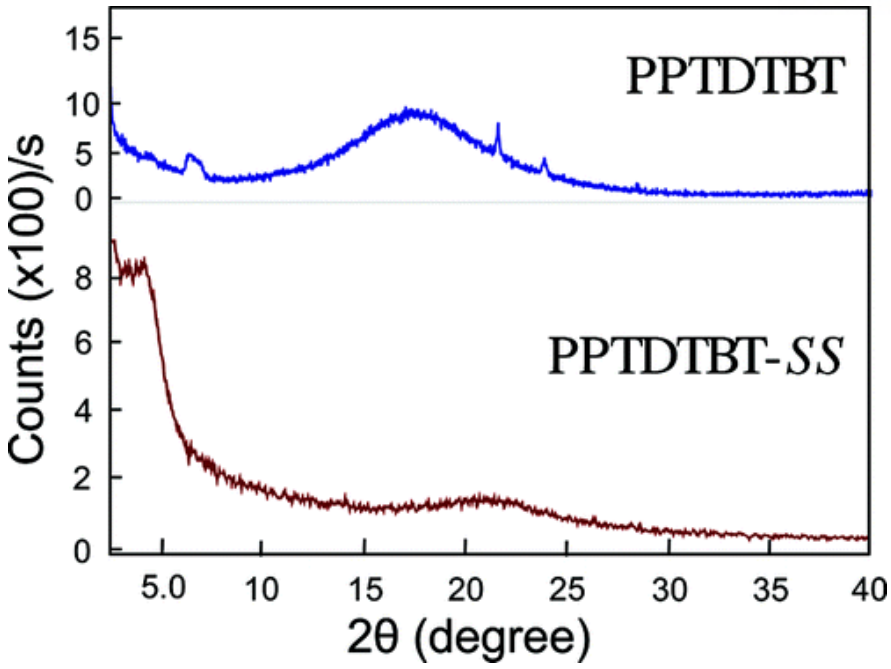

Figure 2. 2. 4. X-ray diffraction (XRD) patterns of drop-cast films of polymers on SiO_2/Si substrates.

Organic Field Effect Transistors.

To investigate the potential of the two new polymers in plastic electronics, organic field-effect transistors (OFETs) were fabricated in the top contact geometry as described in the Experimental Section (**Figure 2.2.5.**). **Figure 2.2.5.b** shows the transfer characteristics, $|I_{ds}|$ vs V_{gs} and $|I_{ds}|^{1/2}$ vs V_{gs} (both at V_{ds} =−60 V), of OFETs fabricated using PPTDTBT and PPTDTBT-SS, respectively, as the active layer. These I_{ds} vs V_{gs} curves obtained from both PPTDTBT and PPTDTBT-SS exhibit clear signature of p-type behavior. The saturated charge carrier mobilities of the polymers are calculated using the saturation current equation: $I_{ds}= (\mu WC_i/ 2L)(V_{gs} - V_T)^2$.[116] An hole mobility (μ) as high as 9.8×10^{-5} $cm^2\ V^{-1}\ s^{-1}$ (threshold voltage (V_T)=−11.5 V) with a current on/off ratio (I_{on}/I_{off}) of 2.5×10^2 is estimated for OFETs produced from PPTDTBT. Interestingly, despite the insertion of the electron-deficient SO_2 groups as well as the relatively lower molecular weight, the hole carrier mobility is increased by about 1 order of magnitude in PPTDTBT-SS OFETs (μ = 6.9 × 10−4 $cm^2\ V^{-1}\ s^{-1}$, V_T = −21.0 V, I_{on}/I_{off} = 7.7 × 10^2), compared to PPTDTBT. Although a concrete evidence of the high performance with PPTDTBT-SS OFETs is lacking at this stage, we think this is partially contributed either from (i) the reduced contact resistance between the semiconductor and the source/drain electrodes arising from the favorable interfacial dipoles between S,S-dioxide groups and Au electrodes or (ii) the well-interconnected thin film morphology due to the interaction between the polar S,S-dioxides. The enhanced intermolecular interactions would bring the polymer chain into a proximity as evidenced by the XRD results, which can facilitate charge hopping in the polymer.

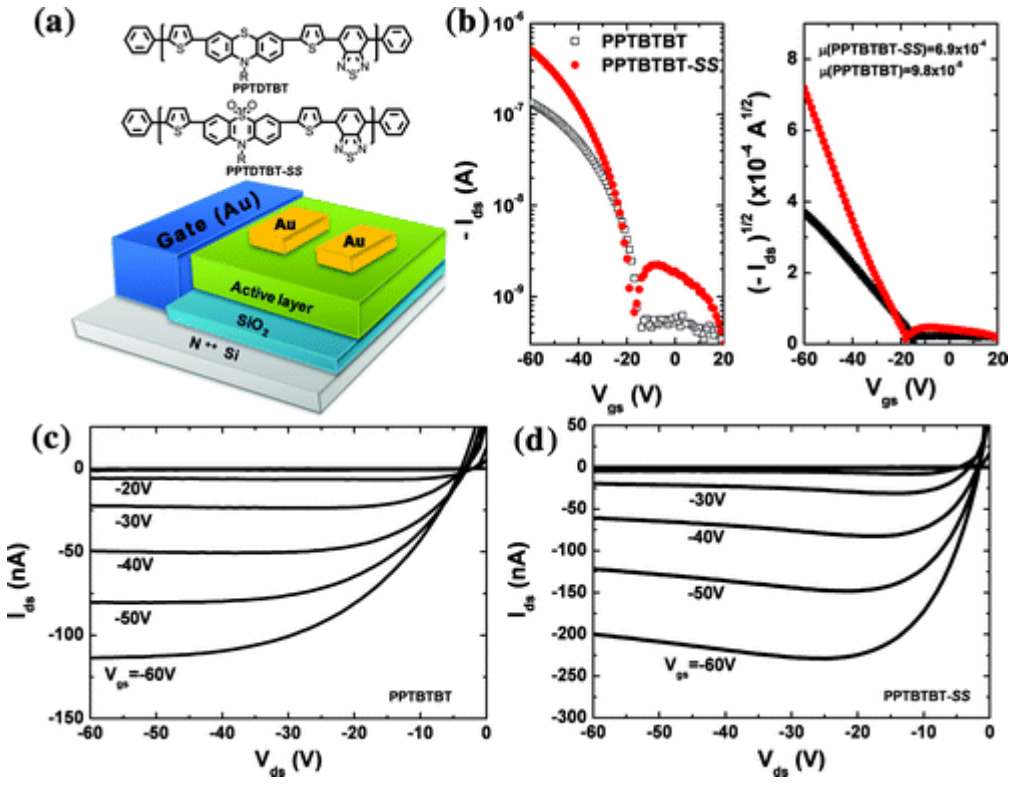

Figure 2. 2. 5. (a) Chemical structures of the polymers and schematic representation of OFERs structure (L = 50μm, W = 1.5mm). (b) Transfer curves in saturated regime with PPTDTBT (black line) and PPTDTBT-SS (red line). The output characteristics of PPTDTBT (c) and PPTDTBT-SS (d), respectively.

DFT Electronic Structure Calculations.

To shed light on the difference in the electronic properties and energies of frontier orbitals between the two polymers, computational studies using density functional theory (DFT) approaches were carried out. Oligomers $(PTDTBT)_n$ and $(PTDTBT\text{-}SS)_n$ with n = 1 and 2 were subjected to the calculations, with the alkyl chains replaced by methyl groups for simplicity. The optimized geometries and electron density distributions of the polymers were calculated with the B3LYP function and 6-31G* basis. As shown in **Figure 2.2.6.**, the HOMO iso-surfaces of the both $(PTDTBT)_n$ and $(PTDTBT\text{-}SS)_n$ are well spread over the whole conjugated backbones, whereas the LUMOs are mainly localized on BT units, respectively, which verifies the p-type behaviors obtained from the OFET study. In addition, the calculated bandgaps for $(PTDTBT)_2$ (1.80 eV) and $(PTDTBT\text{-}SS)_2$ (1.99 eV) are in considerable coincidence with the electrochemical analyses above. It is found that the phenothiazine and phenothiazine-S,S-dioxide rings are folded along the S···N vector, having the aspect angles of 21° and

15°, respectively, in qualitative agreement with their single crystal X-ray diffraction studies. We note a relatively larger dihedral angle between PT and DTBT-SS units (θ = 160°) in the optimized geometry, when compared to that between PT and DTBT (θ = 153°). So it can be seen from the data that the coplanarity of PPTDTBT-SS is better than that in PPTDTBT. This implies that the backbone of PPTDTBT-SS brings about larger effective π–π interactions in the solid state, which matches qualitatively well with the XRD data. Furthermore, this can explain satisfactorily our interpretation of the better PPTDTBT-SS OFET results above.

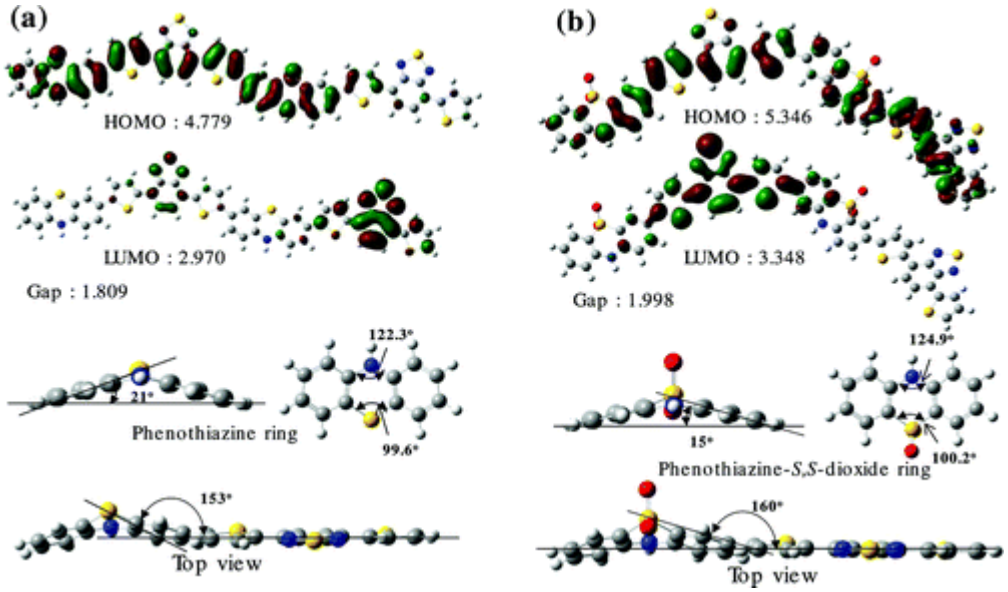

Figure 2. 2. 6. DFT-optimized geometries and charge-density isosurfaces for the HOMO and LUMO levels of (a) $(PTDTBT)_2$ and (b) $(PTDTBT\text{-}SS)_2$ model systems (top) and optimized structures of phenothiazine and phenothiazine-S,S-dioxide rings and their top views, respectively (bottom).

Polymer Solar Cells.

To demonstrate potential applications of the two polymers in PSCs, we used PPTDTBT and PPTDTBT-SS as an electron donor and PC71BM as an electron acceptor and fabricated conventional PSCs with a BHJ structure of ITO/PEDOT:PSS/polymers:PC71BM/Al. The focus of the current study is to elucidate the improved device performance of inverted PSCs by introducing SO2 functionality in the polymer backbone through potential interaction with oxide materials. Thus, the PSCs with inverted configuration stacked from bottom to top (ITO/TiOx/ polymers:PC71BM/MoO_3/Au) were also prepared, where MoO3 as the hole transport layer and TiOx as the electron transport layer were deposited. TiOx was employed as the electron selective layer due to its high electron affinity (LUMO = ~4.4 eV).[117] Since the valence band edge of TiOx is much lower than those of HOMOs of both the polymers and PC71BM, the TiOx layer serves also as a hole blocking layer. Similarly, the MoO3 layer

was used to block the electron flow because of its small electron affinity and to enhance hole transport to the anode.[118] The device structures of regular and inverted polymer solar cells are shown in **Figure 2.2.1. a** and **b**, and **Figure 2.2.3.b** illustrates the energy level diagrams for each component, respectively. All data were obtained under white light AM1.5G illumination from a calibrated solar simulator with irradiation intensity of 100 mW/cm2. The active layers through a very broad altering range from 1:1 to 1:4 (w/w) of polymer:$PC_{71}BM$ in either chlorobenzene (CB) or odichlorobenzene (ODCB) were evaluated. The optimized weight ratios of polymer to PC71BM for PPTDTBT and PPTDTBT-SS are 1:2 and 1:1.5, respectively. Device current density/voltage ($J-V$) characteristics are shown in **Figure 2.2.7.** and the parameters listed in **Table 2.2.1**.

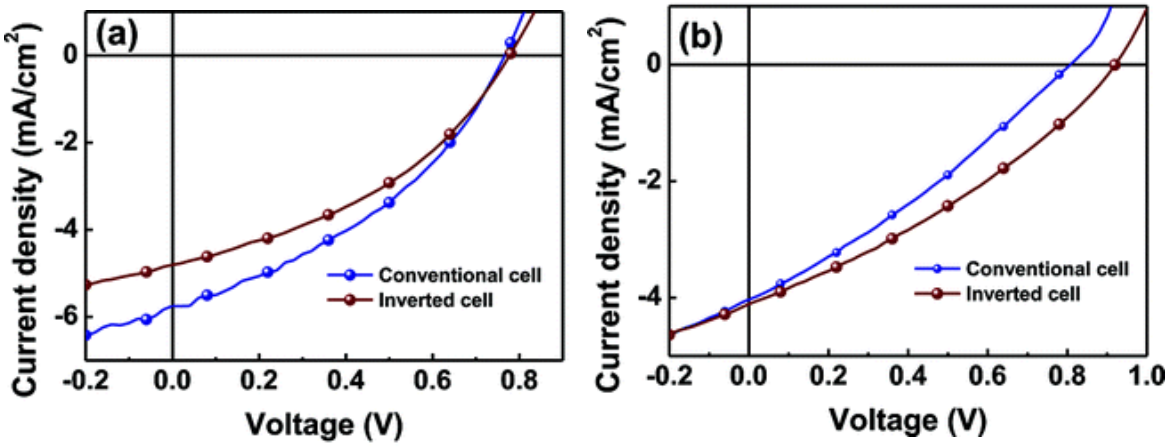

Figure 2. 2. 7. J-V characteristics of the PSCs based on PPTDTBT (a) and PPTDTBR-SS (b) under illumination of AM 1.5G, 100mW/cm^2.

Table 2. 2. 1. Photovoltaic performance of blends of the polymers with fullerenes.

Device structure	Composite	d^a (nm)	J_{SC} [mA/㎠]	V_{OC} [V]	*FF*	PCE [%]
Conventional	PPTDTBT:$PC_{71}BM$ (1:2)	50	5.75	0.77	0.38	1.69
	PPTDTBT-SS:$PC_{71}BM$ (1:1.5)	50	4.03	0.81	0.30	0.97
Inverted	PPTDTBT:$PC_{71}BM$ (1:2)	28	4.80	0.78	0.39	1.47
	PPTDTBT-SS:$PC_{71}BM$ (1:1.5)	32	4.11	0.92	0.32	1.22

[a]Thickness of the active layer.

PCEs up to 1.69% is observed for the conventional PPTDTBT:PC71BM solar cells with a VOC of 0.77 V, a short circuit current density (J_{SC}) of 5.75 mA cm^{-2}, and a fill factor (FF) of 38%. Under the same white light illumination, the PPTDTBT-SS:PC71BM-based regular cell exhibits a J_{SC} of 4.03 mA cm^{-2},aVOC of 0.81 V, and a FF of 30%. It yields a substantially lower PCE of 0.97% because of its decreased photocurrent, when compared to that of PPTDTBT:PC71BM. This can be mainly attributed to PPTDTBT-SS's intrinsic absorption limit in the visible region due to the relatively large energy bandgap. It is worthy to mention that as expected from the oxidation potential, the VOC for the cell with PPTDTBT-SS is higher than that of PPTDTBT.

Despite the aforementioned advantages of the inverted cells, the majority studies on the inverted cells were based on P3HT as active materials,[119] while only few new conjugated polymers had been tested in such configuration.[120, 121] Therefore, comparison of the photovoltaic properties of new materials in both conventional and inverted cells is very important to fully evaluate the performance of new polymers. The J−V curves for the inverted polymer solar cells obtained under white light illumination (AM1.5 G, 100 mW/cm^2) are shown in **Figure 2.2.7.** The corresponding PCE is 1.47 and 1.22% for PPTDTBT:PC71BM and PPTDTBT-SS:PC71BM, respectively (**Table 2.2.1.**). In the both inverted devices, despite the fact that the absorption spectra of the active layer films in the two device types are identical, a decrease in the J_{SC} (4.80 mA cm^{-2} for PPTDTBT:PC71BM and 4.11 mA cm^{-2} for PPTDTBTSS:PC71BM, respectively) is clearly observed, resulting the low overall performances. One possible explanation for this phenomenon is that, in the inverted cell, a small fraction of the incident light is observed by the evaporated Au top electrode. It is roughly estimated that 30% of the incident light with wavelength <650 nm is not absorbed by the active layer on the first pass, so clearly the reflectivity of the top electrode plays a non-negligible role in the total number of photons absorbed by the blend. Thus, it is plausible that the enhanced reflectivity of the Al electrodes used in the normal cell causes the photocurrent to be slightly higher.[122]

Surprisingly, in contrast, the inverted cell of PPTDTBTSS:PC71BM exhibits a slight improved J_{SC} and a much higher VOC value (0.92 eV) than that of the conventional configuration with PPTDTBT:PC71BM, which suggests that the recombination behavior and morphology are different for the two architectures. A likely rationale for this positive effect may be attributed to a combination of the following factors: The hydrophilicity of SO_2 groups would facilitate intimate contact on both the electrodes and thus facilitate efficient charge transfer between the active layer and the electrodes. In addition, we cannot rule out that the dipole moment induced by the polar SO_2 units in PPTDTBT-SS could be the origin of the improvement in the device performance since a higher VOC can indicate a larger electrostatic field across the device structure, although other explanations are still possible. Further investigation of these films using electrostatic force and surface potential microscopy in underway.

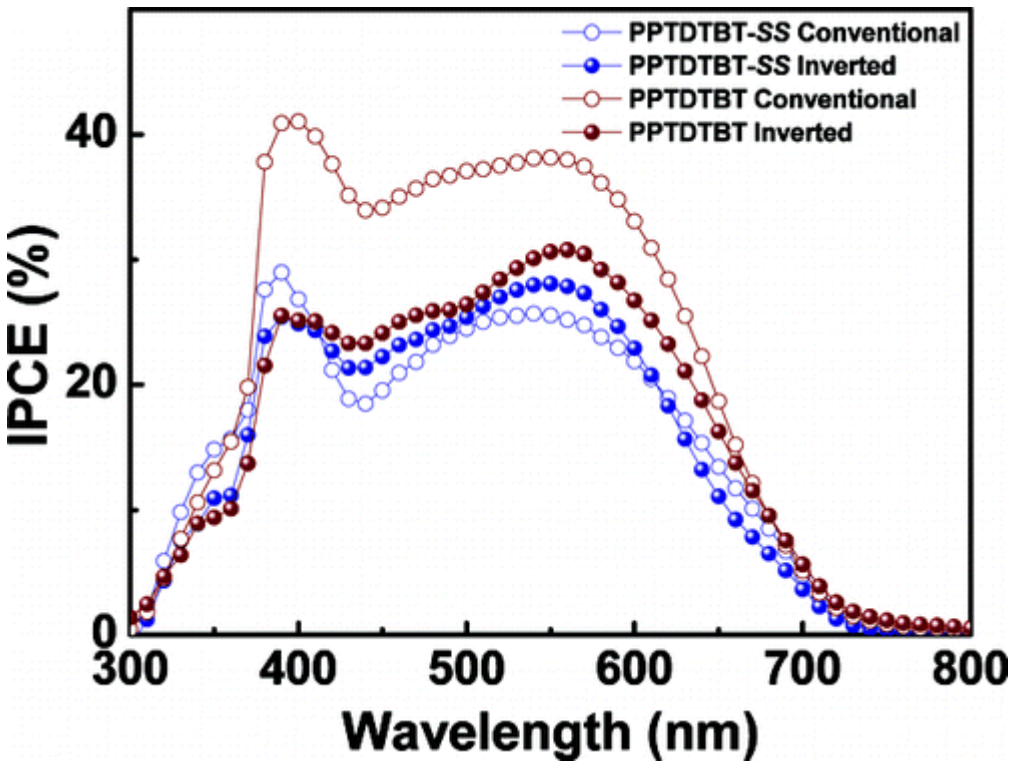

Figure 2. 2. 8. Incident photon-to-current efficiency (IPCE) spectra of the polymer:PC71BM solar cells.

The accuracy of the photovoltaic measurements can be confirmed by the incident photon-to-electron conversion efficiency (IPCE) of the devices. **Figure 2.2.8.** shows the IPCE curves of both the conventional and inverted PSCs fabricated under the optimized conditions as those used for the J−V measurements. All devices show a broad photoresponse spreading from 300 to 700 nm, with maximum around 570 nm. However, the IPCE of the device is within 40% for almost the whole absorption range. From this observation, we believe that the IPCE of the devices can be improved by increasing the thickness of the active layer without hampering charge separation and transport properties. However, because of their limited solubility for the fabrication of practical PSCs, it is difficult to obtain high thickness for the active layer by using high concentration of the polymer blends. Currently, the preparation of dithienylbenzothiadiazole with two flexible alkoxyl chains to improve solubility is ongoing. Obviously, the IPCE value for the conventional PPTDTBT:PC71BM is the highest, which agrees with the highest J_{SC} value of the devices. To evaluate the accuracy of the photovoltaic results, the J_{SC} values were calculated by integrating the IPCE data with the AM 1.5G reference spectrum. The J_{SC} values obtained using integration and J-V measurements are rather close (within 7% error), which indicates that the photovoltaic results are reliable.

Morphology. The nanoscale morphologies of both the conventional and inverted polymer/PC71BM films were studied using tapping-mode atomic force microscopy (AFM). Surface topography (left) and phase images (right) were taken for each film and are shown in **Figure 2.2.9**. Both the regular and inverted PPTDTBT:PC71BM blends are very similar and exhibit a rather uniform smooth film formation which suggests the absence of large features that might reduce the interface between polymer and fullerene potentially limiting device performance.[123, 124] In contrast, PPTDTBT-SS:PC71BM blends in both conventional and inverted structures (**Figure 2.2.9**, **c** and **d**) give very inhomogeneous features in which voids with a diameter of ~300 nm are present. This indicates poor miscibility between PPTDTBT-SS and PC71BM. This implies that the presence of SO_2 groups makes PPTDTBT-SS strongly hydrophilic, which is, in large part, responsible for the relatively low PCEs in the conventional cells, but this can positively affect the inverted PSCs adopting transporting metal oxides between the ITO/ BHJ and BHJ/metal interfaces because of the potential interaction with oxides. This observation is in good agreement with the J-V characteristics tested in this study.

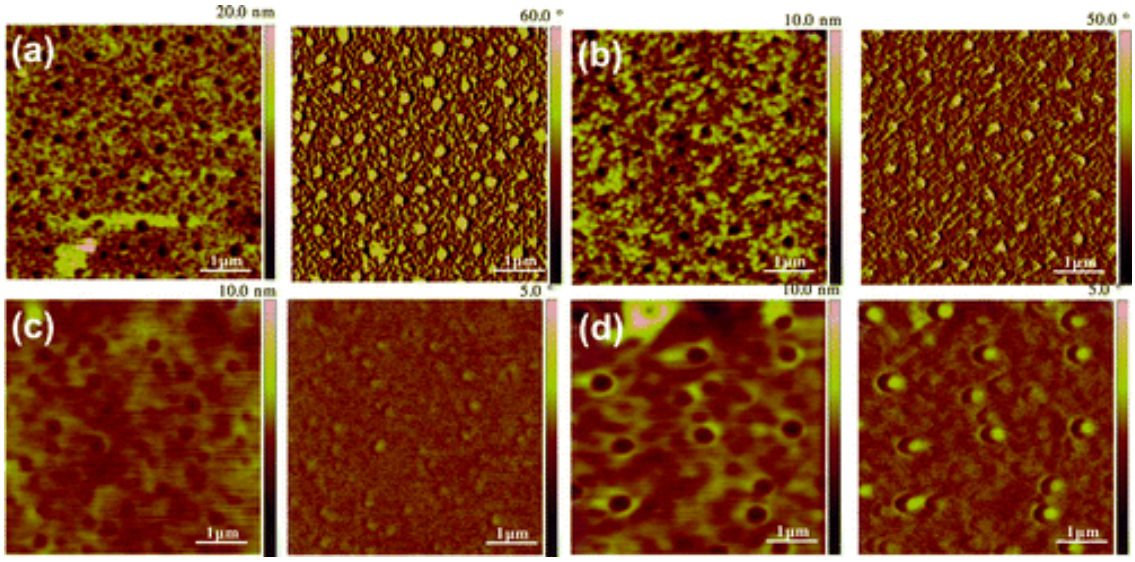

Figure 2. 2. 9. Tapping-mode AFM images (5μm x 5μm) of PPTDTBT:PC71BM (conventional (a); inverted (b)) and PPTDTBT-SS:PC71BM (conventional (c); inverted (d)) films used in making the devices (under optimized device conditions). The topography of each film is shown in the left panels, and the corresponding phase images in the right panels.

2.2.4 Conclusion

Considering low cost PSCs into account, an easily accessible donor, phenothiazine, which is stronger than commonly used 2,7-carbazole donors due to an additional sulfur atom, has been copolymerized with electron-deficient benzothiadiazole building block to yield new conjugated polymer PPTDTBT. By virtue of the enhanced strength of ICT, the "strong donor− acceptor" polymer (PPTDTBT) shows more bathocromically shifted absorption spectrum (λ_{max} = 582 nm) and lower band gap (E_g^{elec} = 1.78 eV) in comparison with its analogous polymer (PCDTBT) that in particular has been subject to increasing interest in the polymer research community. Through the sulfur oxidation in the phenothiazine unit, the corresponding oxidized form polymer PPTDTBT-SS is also prepared and characterized in parallel following our design motif. The strong polarity of SO2 groups would enhance the compatibility and low contact resistance in the inverted BHJ solar cells integrated two metal oxides. Both the PPTDTBT and PPTDTBT-SS show moderate mobilities as p-type polymer semiconductors in OFETs. Interestingly, the carrier mobility of PPTDTBT-SS is about 1 order of magnitude higher than that of PPTDTBT, which is presumably ascribed to the closer packing driven either from the dipolar intermolecular interactions associated with the presence of the sulfonyl groups or the relatively enhanced coplanarity of PPTDTBT-SS, supported by the DFT calculations as well as XRD results. The performance of the PSCs containing the polymer PPTDTBT reaches PCEs of 1.69% and 1.47% for conventional and inverted structure devices when using PC71BM as electron acceptor, respectively.

On the other hand, despite the fact that relatively low-lying HOMO of PPTDTBT-SS enhances the V_{OC}, the current density in the PPTDTBT-SS:PC71BM-based regular cell is low and limits the PCE to 0.97%. This is likely a consequence of a reduced solar absorption of PPTDTBT-SS's caused by the relatively large energy bandgap. Delightfully, when it comes to incorporating PPTDTBT-SS into the inverted configuration cell with TiOx and MoO_3 as electron-selective and hole selective layers, respectively, the estimated PCE of 1.22% is achieved from the combination with the improved V_{OC} and J_{SC}. Current work on π-conjugated polymer structural modification has been aimed at understanding the influence of polymer polarity in inverted solar cells. Our results indicate that the introduction of *S,S*-dioxide units into the polymer backbone is a useful strategy for the design of high performance inverted solar cells.

2.3. A Selenophene Analogue of PCDTBT: Selective Fine-Tuning of LUMO to Lower of the Bandgap for Efficient Polymer Solar Cells[249]

2.3.1 Research Backgrounds

With deep understanding of efficient photoinduced electron transfer within an interpenetrating network by simple blending π-conjugated polymers (electron donor) with fullerene derivatives (electron acceptor),[125] bulk-heterojunction (BHJ) polymer solar cells (PSCs) based on poly(3-hexylthiophene) (P3HT):[6,6]-phenyl C61-butyric acid methyl ester (PCBM) have been extensively investigated, leading to great progress in power conversion efficiencies (PCEs) of 4−5%.[126, 127] Yet, the PCE of P3HT-based PSCs is limited by its relatively large bandgap (~1.9 eV) with major loss of the solar radiation as well as low open circuit-voltage (V_{OC} ≅ 0.6 V) due to the relatively small energy difference between the highest occupied molecular orbital (HOMO) of P3HT and the lowest unoccupied molecular orbital (LUMO) of PCBM. By taking into consideration using low bandgap polymers to harvest more solar photons, researchers have devoted much effort recently to reducing the bandgap of polymers. This approach has provided a remarkable short-circuit current density (J_{SC}) of 16 mA/cm^2,[128] whereas, in general, the V_{OC} has suffered[129] because of a higher than the HOMO optimal energy level in order to pursue a lower bandgap. In the PSCs community, poly(2,7-carbazole-altdithienylbenzothiadiazole) (PCDTBT) is one excellent example for a low HOMO (−5.45 eV) as required by the 'ideal' π conjugated polymers, which led to a high V_{OC} value over 0.8 V and outstanding stability against oxidation at high temperatures.[130-132] The initial PCE reached 3.6%[133] in a typical BHJ device and has been subsequently improved to exceeding 6% by BHJ layer thickness optimization and nanomorphology control using mixed solvent mixtures.[134, 135] However, the bandgap of PCDTBT is still relatively larger than the proposed 1.5−1.7 eV of the ideal polymers for PCEs exceeding 10%. Recently, to further lower the bandgap of PCDTBT without sacrificing its high V_{OC}, Hsu et al.[136, 137] and our group[138] independently reported PCDTBT-based ladder-type polymers with forced planarity of which device performance showed impressive PCEs of up to 4.59% with reduced bandgap (ca. 0.2 eV) in comparison with that of PCDTBT. However, the multiple synthetic steps for the ladder-type PCDTBTs have restricted the realization for their usage in BHJ devices. Herein, we present an easily obtainable selenophene analogue of PCDTBT, namely, poly(2,7-carbazole-alt-diselenienylbenzothiadiazole) (PCDSeBT) by replacing thiophenes with selenophene rings in the polymer backbone. Such a structural modification would be expected the lower-lying LUMO with the HOMO being largely unaffected due to the individual effects of the smaller ionization potential (IP) and almost the same electronegativity of selenium relative to sulfur atom.[139] In addition, interchain-charge transfer should be facilitated by intermolecular Se···Se contacts, most likely leading to a widen absorption band and enhanced mobility that are desirable for

high photocurrents.[140] Our preliminary investigation on the photovoltaic properties of PCDSeBT in typical BHJ devices with [6,6]-phenyl C71-butyric acid methyl ester (PC71BM) shows a highly respectrable PCE of 4.12% on account of the high J_{SC} and VOC.

2.3.2 Experimental Details

Materials and Characterization. Compounds 1, 2, 3, and 4 were synthesized according to the previously reported procedures.1,2 All starting materials were purchased either from Aldrich or Acros and used without further purification. THF was distilled over sodium/ benzophenone. 1 H NMR spectra were recorded on a Varian VNRS 600 MHz (Varian USA) spectrophotometer using $CDCl_3$ as solvent and tetramethylsilane (TMS) as the internal standard. UV−vis spectra were taken on the Cary 5000 (Varian USA) spectrometer. Number-average (M_n) and weight-average (M_w) molecular weights, and polydispersity index (PDI) of the polymer products were determined by gel permeation chromatography (GPC) with Agilent 1200 HPLC Chemstation using a series of mono disperse polystyrene as standards in THF (HPLC grade) at 308 K. Cyclic voltammetry (CV) measurement was performed on AMETEK VersaSTAT 3 with a three-electrode cell in a nitrogen bubbled 0.1 M tetra-*n*-butylammonium hexafluorophosphate (*n*-Bu_4NPF_6) solution in acetonitrile at a scan rate of 50 mV/s at room temperature. A used as the Ag/Ag^+ (0.1 M of $AgNO_3$ in acetonitrile) reference electrode, platinum counter electrode and polymer coated platinum working electrode, respectively. The Ag/Ag^+ reference electrode was calibrated using a ferrocene/ferrocenium redox couple as an internal standard, whose oxidation potential is set at −4.8 eV with respect to zero vacuum level. The HOMO energy levels were obtained from the equation HOMO = $-(E_{ox}^{onset} - E_{(ferrocene)}^{onset} + 4.8)$ eV. The LUMO levels of polymers were obtained from the equation LUMO = $-(E_{red}^{onset} - E_{(ferrocene)}^{onset} + 4.8)$ eV.

Fabrication of Photovoltaic Cells. Polymer solar cell devices were fabricated according to the following procedure: First, the ITO coated glass substrate was cleaned with detergent, then ultrasonicated in distilled water, acetone and isopropyl alcohol, and then dried overnight in an oven at the 100 °C. Poly(3,4- ethylenedioxythiophene):poly(styrenesulfonate) (PEDOT:PSS) (Baytron PH) was spin-cast at 5000 rpm for 40s. The substrate was then dried for 10 min at the 140 °C in the air. Subsequently, it is moved into a glovebox for spin-coating the active layer. A mixed solution of PCDSeBT:$PC_{71}BM$ in o-dichlorobenzene (DCB) was then spin coated at 700 rpm for 60s on top of the PEDOT:PSS layer to obtain a BHJ film. Those samples were brought into a vacuum system (about 10^{-7} Torr), and an Al electrode (100 nm) was deposited on top of the BHJ layer. Typical devices were thermally annealed in a Petri dish. Thermal annealing was carried out by directly placing the completed devices on a digitally controlled hot plate at 150 °C, in a glovebox filled with nitrogen gas and after annealing. The devices were put on a metal plate and cooled to room temperature. Measurements were carried out with the solar cells inside the glovebox by using a high quality optical fiber to guide the light from the solar simulator equipped with a Keithley 2635 A source. The solar cell devices were illuminated at an intensity of 100 mW/cm^2. For more accurate information the IPCE measurements were carried out with QEX7. The device structure of the hole and electron only devices are ITO/ PEDOT:PSS/ PCDSeBT :PC $_{71}$ BM/Au and FTO/ PCDSeBT:PC71BM/Al, respectively. The space-

charge-limited current (SCLC) mobilities were estimated the Mott-Gurney square law $J_{SCLC} = 9/8 \times \varepsilon_r\varepsilon_0 \times \mu(V^2/L^3)$, where ε_r is the dielectric constant of the material, ε_0 is the permittivity of free space, L is the distance between the cathode and anode, which is equivalent to the film thickness, and V is the applied voltage.

OFET Device Preparation and Measurement. Highly doped n+ - Si wafers were used as substrates, and a layer of 200 nm of silicon dioxide (SiO_2:grown by thermal oxidation) was used as the gate dielectric layer. Au (60 nm) was successively evaporated with shadow mask to obtain source and drain electrodes. The interdigitated structure of the source-drain contacts determined a channel length of 50 μm and a channel width of 2950 μm. Substrates were cleaned by acetone, isopropanol and dried at 100 °C oven for 20 min, and treated with octadecyltrichlorosilane (OTS) at room temperature for over 12 h to treat the surface. Organic semiconductor layers (60 nm) were deposited by spin-coating at 1500 rpm. All fabrication processes were carried out in a glovebox filled with N_2. Electrical characterization was performed using a Keithley semiconductor parametric analyzer (Keithley 4200-SCS) under N_2 atmosphere. The electron mobility (μ) was determined using the following equation in the saturation regime; $I_{ds} = (WC_i/2L) \times \mu \times (V_{gs} - V_{Th})^2$, where C_i is the capacitance per unit area of the SiO_2 dielectric (C_i = 15 nF/cm^2) and V_{Th} is the threshold voltage.

2.3.3 Results and Discussion

As shown in **Figure 2.3.1a**, the UV−vis absorption spectra of PCDSeBT both in chloroform solution and solid state exhibit two distinct absorption bands, as typically observed for donor (D)-acceptor (A) low bandgap materials. The absorption maxima (λmax) of the film are located at 403 and 589 nm. The shorter absorption band is due to π−π* transitions of the polymer backbone,[141] while the lower-energy peak is attributed to intramolecular charge transfer (ICT) in the electron-rich and electron-deficient units.[142,143] It is worth noting that the maxima absorption values of PCDSeBT in the film are slightly broadened without any obvious red-shift when compared to the solution. This verifies that only a small reorganization via π−π stacking between the polymer chains is within view during the film formation because of the interchain aggregates in solution.[144] This observation is in contrast to many conjugated polymers, in which there is a red-shift that occurs in going from the solution to the solid state due to the aggregation of the polymer chains in the solid state,[145] even the PCDTBT film is red-shifted by 30 nm vs solution. Besides, the deep blue color of PCDSeBT solution is observed unlike the red color of PCDTBT in solution (see the digital photograph in **Figure 2.3.1a**).

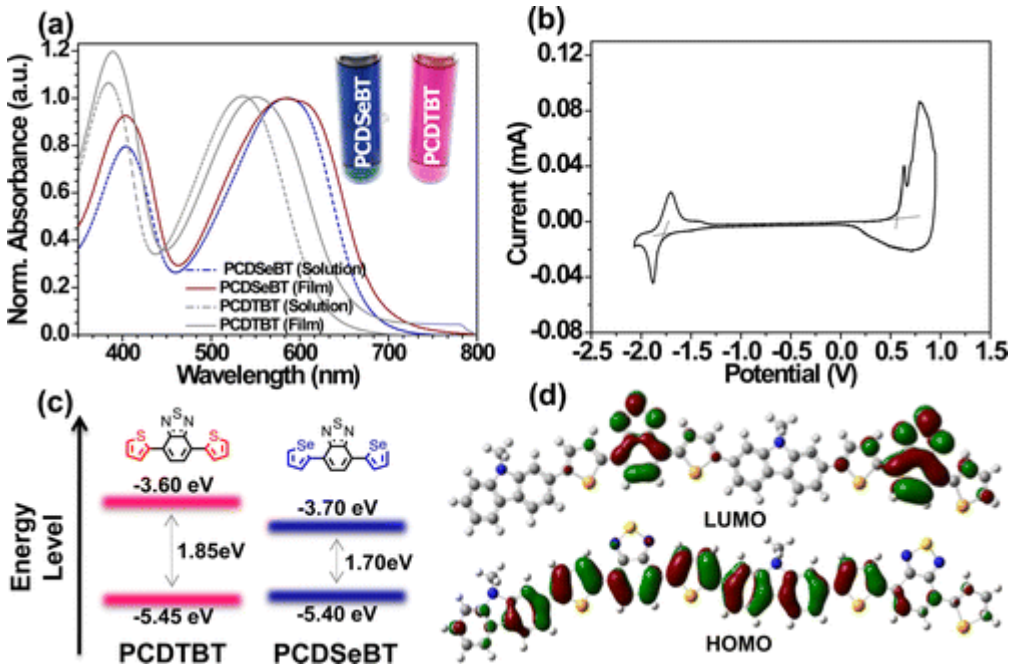

Figure 2. 3. 1. UV–vis absorption spectra of PCDSeBT in chloroform and the thin film on the quartz (a). Inset: images of PCDSeBT and PCDTBT in chloroform solutions. Cyclic voltammogram of PCDSeBT thin film (b). Energy-level diagrams of PCDSeBT and PCDTBT (c). Graphical representation of a methyl-substituted CDSeBT dimer (d).

Notably, although the absorption profile of PCDSeBT is similar to that of the thiophene analogue, PCDTBT, the absorption onset of PCDSeBT is significantly red-shifted by ~70 nm, corresponding to a lower optical bandgap (Eg opt = 1.70 eV) than PCDTBT (Eg opt = 1.85 eV). This apparently demonstrates that, in agreement with earlier studies and experimental studies,[146,147] the replacement of thiophene with selenophene results in a reduction of the optical bandgap due to the increase of quinoid character in the polymer backbone.[148-150] In a closer look of the film absorptions, it is also found that the full width at half-maximum (FWHM) of PCDSeBT (155 nm) is wider than that of PDCTBT (140 nm), as a matter of a characteristic of strong intermolecular Se···Se interactions, which can potentially further increase J_{SC} value. The electrochemical properties of PCDSeBT were investigated by cyclic voltammetry (CV). As shown in **Figure 2.3.1b**, PCDSeBT exhibits clear reversible n-doping/dedoping processes in the negative potential range, whereas quasi-reversible p-doping/dedoping behaviors in the positive potential range are observed. The HOMO and LUMO energy levels are estimated to be −5.40 eV and −3.70 eV, respectively, using the ferrocene-ferrocenium (Fc/Fc+) redox couple (4.8 eV below the vacuum level). Both PCDTBT and PCDSeBT have nearly identical HOMO energy levels, but PCDSeBT exhibits 0.10 eV lower-lying LUMO level relative to PCDTBT (LUMO = −3.60 eV), verifying our presumption about the effect of selenium on the selective fine-tuning of LUMO level. The material-design rules described by Scharber et al.[151] Suggested that the PCEs of a BHJ solar cell should be much more sensitive to changes of the donor LUMO level compared to variations of the donor bandgap. On the basis of the rules, the estimated PCE from the Eg opt and the LUMO value of PCDSeBT is 7.8%. This theoretical value is much higher than that of PCDTBT (6.5%), indicating that a highly promising material for PSCs considering the frontier orbital energies. Upon utilizing a model dimeric system containing methyl groups, the optimized molecular geometry of PCDSeBT and its frontier molecular orbitals of the calculated HOMO and LUMO iso-surfaces were computed by density functional theory (DFT, B3LYP/6-31G) (**Figure 2.3.1d**). The HOMO of PCDSeBT is well-distributed along the conjugated chains; its LUMO is mainly centralized on BT accepting core as shaped by orbital lobes, being predicted a p-type organic semiconductor. In order to corroborate the effect of the heteroatom substitution on charge transporting properties of the polymers, top-contact organic field-effect transistors (OFETs) were fabricated using solution processed PCDTBT and PCDSeBT, respectively, as the semiconducting layer on the octadecyltrichlorosilane (OTS) self-assembled monolayer (SAM)-modified Si/SiO2 substrates (see the detailed devices fabrication in the Experimental Section). The OFET mobilities are calculated in the saturation regime using the following equation: $I_{ds} = (W/2L) \times \mu \times C_i (V_{gs} - V_{th})^2$, where W and L are the channel width and length, respectively, C_i is the capacitance per unit area of the insulation layer. Linear plot of Ids 1/2 vs V_{gs} deduced from the I_{ds} vs V_{gs} measurement. These devices show characteristics of a typical p-channel transistor with good drain-current Modulation, well-defined linear, and saturation regions (**Figure 2.3.2**). The summary of the performances is provided in **Table 2.3.1.** The OFET device using as-cast PCDTBT films without

thermal annealing exhibits a hole mobility of 2.2×10^{-4} $cm^2/V \cdot s$ with an on/off current ratio (I_{on}/I_{off}) of 4.44×10^3. For PCDTBT thin films after annealing at evaluated temperatures the mobilities are not markedly improved, implying that the PCDTBT thin films remain nearly amorphous for both as-cast and annealing at high temperature.

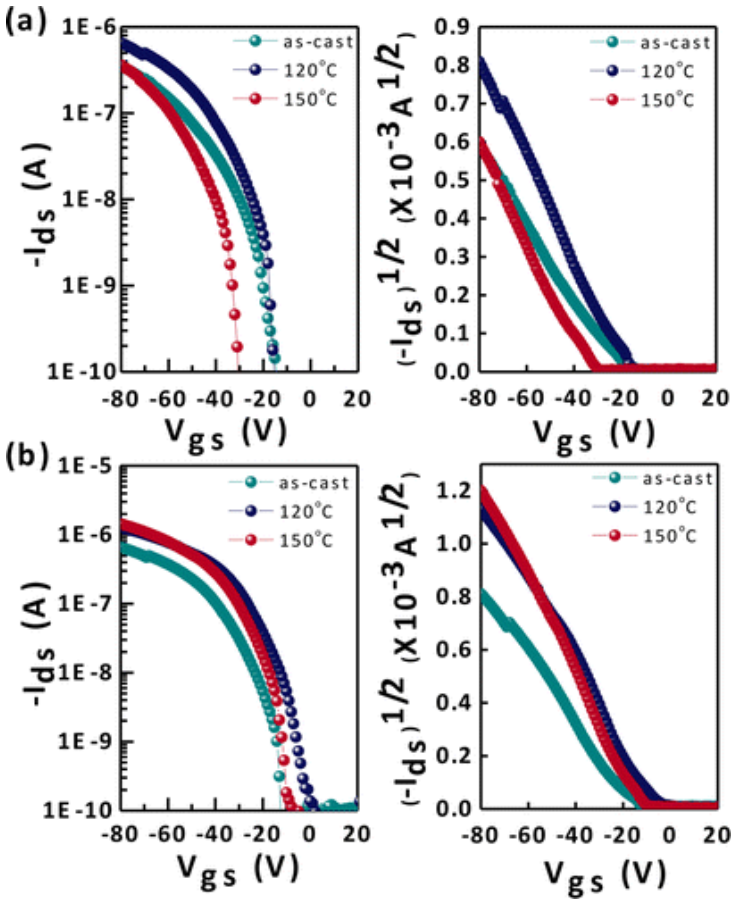

Figure 2. 3. 2. Transfer characteristics of (a) PCDTBT- and (b) PCDSeBT-based OFET devices at different annealing temperatures.

On the other hand, it is found that the unannealed thin films of PCDSeBT exhibit a slightly higher mobility of μh = 5.1 × 10−4 cm2 /V·s, compared with that of pristine PCDTBT. Interestingly, in contrast, as the PCDSeBT thin films are annealed at a temperature of 120 and 150 °C, the mobilities are systematically improved up to 1.0 × 10−3 cm2 /V·s (**Figure 2.3.2b**), which is about 1 order of magnitude higher than that of PCDTBT, possibly due to increased interpolymer chain contact induced by Se···Se interactions with the thermal annealing process.

Table 2. 3. 1. OFET performance of PCDTBT and PCDSeBT polymer thin films at different annealing temperatures

Polymer	Condition	Mobility (μ_h)(cm^2/V.s)	I_{on}/I_{off}	V_{th}[V]
PCDTBT	As-cast	2.2 X 10^{-4}	4.4 X 10^3	-21
	120℃	4.9 X 10^{-4}	7.9 X 10^3	-22
	150℃	3.5 X 10^{-4}	7.9 X 10^3	-34
PCDSeBT	As-cast	5.1 X 10^{-4}	4.1 X 10^4	-19
	120℃	7.8 X 10^{-4}	3.4 X 10^4	-9
	150℃	1.0 X 10^{-3}	4.0 X 10^4	-13

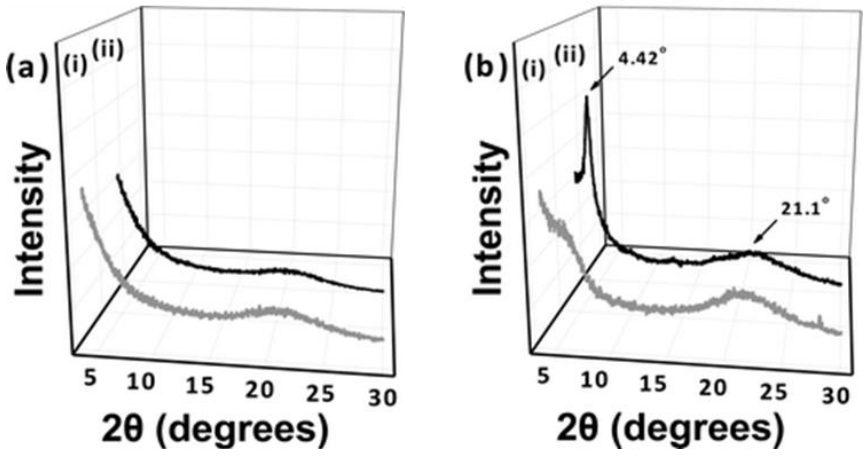

Figure 2. 3. 3. X-ray diffraction patterns of PCDTBT(a) and PCDSeBT(b) thin films before (i) and after annealed at 150 °C (ii).

To gain a better understanding of the influence of the thermal annealing, the crystallinity and molecular organization of PCDTBT and PCDSeBT thin films were investigated by X-ray diffraction (XRD), both before and after annealing at 150 °C. Both the as-cast and annealed PCDTBT thin films fail to reveal any defined scattering patterns (**Figure 2.3.3a**), indicating the macroscopically disordered, amorphous structure. In the case of PCDSeBT, the as-cast thin films show very weak diffractions

(**Figure 2.3.3b**). Upon thermal annealing, the primary peak at 4.42°, corresponding to a d-spacing of 19.99 Å, progressively intensifies and the secondary broad peak at ~21.1° (d = 4.21 Å) that is probably related to π−π stacking becomes visible (**Figure 2.3.3b**). On the basis of these XRD results, we can conclude that the oriented microstructure of the as-cast PCDSeBT thin films is kinetically limited but the polymer chains reorganize to ordered lamellar packing structures upon annealing. This observation is a plausible explanation for the sudden rise in mobility of PCDSeBT as a function of the thermal annealing.

Photovoltaic effects of PCDSeBT were investigated in BHJ PSCs with the device structures of the standard configuration glass/ITO/PEDOT:PSS/PCDSeBT:PC71BM/Al. The PCDSeBT:PC71BM weight ratio was optimized from 1:1, 1:2, 1:3, to 1:4. The current-density−voltage (J−V) characteristics of the devices under the illumination of simulated AM 1.5G conditions (100 mW/cm^2) are shown in **Figure 2.3.4a** and the parameters are summarized in **Table 2.3.2.** Without extensive optimization, the initial device fabricated from the blend solutions with a PCDSeBT:PC71BM weight ratio of 1:1 shows a PCE of 0.73% with a J_{SC} of 2.98 mA/cm^2 , a VOC of 0.71 V, a fill factor (FF) of 35%. As increasing the weight fraction of PC71BM, the PCEs are gradually increased. The device containing the 1:4 w/w blend as the photoactive layer after thermal annealing at 150 °C delivers at superior performance with the J_{SC} of 11.7 mA/cm2 , VOC of 0.79 V, and FF of 45%, improving the PCE to 4.12%, an approximately 37% enhancement in PCE, when compared to the reference cell based on PCDTBT:PC71BM for the sake of comparison (see **Figure 2.3.4c**).

Table 2. 3. 2. Photovoltaic properties of PSCs based in PCDSeBT.

PCDSeBT:PC$_{71}$BM	***J*$_{SC}$ [mA/㎠]**	**V$_{OC}$ [V]**	***FF* [%]**	**PCE [%]**
1:1	2.98	0.71	0.35	0.73
1:2	4.66	0.76	0.42	1.50
1:3	9.97	0.79	0.46	3.64
1:4	11.7	0.79	0.45	4.12
1:4 (before thermal annealing)	10.3	0.64	0.42	2.76

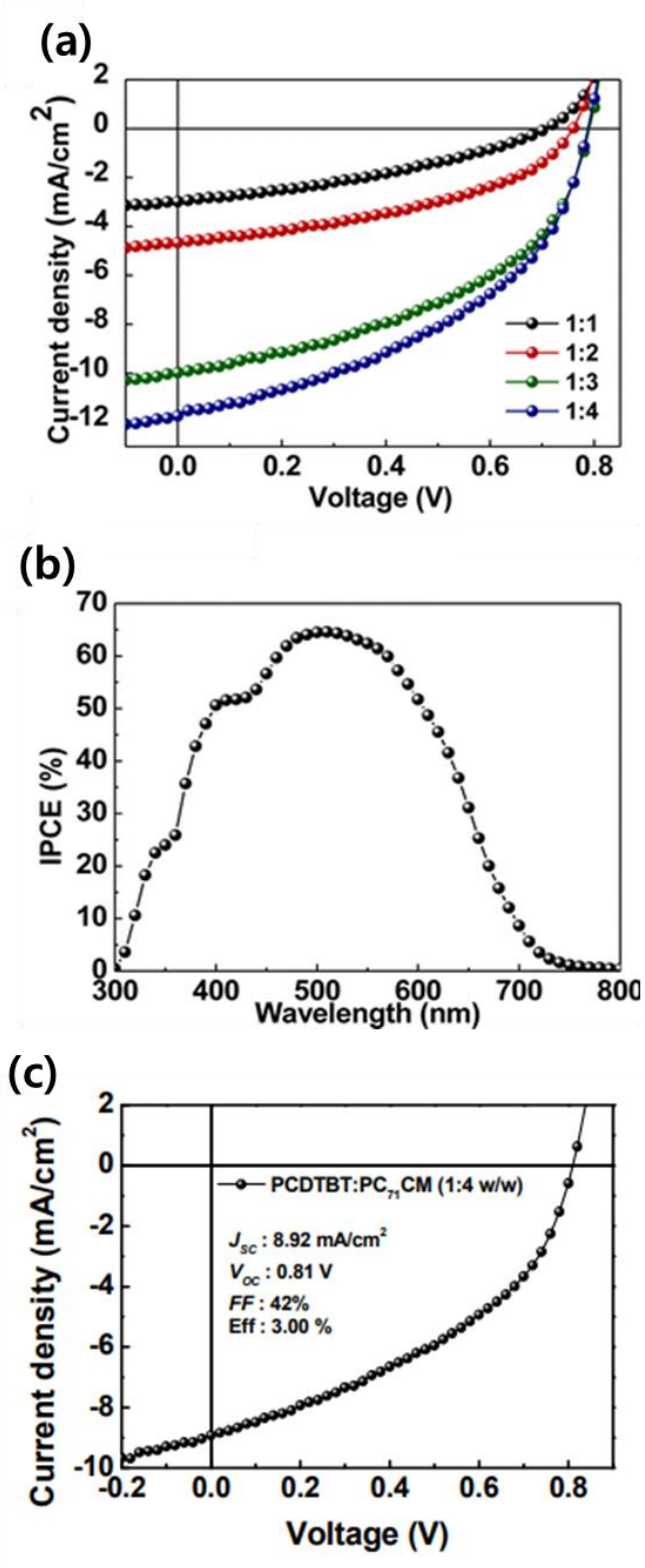

Figure 2. 3. 4. *J–V* characteristics of PSCs based on PCDSeBT:$PC_{71}BM$ under illumination of AM 1.5 G, 100 mW/cm^2 (a). Incident photon-to-current efficiency (IPCE) spectrum of PCDSeBT:$PC_{71}BM$ (1:4 w/w)-based device (b). Reference device with PCDTBT:PC71BM (c).

It is worth noting that the J_{SC}, to the best of our knowledge, is among the highest J_{SC}s reported to date for PCSs based on PCDTBT analogues,[152] in a good agreement with the extended absorption of sunlight through the low bandgap and broaden absorption band of PCDSeBT. In order to ensure the accuracy of the measurements, we investigated the incident photon-to-current efficiency (IPCE) spectrum of the optimized device (1:4 w/w), exhibiting over 65% at the energetically lower peak, i.e. at the λ_{max} of PCDSeBT (**Figure 2.3.4b**).

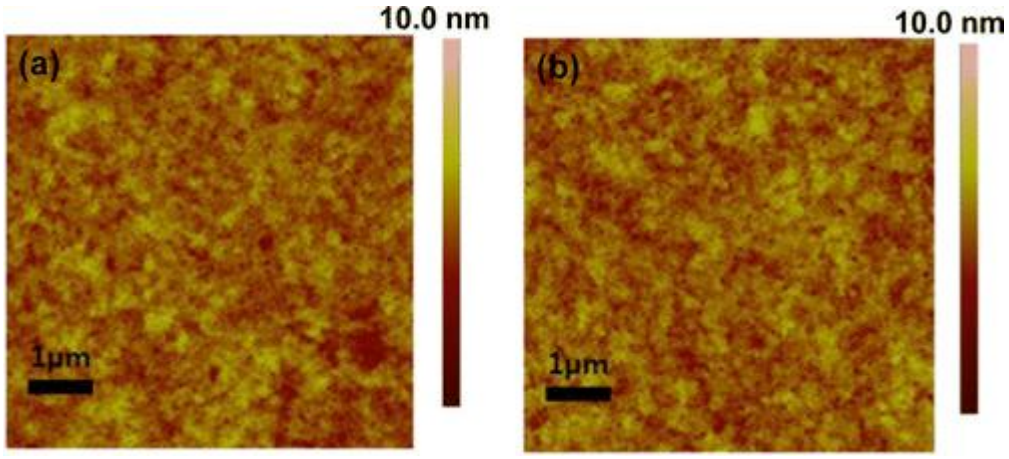

Figure 2. 3. 5. AFM images (6 μm × 6 μm) of PCDSeBT:PC_{71}BM (1:4 w/w) cells before (a) and after (b) thermal annealing at 150 °C, respectively.

The J_{SC} value calculated by integrating the IPCE data with an AM 1.5G reference spectrum is rather consistent with that obtained from J−V plots within 10% error. Atomic force microscopy (AFM) was performed to gain insight into the surface morphology of the optimized 1:4 w/w blend films (**Figure 2.3.5**). The films before and after thermal annealing have smooth surface topographies and very similar features, where the formation of voids, typically attributed to incompatibility between donor and acceptor components, is not observed. However, the rms roughness is somewhat reduced to from 0.47 to 0.43 nm with thermal treatment, being favorable for charge separation and transport. This can reasonably explain the enhanced efficiency via the post-annealing effect. Note that, in stark contrast to PCDTBT:PC71BM system in which thermal annealing reduced the photovoltaic parameters (FF, J_{SC}, and V_{OC}),[153] the performance of all PCDSeBT-based devices for this study is considerably improved as a result of thermal treatment. We can conclude that the formation of crystalline nanoscale domains would be slightly induced in PCDSeBT:PC71BM with a thermal treatment in consequence of the ordered crystalline nature of the PCDSeBT on annealing as supported by the XRD results above as well as the large quinoidal character in the polymer backbone as the inclusion of selenophene.[154] The AFM of the annealed film gives an evidence for slightly nanofibril-like organization (see **Figure 2.3.5b**).

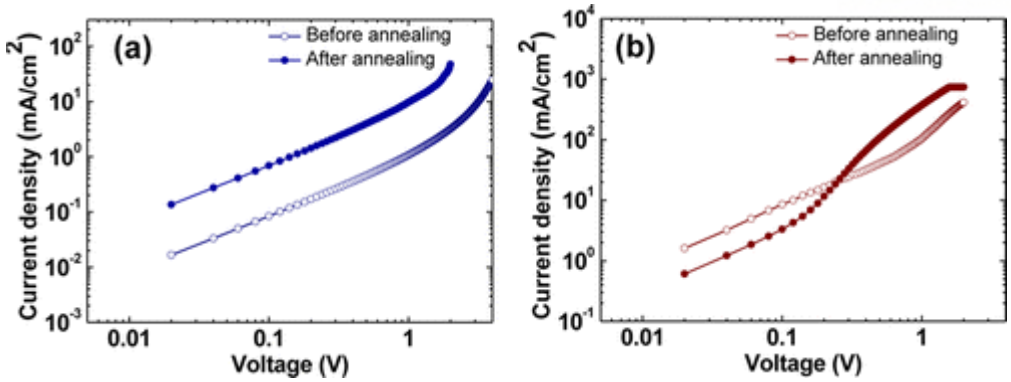

Figure 2. 3. 6. Measured *J–V* characteristics by the space charge limited current (SCLC) method with PCDSeBT:$PC_{71}BM$ (1:4 w/w) films under dark conditions before and after thermal annealing for hole-only device (a) and electron-only device (b).

The hole and electron mobilities of PCDSeBT:PC71BM (1:4 w/w) blends were measured using the space-charge-limited current (SCLC) method and the J−V characteristics were plotted in **Figure 2.3.6**. The hole mobility (μ hole = 4.68 × 10−5 cm2 /V·s) obtained with the thermally annealed film is one order higher than that without post annealing (μ hole = 4.02 × 10−6 cm2 /V·s), whereas in the both cases, the electron mobilities (μ electron) are similar (1.24 × 10−3 and 5.58 × 10−3 cm2 /V·s) for as-cast and annealed films, respectively, yielding a smaller difference between the mobility ratio for the annealed film. The higher mobilities and more balanced charge transport should definitely favor the charge transportation in the blend film and lead to high solar cell performance, supporting the beneficial effect of the thermal annealing on PCDSeBT:PC71BM cells.

2.3.4 Conclusion

In conclusion, diselenienylbenzothiadiazole (DSeBT) units have successfully been incorporated into a D−A polymer backbone by Suzuki polymerization with 2,7-carbazole comonomer, affording a poly(2,7-carbazole-alt-diselenienylbenzothiadiazole) (PCDSeBT); This design motif is that replacement of thiophenes to selenophene units in PCDTBT that acts as a superior p-type photoactive material for PSCs, induces a lower bandgap (1.70 eV) than that of PCDTBT (1.85 eV), while the ideal HOMO energy level (−5.40 eV) is still maintained. Another pleasant surprise comes from PCDSeBT with a relative wider absorption band observed, as a result of strong intermolecular Se···Se interactions. The lower bandgap with the broaden absorption band significantly improves a J_{SC} of 11.7 mA/cm2 , which is among the highest J_{SC} values for PSCs based on PCDTBT derivatives, while the low HOMO energy level maintains the high VOC value. The corresponding PCE is 4.12%, about 37% higher than that obtained from a PCDTBT-based reference device. This work provides a feasible strategy for selective fine-tuning of LUMO levels, which achieves a high J_{SC} value, while nearly remaining a high VOC. Therefore, further exploration of PCDSeBT-based PSCs is still warranted for high-performance PCEs by means of controlling the film morphology and improving electric contacts.

2.4. Finding Optically Advantageous Top Electrodes for Organic Solar Cells[250]

2.4.1 Research Backgrounds

Polymer solar cells (PSCs) based on thin film conjugated polymer/fullerene compounds have attracted attention due to their potential applications in light weight, low-cost, flexible, and large-area solution processed devices.[155-160] Recently, the power conversion efficiency of PSCs has reached 11 %, while 10 % has been estimated as the threshold efficiency for commercial applications.[161] For the commercialization of PSCs, stability and mass production techniques still require further development. Therefore, significant research efforts have recently focused on enhancement of PSC stability. Inverted polymer solar cells (iPSCs) offer distinct advantages for long term air stability compared to conventional polymer solar cells (cPSCs) by avoiding the corrosive and hygroscopic p-type buffer layer poly(3,4-ethylenedioxylenethiophene):poly (styrenesulphonicacid) (PEDOT:PSS) and easily oxidizable metal cathodes.[162, 163] Inverted devices differ from conventional devices by using an n-type transparent substrate and high work function top electrode; many studies have been attempted to identify optimal materials and processing conditions to construct this architecture. Early work with iPSCs, explored the use of various n-type, p-type metal oxides to achieve symmetry breaking in iPSCs, such as titanium oxide (TiO_x), zinc oxide (ZnO) or molybdenum oxide (MoO_3), vanadium oxide (V_2O_5) have been introduced between the active layer and the electrodes.[164-166] However, there are inherent incompatibilities at the organic active layer/inorganic metal oxide interface. Therefore, recently, conjugated polyelectrolyte (CPE) have been introduced at the interface between the organic active layer and inorganic metal oxide in order to improve compatibility at the organic/inorganic interface.[167-169] Although TiO_x or ZnO layers have been demonstrated as effective n-type buffer layers, they can reduce the amount of light absorption within the active layer due to absorb in the blue to ultraviolet (UV) wavelength region.[170] To reduce this absorption loss, more transparent organic materials such as Polyethylenimine ethoxylated (PEIE), branched polyethylenimine (PEI) and poly[(9,9-bis(3′-(N,N-dimethylamino) propyl)-2,7-fluorene)-alt-2,7- (9,9-dioctylfluorene)] (PFN) have been introduced in iPSCs as n-type buffer layers instead of ZnO or TiO_x[171-173]

In this article, we focus on the identification of optimal top electrode materials for use in iPSCs. We explore various anode metals including aluminum (Al), silver (Ag), gold (Au), copper (Cu), palladium (Pd), platinum (Pt), nickel (Ni), and molybdenum (Mo) to identify relationships between the inherent optical properties of the top electrode and device performance. The reflectance of three top electrodes (Al, Ag, and Au) was studied using ultraviolet- visible

(UV-Vis) spectroscopy in reflection mode, while electrode work functions were determined by ultraviolet photoelectron spectroscopy (UPS). Solar cell devices were fabricated in the inverted structure using a bulk heterojunction consisting of the conjugated polymer thieno[3,4-*b*] thiophene/ benzodithiophene (PTB7) and [6,6]-phenyl C_{71}-butyric acid methyl ester ($PC_{71}BM$) with different metal electrodes. The optical properties of these devices were simulated by transfer matrix modeling (TMM) and compared to the measured properties of the cells. Analysis of the simulations, experimental data and device stability lead to the unambiguous identification of Ag as the optimal anode for use in inverted devices, which is found to yield an efficiency of 8.19 % in PTB7-based iPSCs.

2.4.2 Experimental Details

Device Fabrication and characterization: Inverted organic solar cell devices were fabricated using the following procedure. First, ITO coated glass substrates were cleaned with detergent, then ultrasonicated in distilled water, acetone and isopropyl alcohol, then dried overnight in an oven at 100 ºC. The ZnO layer was next deposited by diluting a diethylzinc solution (Aldrich, 15 wt.% in toluene) with two parts tetrahydrofuran[174] (note: the un-diluted diethyl zinc solution is highly reactive towards air and should be handled inside a glove box; after dilution with THF, the solution becomes less reactive, however, appropriate safety precautions should be taken in case of an accidental spill or fire), filtering through a 0.45 μm PTFE syringe filter and spin coating at 3000 rpm for 30 s in air. The ZnO layer was then annealed in air on a hot plate at 110 °C for 10 minutes, a ZnO film thickness was approximately 60 nm. Subsequently, substrates were transferred into a nitrogen filled glove box for spin-coating the active layer. A mixed solution of PTB7: $PC_{71}BM$ in chlorobenzene (concentration of 10 mg mL^{-1}) with 3 % DIO additive was then spin coated at 1300 rpm for 60 s on top of the ZnO layer to obtain a BHJ film with thickness of approximately 80 nm. Samples were then brought under vacuum (10^{-6} - 10^{-7} Torr), and MoO_3 (Thickness : ≈ 3.7 nm, evaporation rate : 0.1 Å/s) and Al (Thickness : ≈ 100 nm, evaporation rate : 1.5 Å/s) or Ag (Thickness : ≈ 100 nm, evaporation rate : 1.5 Å/s) or Au (Thickness : ≈ 100 nm, evaporation rate : 0.2 Å/s) metal electrodes were deposited on top of the BHJ layer by thermal evaporation with an area of 0.13 cm^2 for each device. Inverted devices using P3HT:$PC_{61}BM$ in *o*-dichlorobenzene (*o*-DCB) were prepared following the same procedure with concentration of 26 mg mL^{-1} and thickness of approximately 200 nm.

Current density-voltage measurements were collected using a Keithley 2635 source measure unit. Each device was scanned from -0.5 V to 1.0 V in 20 mV steps with a 50 ms integration time for each data point. J-V characterization was carried out inside a nitrogen filled glove-box using a high quality optical fiber to guide the light from a xenon arc lamp to the solar cell device. Each device had an active area of 13 mm^2, defined by an aperture placed over each device. Solar cell devices were illuminated with an intensity of 100 mW cm^{-2} as calibrated using a standard silicon reference cell (PV Measurements, Inc.) which had been standardized and certified at the National Renewable Energy Laboratory in Golden, Colorado. EQE measurements were carried out using a QEX7 system manufactured by PV Measurements, Inc."EQE measurements were carried out using a QEX7 system manufactured by PV Measurements, Inc. UV-Vis reflectance spectra were measured on a Varian Cary 5000 spectrophotometer and UPS measurements were carried out using a KRATOS AXIS Nova instrument following previously reported procedures.[175] He I hv = 21.22 eV was used as a light source and thermally evaporated Au substrates were used as a reference. Work functions (Φ) were calculated from the onset of the secondary edge (E_{SE}) using the equation $\Phi = 21.22 - E_{SE}$.

Optical modelling by transfer matrix method: The transfer matrix method was utilized to calculate the absorption and $|E|^2$ intensity in each layer. The film thickness of each layer was determined by examining cross-sectional samples via scanning electron microscopy (cross-sectional SEM). Measured thicknesses were: 150 nm for ITO, 60 nm for ZnO, 80 nm for PTB7:$PC_{71}BM$ blend, 200 nm for P3HT:$PC_{61}BM$ blend, 3.7 nm for MoO3, and 100 nm for top metal electrode. Thickness measurements were repeated several times and average values were taken.

In order to conduct the transfer matrix method, the complex number of refractive indices ($\tilde{n} = n + ik$), which are the function of wavelength ($\tilde{n}(\lambda)$), are needed for each layer. To get the extinction coefficient, *k*, the absorption spectrum of each layer was measured by UV-vis absorption spectroscopy followed by conversion into *k* by following relationship.

$$\frac{A}{l}\ln 10 = \frac{4\pi k}{\lambda} \tag{2-1}$$

where A stands for measured absorbance at the specific wavelength, l for the thickness of the film, and λ for the wavelength. The films were coated on the quartz substrate and the thickness of the film was measured by alpha step.

Since real and imaginary parts of complex refractive index satisfy Kramers-Kronig relation (K-K relation), which ensures two parts are inter-convertible each other, refractive index of active layer was derived from the calculated extinction coefficient using Hilbert function implemented in MATLAB. In order to validate that this calculation is applicable to our consideration, calculated refractive index was compared with other published data[176, 177] (**Fig. 2.4.1**). The calculated optical constants exhibit extrema at the same position and follow previously reported spectra, confirming that the Kramers-Kronig transformation yields suitable refractive index data.

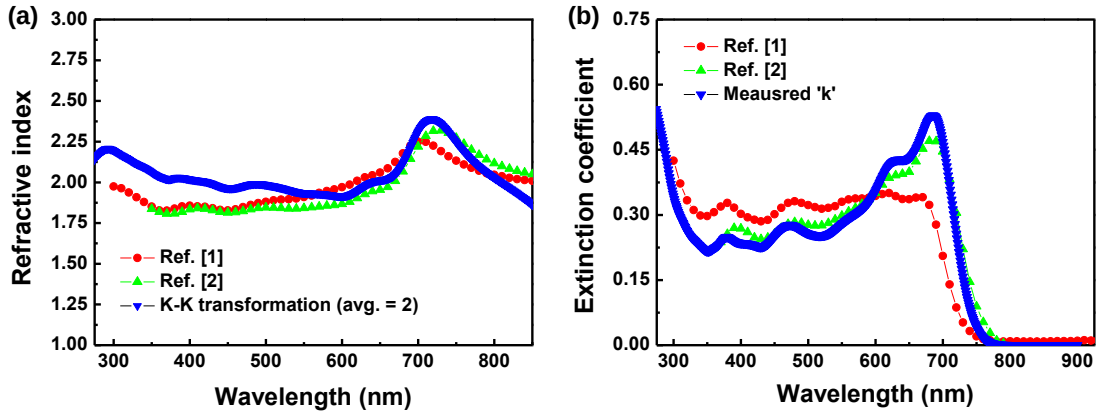

Figure 2. 4. 1. Complex refractive index of PTB7:$PC_{71}BM$ blends. (a) Refractive index (n). The calculated refractive index was compared with previously reported refractive index data which was obtained ellipsometrically. All papers share same donor:acceptor ratio. (b) Extinction coefficient (k). Extinction coefficients were calculated from the measured absorption coefficient (α) of the active film.

2.4.3 Results and Discussion

Optical properties and device characteristics

Solar cell devices function by absorbing light in the active layer after it has passed through a transparent front electrode. Active layers in polymer solar cells are typically close to 100 nm thick, with relatively low optical densities, and transmit a large fraction of this incident light. Light which is not absorbed in the first pass may be reflected from a top metal electrode and pass through active layer again, allowing additional absorption to take place. As a result, the optical properties of top metal electrode strongly correlate with light harvesting in the active layer. Generally, in iPSCs, one of three metals (Al or Ag or Au) is typically used as top electrode, with a high-work function layer of MoO_3 to facilitate the extraction of holes. To investigate the optical properties inherent to commonly used top electrodes, the reflectance of three metals (Al or Ag or Au) /MoO_3 films were measured. The MoO_3 film and metal film thickness were fixed at 3.7 nm and 100 nm, respectively. As shown in **Figure 2.4.2**a, three metal/MoO_3 films have considerably different reflectance spectra. The Au/MoO_3 film is much less reflective than Ag/MoO_3 or Al/MoO_3 at wavelengths below 600 nm wavelength, which corresponds to the Au overturn absorption peak.

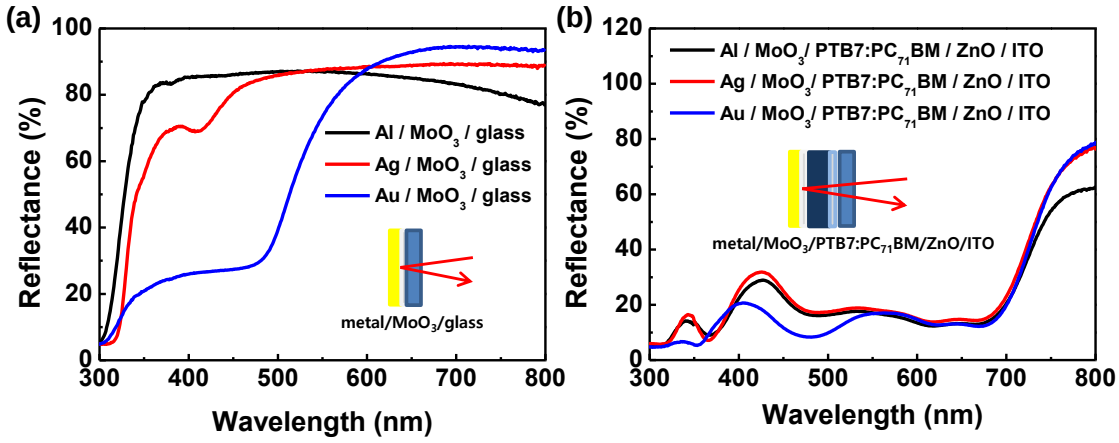

Figure 2. 4. 2. Comparison of reflectance of three types of metals (Al, Ag and Au) (a) deposited on glass/MoO_3 substrates films and (b) as completed solar cell devices (glass/ITO/PTB7:PC_{71}BM/MoO_3 /metal).

In contrast, the Ag/MoO_3 and Al/MoO_3 films have high reflectance throughout the visible spectrum, except wavelengths around 420 nm and over 600 nm, respectively. The reflectance curves of Ag/MoO_3 and Al/MoO_3 films are well matched with Ag and Al overturn absorption. Inverted structure devices were fabricated with three metal electrodes and compared the corresponding reflectance spectra. In completed solar cell devices, interference of incident light occurs within each layer, where incident light

interacts with light reflected from the top electrode (see **Figure 2.4.2**b). Here, the Au electrode device has lower reflectance than Ag or Al electrodes at less than 600 nm wavelength while the Al electrode device has lower reflectance than Ag and Au at wavelengths above 600 nm. This indicates that throughout all of the layers in the device, the intensity of reflected light is largely determined by the reflectivity of the top electrode.

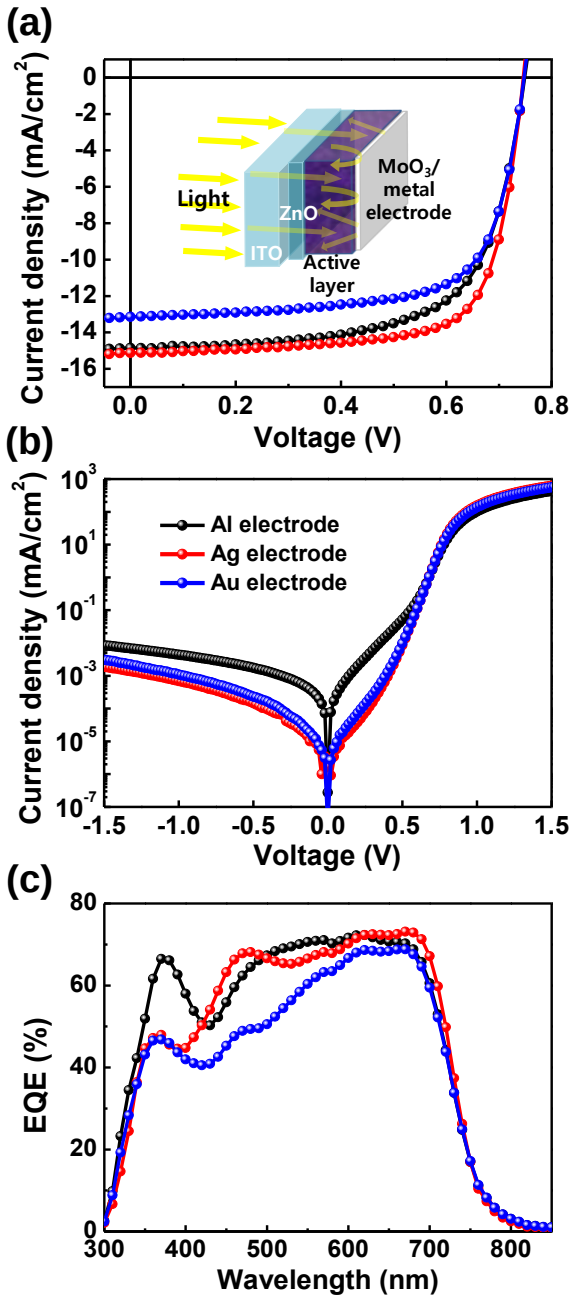

Figure 2. 4. 3. Comparison of (a) *J-V* characteristics in PTB7: $PC_{71}BM$ inverted devices with aluminum (Al), silver (Ag), and gold (Au) top electrodes under illumination and (b) in dark condition. (c) External quantum efficiency (EQE) spectra corresponding to the same devices.

Table 2. 4. 1. Photovoltaic parameters of PTB7:$PC_{71}BM$ inverted devices with different top electrodes.

Electrode	J_{SC} [mA/cm²]	V_{OC} [V]	*FF*	PCE [%]	J_{SC} (calc.) [b] [mA/cm²]	R_s [Ω cm²]	R_{sh} [Ω cm²]
Al [a] (*n* = 5)	14.6 ± 0.26 (14.9) [c]	0.75 ± 0.01 (0.75) [c]	0.65 ± 0.01 (0.66) [c]	7.14 ± 0.13 (7.35) [c]	15.1	6.00 ± 0.1	496 ± 7.9
Ag [a] (*n* = 5)	14.8 ± 0.39 (15.1) [c]	0.75 ± 0.00 (0.75) [c]	0.72 ± 0.01 (0.73) [c]	8.00 ± 0.22 (8.19) [c]	15.1	3.08 ± 0.1	753 ± 5.4
Au [a] (*n* =5)	12.9 ± 0.62 (13.5) [c]	0.75 ± 0.01 (0.75) [c]	0.69 ± 0.01 (0.70) [c]	6.58 ± 0.41 (6.93) [c]	13.4	4.92 ± 0.6	607 ± 3.3

[a] Device structure : ITO/ZnO/PTB7:$PC_{71}BM$/MoO_3(3.7 nm)/electrode(100 nm). Here *n* represents the number of devices for averaging the final values (see **Table 2.4.2**). [b] J_{SC}(calc.), calculated J_{SC} from a EQE curve. [c] Best performance

Table 2. 4. 2. Photovoltaic parameters of PTB7: $PC_{71}BM$ inverted devices with different top electrodes.

Electrode	J_{SC} [mA/cm²]	V_{OC} [V]	*FF*	PCE [%]	R_s [Ω cm²]	R_{sh} [Ω cm²]
Al-1	14.19	0.75	0.66	7.00	6.1	498
Al-2	14.85	0.75	0.66	7.35	6.1	508
Al-3	14.74	0.75	0.65	7.16	6.0	495
Al-4	14.69	0.74	0.65	7.12	5.9	489
Al-5	14.71	0.74	0.65	7.09	5.9	489
Al Average	14.64	0.75	0.65	7.14	6.00	496
Ag-1	14.69	0.75	0.71	7.73	3.1	745
Ag-2	14.96	0.75	0.71	7.95	3.3	750
Ag-3	15.12	0.75	0.73	8.19	3.0	759
Ag-4	15.04	0.75	0.72	8.10	3.0	756
Ag-5	14.17	0.75	0.72	7.70	3.0	753
Ag Average	14.78	0.75	0.72	8.00	3.08	753
Au-1	13.14	0.75	0.70	6.84	4.5	606
Au-2	11.94	0.74	0.68	6.02	4.2	603
Au-3	13.46	0.75	0.69	6.93	5.8	612
Au-4	12.59	0.75	0.67	6.28	5.2	606
Au-5	13.26	0.74	0.69	6.84	4.9	607
Au Average	12.88	0.75	0.69	6.58	4.92	607

Figure 2.4.3a present the device structure (glass /ITO (150 nm) /ZnO (60 nm) /PTB7:$PC_{71}BM$ (80 nm) /MoO_3 (3.7 nm) /top electrode (100 nm)) and the morphology of three kinds of top electrodes. The details of device fabrication are included in the experimental section. Each type of metal has different material properties (such as density, and melting point) and grows by different mechanisms under thermal evaporation condidtions.[178-180]

Additionally, the morphology of each type of metal may be affected by parameters such as evaporation rate or temperature. To investigate the effect of evaporation rate and morphology on device properties, 100 nm films of each type of electrode were prepared using different evaporation conditions; the morphology and conductivity of the anodes were characterized via scanning electron microscope (SEM) and Van der Pauw method, respectively, (See **Table 2.4.3** and **Figure 2.4.4**) for samples prepared using slow (0.2 Å/s) or fast (1.5 Å/s) evaporation rates. The Al electrodes show the strongest dependence on evaporation rate, exhibiting very large grain sizes (greater than 1 μm) when evaporated slowly and smoother, sub-micrometer features when evaporated quickly; the conductivity of Al electrodes was found to be $1.7 \times 10^5\ \Omega^{-1}cm^{-1}$ for slowly evaporated films and approximately doubled to $3.4 \times 10^5\ \Omega^{-1}cm^{-1}$ when evaporated quickly, reflecting the different morphologies. These differences presumably result from the reaction of Al vapor with trace gasses present in the evaporation chamber when evaporated slowly. Ag and Au morphologies showed weaker dependence on evaporation rete, yielding slightly smoother films when evaporated quickly. The conductivities of Ag electrodes were 3.7 and $3.9 \times 10^5\ \Omega^{-1}cm^{-1}$ for electrodes evaporated slowly or quickly, respectively, while the conductivities of Au electrodes were 3.1 and $3.0 \times 10^5\ \Omega^{-1}cm^{-1}$ for electrodes evaporated slowly or quickly, respectively. In any case, the conductivities were found to be about two orders of magnitude greater than the conductivity of the ITO electrodes ($5.2 \times 10^3\ \Omega^{-1}cm^{-1}$) indicating that the current through the electrodes is limited by the ITO films and not the top electrodes.

Table 2. 4. 3. Measured conductivity of metal thin films (100 nm) prepared using slow and fast evaporation rates.

Electrode	Conductivity [S/cm, $\Omega^{-1}cm^{-1}$]
ITO	5.2×10^3
Al (slow evaporation, 0.2 Å/s)	1.7×10^5
Al (fast evaporation, 1.5 Å/s)	3.5×10^5
Ag (slow evaporation, 0.2 Å/s)	3.7×10^5
Ag (fast evaporation, 1.5 Å/s)	3.9×10^5
Au (slow evaporation, 0.2 Å/s)	3.1×10^5
Au (fast evaporation, 1.5 Å/s)	3.0×10^5

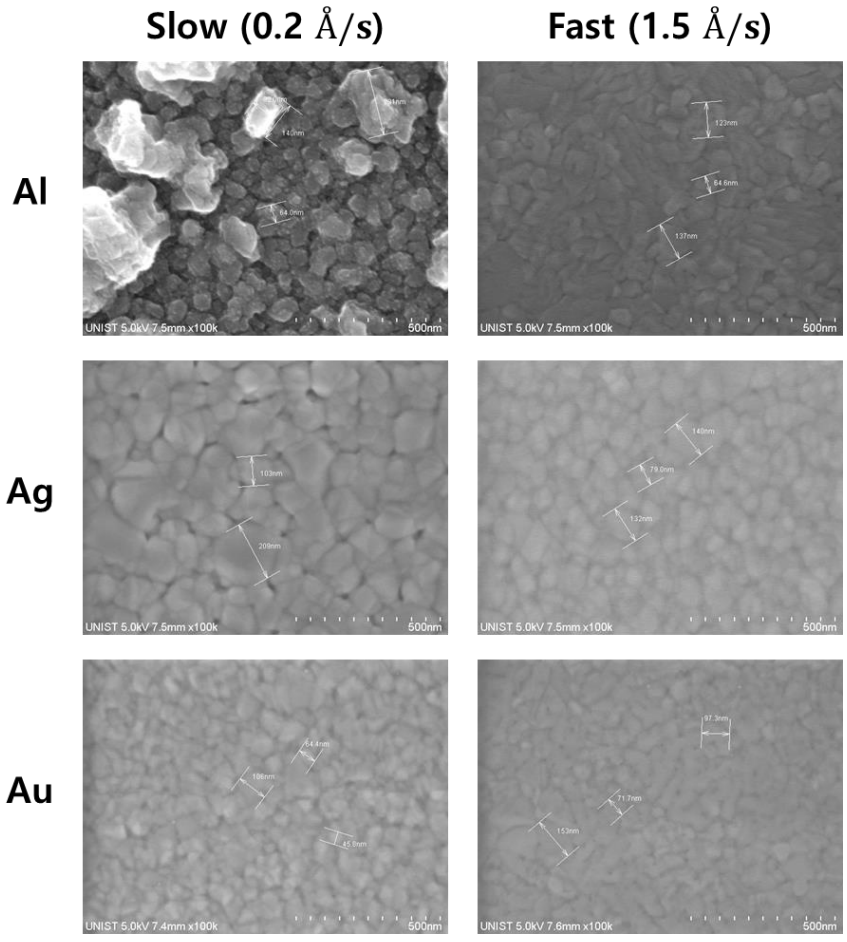

Figure 2. 4. 4. SEM images of different metal thin films (100 nm) prepared using slow and fast evaporation rates.

Figure 2.4.3a compares the current density - voltage (*J-V*) characteristics of iPSCs with three types of top electrodes under AM 1.5G illumination. The photovoltaic parameters are summarized in **Table 2.4.1**. These values are averaged values of each five devices. The power conversion efficiency (PCE) using Al electrodes is 7.14 ± 0.13 %, with a short-circuit current density (J_{SC}) of 14.6 ± 0.26 mA cm^{-2}, an open-circuit voltage (V_{OC}) of 0.75 ± 0.01 V and fill factor (*FF*) of 0.65 ± 0.01, while Ag electrodes yield a PCE of 8.00 ± 0.22 % (J_{SC} = 14.8 ± 0.39 mA cm^{-2}, V_{OC} = 0.75 ± 0.00 V and *FF* = 0.72 ± 0.01), and Au electrodes yield a PCE of 6.58 ± 0.41% (J_{SC} = 12.9 ± 0.62 mA cm^{-2}, V_{OC} = 0.75 ± 0.01 V and *FF* = 0.69 ± 0.01). Despite using metals with different work functions[181], the V_{OC} values are same (0.75 V) in all cases. When thin n-type and p-type buffer layers are introduced between the active layer and electrodes in the bulk heterojunction (BHJ) device, the V_{OC} may become more dependent on the energy level difference between the highest occupied molecular orbital (HOMO) level of the donor and the lowest unoccupied molecular orbital (LUMO) level of acceptor than the difference of work function between two electrodes.[182, 183] UPS was carried out to confirm the work function of the three anodes with a thin MoO_3 layer (3.7 nm). The spectra show significant differences at high intensity, indicating that the metal underneath the thin MoO_3 affects the spectrum, however, all three samples exhibit the same shoulder feature at the secondary edge, indicating that the thin MoO_3 results in the same work function (5.2 eV) regardless of whether it is deposited on Al, Ag or Au. (**Figure. 2.4.5**). Thus, even though only 3.7 nm of MoO_3 is used, it is effective at shifting the work function of all 3 electrodes to the same value and creating an Ohmic anode contact.

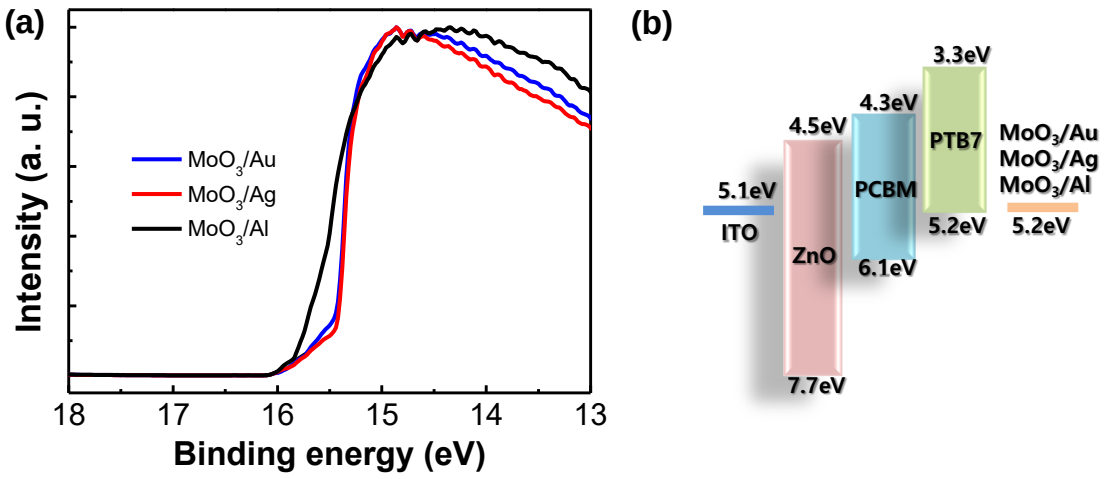

Figure 2. 4. 5. Energy band structures. a) UPS spectra for MoO_3/Au, MoO_3/Ag and MoO_3/Al. b) Energy band diagram for PTB7: $PC_{71}BM$ inverted devices.

Although the active layers, device structures and MoO_3 contacts were prepared using identical procedures, the *FF* exhibits considerable variation when the electrode metal is changed. The Ag electrode device reaches a peak *FF* of 72 % while the Au electrode shows a similar *FF* up to 69 %. The *FF* using the Al electrode, however, reaches only 65 %. Generally, the *FF* is related to shunt resistance and sheet resistance. Poor electrical contact leads to high series resistance and decrease *FF*.[184, 185] In case of Al electrodes, during the thermal evaporation of Al, chemical reactions may occur between MoO_3 and Al, leading to by-products such as MoO_2 and Al_2O_3 which lower the *FF*.[186] For this reason, Al electrodes results in the highest series resistance (R_s) (**Table 2.4.1**). The dark curves for Ag and Au electrode devices show a larger rectification (up to 6 orders of magnitude in the range of ±1.5 V) and smaller reverse saturation currents than the Al electrode device (**Figure 2.4.3**b). This result indicates that Ag and Au electrodes devices result in lower charge recombination losses than the Al electrodes. **Figure 2.4.3**c shows the external quantum efficiency (EQE) spectra of each device, which corresponds to their J_{SC}s. For each device, all processes (except for the top electrode material) were carried out under identical conditions; notably the blending condition and thickness (approximately 80 nm) are identical for each device. Nevertheless, the device with Au electrodes exhibits a lower J_{SC} (calc. J_{SC} = 13.4 mA cm^{-2}) compared to Ag (calc. J_{SC} = 15.1 mA cm^{-2}) and Al (calc. J_{SC} = 15.1 $mAcm^{-2}$, see **Table 2.4.1**). Moreover, we show the interesting result that Al and Ag electrodes devices produce the same J_{SC} despite having different EQE curves. Because the devices are otherwise identical, it follows that these differences in EQE arise from differences in the reflectance of Al and Ag.

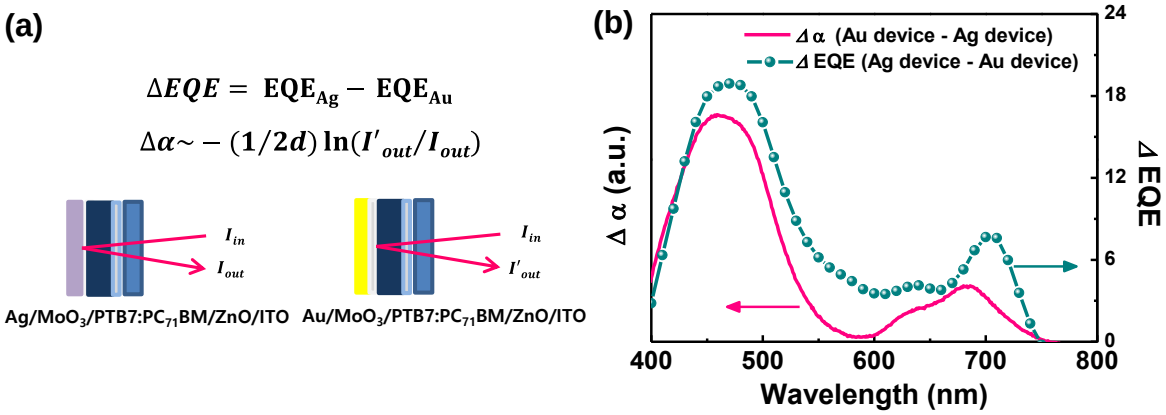

Figure 2. 4. 6. (a) Equations used to determine EQE difference (*Δ*EQE) and absorption difference (*Δ*α) here, d is the PTB7:PC_{71}BM film thickness (80 nm). I'_{out} is the intensity of the reflected light from the Au electrode device and I_{out} is the intensity of the reflected light from the Ag electrode device) as well as device schematics showing the optical beam path through the samples. (b) Comparison of *Δ*α between the Au electrode device and the Ag electrode device (left y-axis) with *Δ*EQE (EQE_{Ag} – EQE_{Au}) (right y-axis).

In order to thoroughly investigate the influence of optical properties on J_{SC}, we have compared the absorption difference ($\Delta\alpha$) between devices with Ag electrodes and Au electrodes, applying the equation in **Figure2.4.6**a to the reflectance spectra in **Figure. 2.4.2**b. $\Delta\alpha$ is compared to the difference in EQE using Ag and Au electrodes in **Figure 2.4.6**b. Notably, the change in absorbance closely matches the change in EQE, indicating that the reflectivity of the top electrode directly influences light harvesting in the active layer. This tendency was seen in not only PTB7:$PC_{71}BM$ inverted solar cells but also P3HT:$PC_{61}BM$ inverted solar cells (see **Figure 2.4.7** and **Table 2.4.4**).

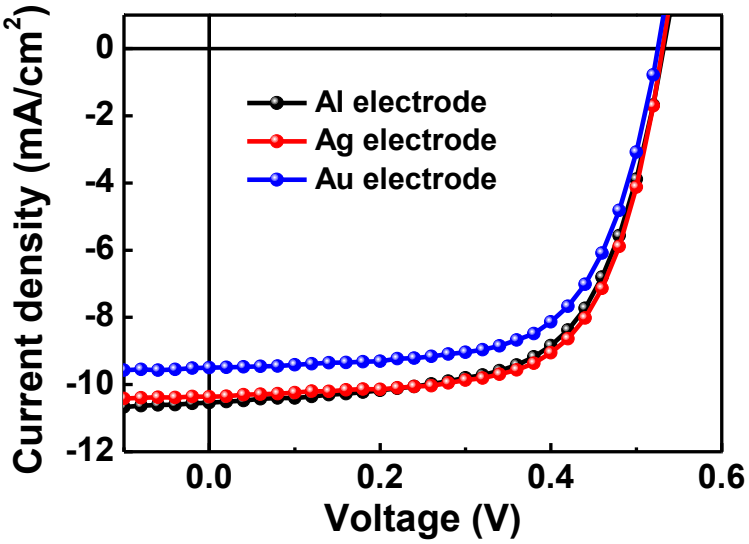

Figure 2. 4. 7. Comparison of *J-V* characteristics of P3HT: $PC_{61}BM$ inverted devices with different top electrodes.

Table 2. 4. 4. Photovoltaic parameters of P3HT: $PC_{61}BM$ inverted devices with different top electrodes.

Device structure	J_{SC} [mA/㎠]	V_{OC} [V]	*FF* [%]	PCE [%]
ITO/ZnO/P3HT:$PC_{61}BM$/MoO_3(3.7 nm)/Al(100 nm)	10.5	0.53	0.63	3.54
ITO/ZnO/P3HT:$PC_{61}BM$/MoO_3(3.7 nm)/Ag(100 nm)	10.4	0.53	0.66	3.63
ITO/ZnO/P3HT:$PC_{61}BM$/MoO_3(3.7 nm)/Au(100 nm)	9.50	0.53	0.65	3.25

.

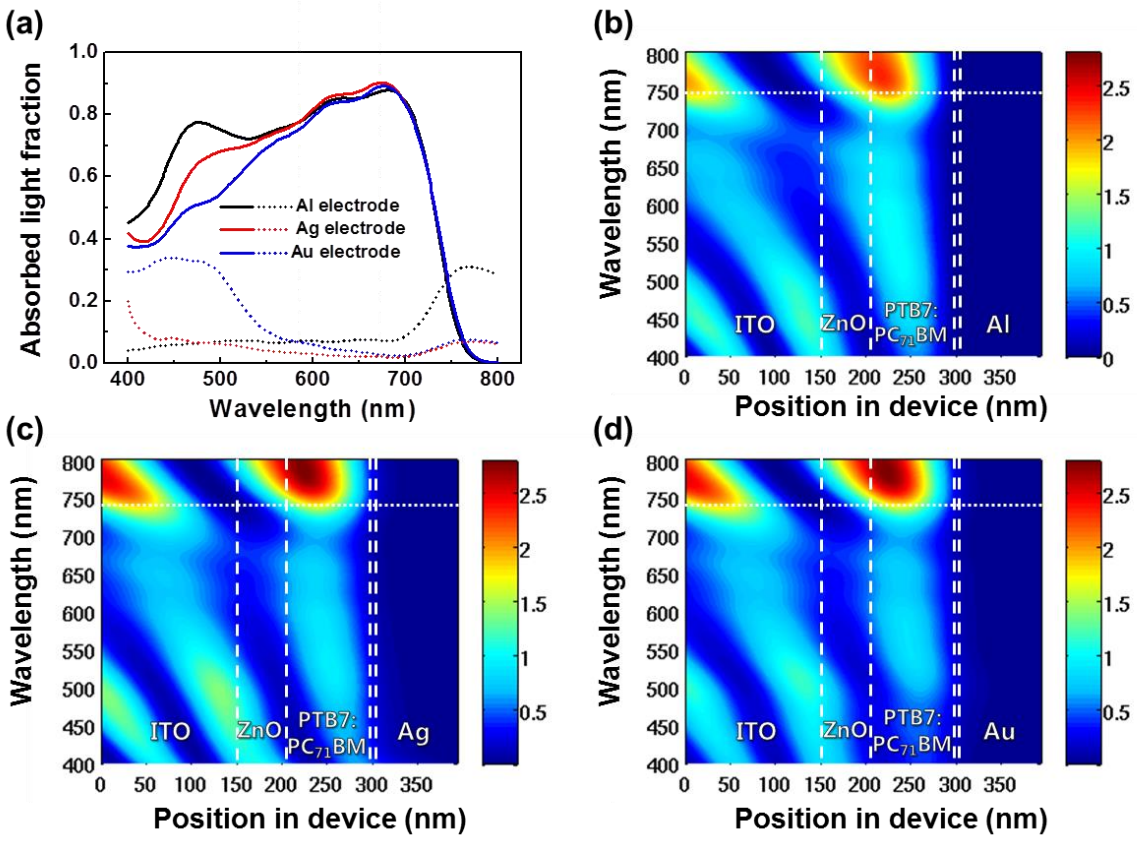

Figure 2. 4. 8. Simulated optical properties of PTB7:$PC_{71}BM$ inverted solar cells with different top electrodes. (a) Absorbed light fraction. Solid lines show the absorption in the active layer and while dotted traces show the parasitic absorption of the top electrode. (b) - (d) Normalized electric field intensity. (b), (c), and (d) correspond to devices having Al, Ag, and Au electrodes, respectively. White dashed lines indicate the boundaries of each layer and white dotted traces represent absorption onset of PTB7:$PC_{71}BM$.

In order to thoroughly explore how the optical properties of the top electrode influence photocurrent generation in iPSCs, a numerical simulation was carried out using, TMM.[187-189] Absorption not only by the active layer but also by the electrode was investigated via TMM. The distribution of the modulus squared of electric field intensity ($|E|^2$), which is directly proportional to the charge carrier generation in the active layer, was also considered. Simulated absorption by the active layer and the top electrodes are shown in **Figure 2.4.8**a. The device with Al electrodes shows the highest absorption in the active layer, while the Au electrode device displays significantly reduced absorption of light at wavelengths from 400 nm to 600 nm. This drop in active layer absorption coincides with a region of strong absorption by the Au electrode. The parasitic absorption of each electrode corresponds well with changes in the active layer absorption and explains the differences in the measured absorption spectra of the active

layer with each electrode. Although Al absorbs a considerable amount of the light above 600 nm, absorption by PTB7 blends drops off rapidly above 700 nm and little difference is observed between the absorption spectra above 600 nm. The tendencies of the light absorption in the active layer modeled by TMM are consistent with changes observed in the shape of EQE spectrum of each device in **Figure 2.4.3**c.

Figure 2.4.8(b-d) shows the distribution of the $|E|^2$ in each device with different electrodes. **Figure 2.4.8**b shows strong intensity in the visible region compared with **Figure 2.4.8**c and d, implying Al has superior reflectance within the visible range. Due to absorption in near IR region, $|E|^2$ is lower than the other metals at wavelengths of higher than 700 nm. Because the active layer absorbs little light at wavelengths greater than 700 nm, this parasitic absorption does not adversely affect photocurrent generation and it is apparent that Al is the best choice to maximize J_{SC} in terms of optical properties. In the case of Ag, a parasitic absorption of light at the wavelength below 470 nm results in reduced $|E|^2$ intensity compared to Al electrode device, as shown in **Figure 2.4.8**c. Nonetheless, due to the high reflectance of light at wavelengths greater than 470 nm, the simulated J_{SC} produced by the Ag electrode device is comparable to that of using Al. (16.8 mA cm^{-2} for the device with Al electrode and 16.2 mA cm^{-2} for that with Ag electrode). For active materials which absorb significant amounts of light at wavelengths greater than 700 nm, Ag electrodes may allow even higher J_{SC}s compared to Al electrodes. $|E|^2$ plots for Au electrodes are shown in **Figure 2.4.8**d and exhibit relatively weak intensity up to 700 nm. This is due to the significant parasitic absorption by Au at wavelengths below 600 nm. This result demonstrates why devices with Au electrodes exhibit the lowest simulated J_{SC} (15.3 mA cm^{-2}) among the devices. In order to ascertain if these results apply to systems other than the PTB7:PC_{71}BM system, the optical simulations and analysis were carried out for the P3HT:PC_{61}BM system as well. Similar tendencies were observed from the simulated optical properties of P3HT:PC_{61}BM inverted PSCs by TMM (**Fig. 2.4.9**). These data and simulations are consistent with the experimental results showing that Ag and Al top electrodes are advantageous for achieving optimal current density due to their high reflectance and low parasitic absorption compared to Au.

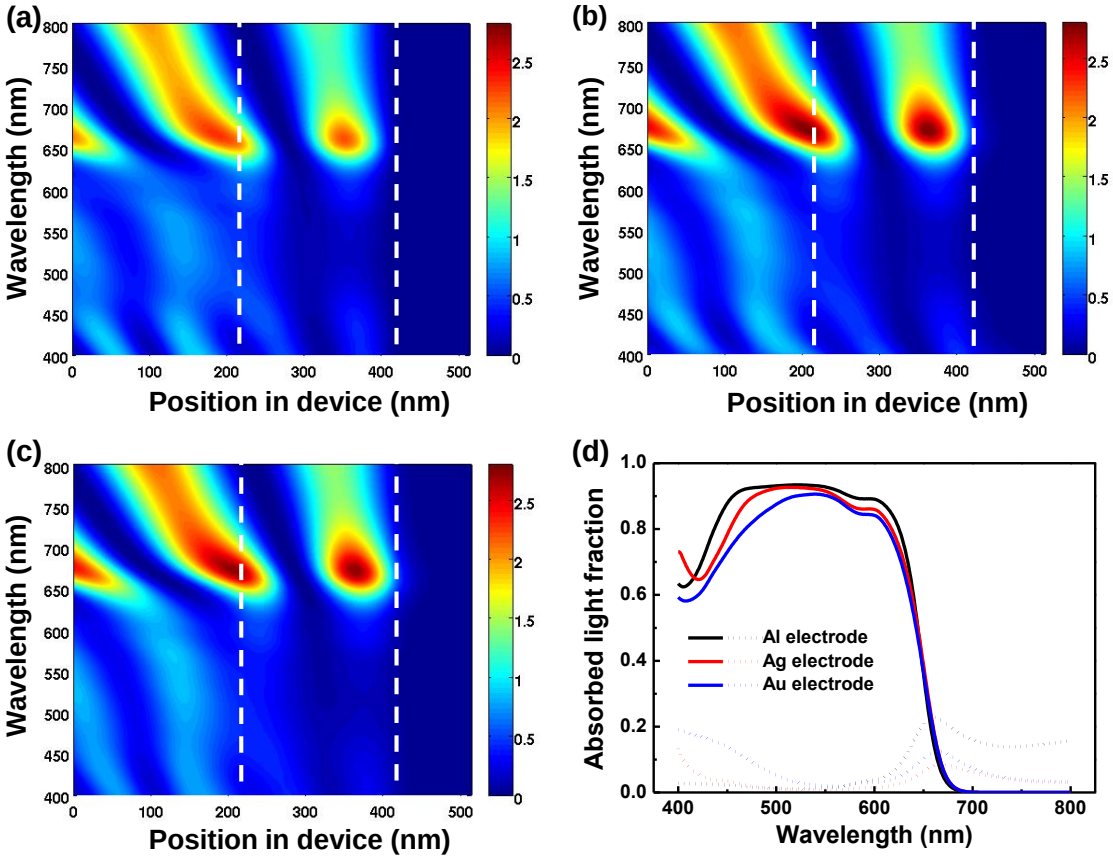

Figure 2. 4. 9. Simulated optical properties of P3HT:$PC_{61}BM$ inverted solar cells with different metal electrodes. (a)-(c) Normalized electric field intensity. (a), (b), and (c) are for devices having Al, Ag, and Au electrodes, respectively. White dashed lines indicate the position of the active layer. (d) Absorbed light fraction. Dashed lines indicate the absorption in the active layer. (Simulated J_{SC} : Al = 13.41, Ag = 13.05 and Au = 12.49)

Other metals

Although Al, Ag, and Au, are the most commonly used electrodes in inverted PSCs, it is possible to use other metals as top electrodes as well; we sought to carry out a comprehensive investigation of how a wider variety of metals affects the optical properties of OPV devices via TMM. Metals were selected which have appropriate work functions for use in the inverted structure and / or which have been applied as electrodes in other types of solar cells [190-192] including Copper (Cu), Palladium (Pd), Platinum (Pt), Nickel (Ni), and Molybdenum (Mo).

The J_{SC} of PTB7:$PC_{71}BM$ inverted solar cells was simulated using each type of anode. For the calculation of J_{SC}, the internal quantum efficiency (IQE) over all wavelengths was assumed to be 100 % implying that all photons absorbed in the active layer lead to photo-generated charge

carriers which are extracted without any losses. Simulated J_{SC}s for devices using each anode metal are compared in **Figure 2.4.10**. Al, Ag, and Au are included for comparison. In order to further quantify differences in each metal, we simulated the fraction of light absorbed by the metal electrode inside the device at three discrete wavelengths (400, 600, and 800 nm representing short, mid, and long wavelength regions of the visible spectrum, respectively). These results are summarized in **Table 2.4.5**. Spatial distribution of modulus squared electric field inside the device for each metal electrode was also considered in **Figure 2.4.11**.

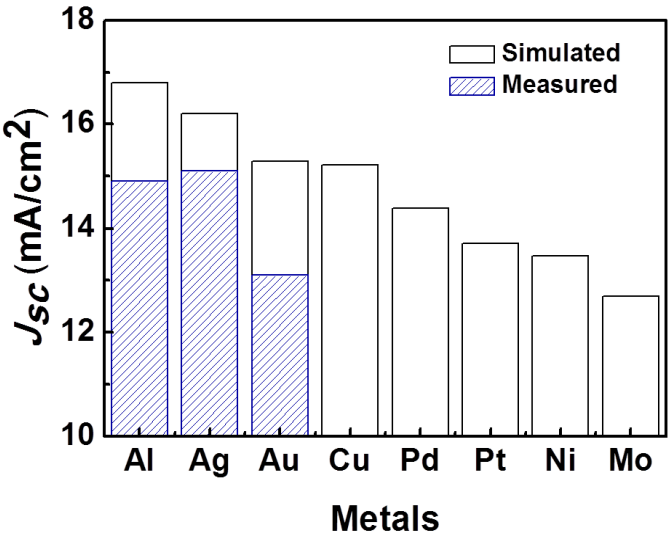

Figure 2. 4. 10. Simulated and measured *J*sc in the PTB7:$PC_{71}BM$ inverted solar cells with each top electrode. IQE of the devices is assumed to be 100 %.

Table 2. 4. 1. Simulated J_{SC} of PTB7:PC71BM inverted solar cells with each top electrode and simulated absorbance of each metal electrode in the devices at wavelength of 400, 600, and 800 nm.

Metal (Φ, eV)	**Simulated J_{SC} (mA/cm^2)**	**Absorption fraction of each metal (%)**		
		400 nm (Short λ)	**600 nm (Middle λ)**	**800 nm (Long λ)**
Al (4.3 eV)	16.8	4.08	7.1	28.7
Ag (4.7 eV)	16.2	19.9	2.9	6.2
Au (5.1 eV)	15.29	29.4	5.9	6.6
Cu (4.7 eV)	15.22	22.9	9.3	9.2
Pd (5.1 eV)	14.39	18.5	20.4	48.5
Pt (5.7 eV)	13.71	22.4	24.8	57.7
Ni (5.2 eV)	13.47	25.4	25	61.5
Mo (4.6 eV)	12.69	24.7	32.6	76.6

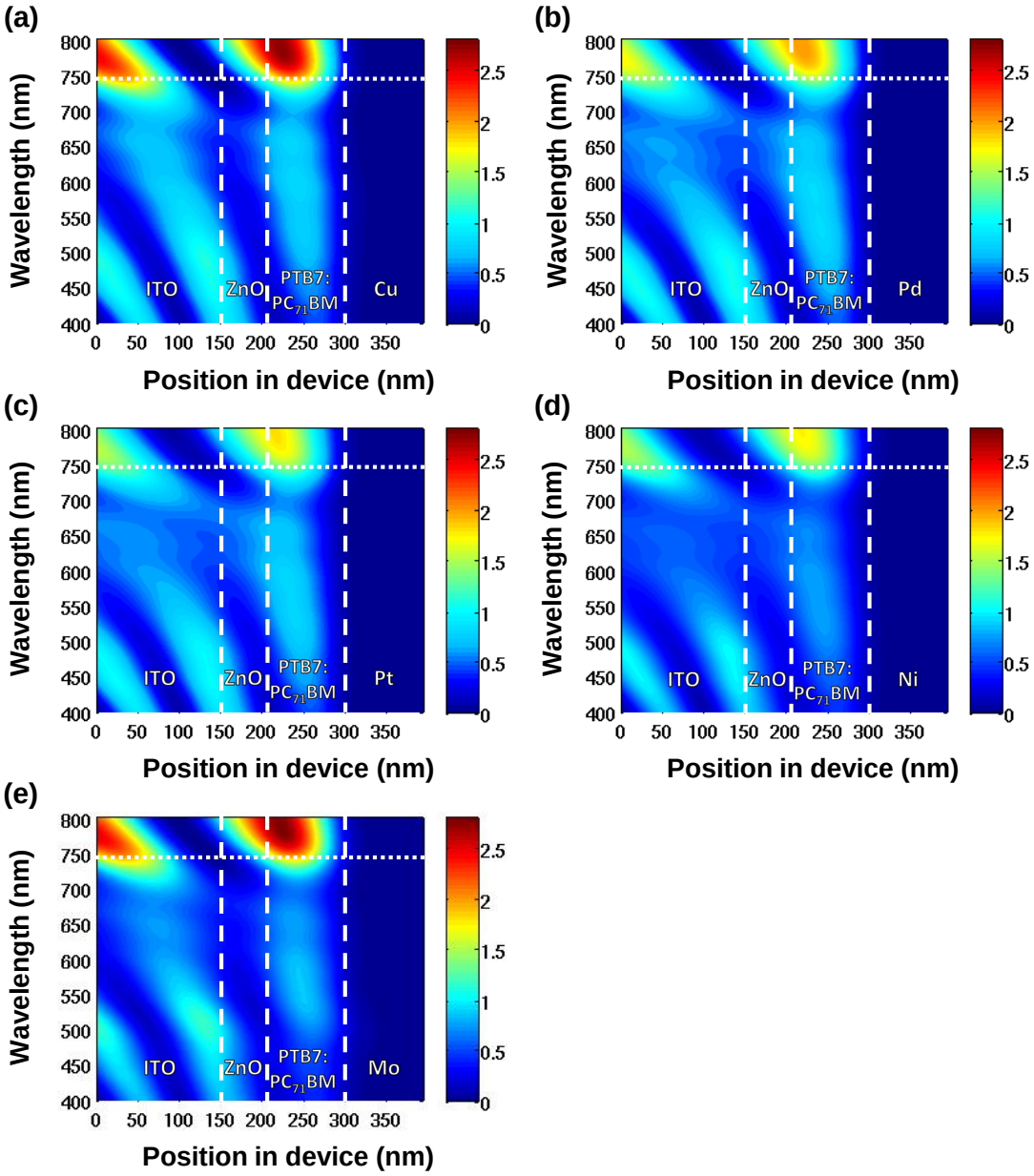

Figure 2. 4. 11. Spatial distribution of normalized electric field intensity in devices with different electrodes. (a), (b), (c), (d), and (e) correspond to devices with Cu, Pd, Pt, Ni, and Mo electrodes, respectively. White dashed lines indicate the boundaries of each layer and white dotted lines demark the absorption onset of PTB7:$PC_{71}BM$.

It is noteworthy that the Cu anode exhibits comparable J_{SC} to that of the device with the Au anode. Other metals, however, showed much lower J_{SC}. The Cu electrode absorbed 22.9 % of the incident light at 400 nm, and 9.3 % and 9.2 % at 600 and 800 nm respectively. The absorption was smaller at 400 nm and higher at 600 and 800 nm than those of Au (29.4 %, 5.9 %, and 6.6 %

at 400, 600 and 800 nm, respectively.). Strong absorption at short wavelengths for both Cu and Au causes devices with these metal electrodes to generate relatively low J_{SC}s compared to Al and Ag.

Pd, Pt, Ni, and Mo electrodes all exhibited significant absorption across the visible spectrum and much higher absorption at 800 nm. Simulated J_{SC}s for devices with Pd, Pt, Ni, and Mo electrodes were consistent with simulated absorption of each metal in the device. Although Mo is the most commonly used anode in thin film solar cells such as Cu (In,Ga)Se_2 cells, this metal absorbs the largest amount of light and is expected to result in a 25% reduction in current relative to Al when used in inverted polymer solar cells.

From these results, it is apparent that the optical properties of metal electrodes play a critical role in determining device properties of inverted PSCs. Unlike their thicker, inorganic counterparts, polymer solar cells cannot fully absorb the incident, non-reflected light in one pass, due to the thin active layers used in PSCs.[193] Therefore, the reflectivity of the metal electrode is a crucial contributor to the generation of current in PSC devices and it is clear that Al and Ag are the best choices for high reflectivity.

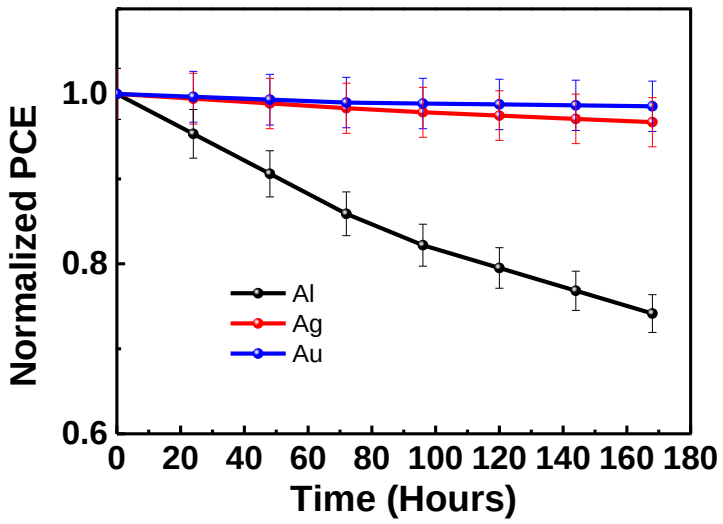

Figure 2. 4. 12. Normalized PCEs for PTB7:PC_{71}BM inverted solar cells with different top electrodes as a function of storage time in air under ambient conditions without encapsulation.

Despite the clear advantages offered by the optical properties of Al and Ag electrodes, Au electrodes have been more generally used in iPSCs. This may be because Au possesses excellent air stability due to its high work function. Therefore, we sought to compare the air stability of Al and Ag electrodes with Au. **Figure 2.4.12** shows the air stability of iPSCs in PTB7:PC_{71}BM with three types of electrodes. Solar cells were exposed to air at room temperature without any encapsulation over a period of about 170 hours. After 170 hours, Au electrode devices maintained almost their original efficiency as expected.

The Ag electrode devices performed similarly, retaining over 96 % of their original efficiency. The devices with Al electrodes, however, were significantly degraded to approximately 25 % of their original performance. These results show that the poor air stability of Al electrodes may limit the practical utility of this electrode even though this it offers good reflectivity and high J_{SC}.

2.4.4 Conclusion

In summary, we have elucidated relationships between the optical properties of top electrodes and the performance of inverted architecture solar cells using a suite of different metals. The reflectivity of each metal electrode is found to considerably influence the light harvesting within the active layer. The three metals Al, Ag and Au are found to offer the best optical properties and yield the highest J_{SC}s via optimal utilization of reflected light. Among these three electrodes, Au suffers from the greatest parasitic absorption and the exhibits the lowest reflectance in the visible region, leading to significantly lower J_{SC}s compared to the other electrodes. Al and Ag electrodes, however, have relatively good reflectance across the visible spectrum and produce larger J_{SC}s. Al electrodes were found to lead to unstable devices with low *FF*s due to the low work function and reactivity of Al. These data, coupled with the advantage that Ag electrodes can be processed by solution methods such as printing or coating[194] lead to the conclusion that the optimal top electrode for use in iPSCs is Ag, offering high performance, good air stability and convenient processability. This study provides guidelines and rational for the selection of appropriate top electrodes in future PSC devices.

III. Design of Semitransparent Electrodes by Fabry-Pérot Etalon Structure

3.1 Research Backgrounds

Recent interest in integrating semitransparent photovoltaic devices into the windows of buildings and other architectural structures has increased. Among the many promising types of photovoltaics, organic solar cells (OSCs) show particularly high potential because of specific advantages such as their flexibility and light weight, as well as the inherent semitransparency of organic photoactive materials. [195-203] For these reasons, semitransparent OSCs (STOSCs) are feasible for integration into structures such as rooftops, building exteriors, vehicle windows, and portable mobile power sources and have the potential for generating products that are both visually aesthetic and functional as renewable energy sources. [204-214] Notably, colorful STOSCs may be suitable for improving the aesthetics of structures in addition to being viable energy sources.

For colored STOSCs, the colors of devices are usually determined by tuning the absorption spectra of the photoactive components. The photoactive layers mainly consist of two components of electron donor and acceptor materials, where the color of devices is controlled by tuning the absorption range of both photoactive materials. [215, 216] These types of devices are usually fabricated using thin single-layer semitransparent metallic electrodes. However, STOSCs that rely only on the active layer to produce color can rarely achieve vivid coloration due to the broad absorption spectra of the active layers.[217] In addition, the thin metal electrodes used for high transparency have lower reflectance, which reduces the amount of re-absorbed light in the photoactive layer via refection at the electrodes.[218, 219] This type of design results in lower photocurrent density and low photovoltaic performance as compared to opaque devices.[220, 221]

Another approach to achieve colorful STOSCs involves optical engineering of electrodes to achieve high color-fidelity STOSCs. In this approach, a high reflectance composite electrode is achieved by constructing a dielectric cavity between two metal films, which exploits the interference effects in selectively transmitting specific frequencies of light while efficiently reflecting other wavelengths. [222-225] These types of colorful semitransparent electrodes have been reported using fabrication techniques such as sputtering or E-beam evaporation to deposit the cavity layer.[226, 227] Although effective, these processes for constructing metal-dielectric-metal (MDM) electrodes were proved not only to be time-consuming, but they can also damage actives layers with increasing device resistance.

In this study, we demonstrate a highly efficient strategy to produce colorful STOSCs based on MDM electrodes using a thermally evaporated antimony oxide (Sb_2O_3) as a dielectric cavity material. This type of electrode can be easily deposited by thermal evaoration to yield smooth films with exceptionally

low parasitic absorption. These types of Sb_2O_3-based MDM electrodes enable low sheet resistance and high transmittance values at specific wavelengths, leading to colored devices that perform well and with minimal photocurrent losses.

3.2 Experimental Details

Optimizing MDM electrodes: MDM electrodes were prepared by thermal evaporation and are composed of Sb_2O_3 (2 nm), Ag (25 nm), Sb_2O_3 (varying from 35 to 100 nm), and Ag (25 nm) onto a bare glass substrate at pressures below 10^{-6} Torr. Deposition rates for the Sb_2O_3 and Ag layers were 1.2–1.6 Å/s and 1.4–2.0 Å/s, respectively.

A Varian Cary 5000 spectrophotometer was used to determine the transmittance of MDM electrodes and devices.

3.3 Results and Discussion

Design and Fabrication of MDM electrodes

Fabry-Pérot etalon (FPE) structures consist of two parallel reflecting metal films and a dielectric cavity film between them. [229, 230] **Figure. 3.1a** presents two approaches used to tune the transmitted spectra of FPE structures by varying either the thickness (*t*) or the refractive index (*n*) of the dielectric layer. This electrode configuration can produce clear color and high transmittance with good wavelength selectivity by simply adjusting thickness or choosing cavity materials of different refractive indices. We prepared FPE films by sequentially depositing Ag/Sb_2O_3/Ag films. Sb_2O_3 has a high refractive index and low extinction throughout the visible spectrum, as shown in **Figure. 3.1b** The low extinction coefficient leads to minimal parasitic absorption in MDM electrodes, whereas the high refractive index enhances light transmission through the metal/dielectric interfaces. In addition, in contrast to most other dielectric oxides, which are refractory in nature, Sb_2O_3 can be easily deposited by thermal evaporation. Because thermal evaporation is ubiquitously used to deposit electrodes in OSCs, this MDM system can be easily implemented using standard OSC facilities.

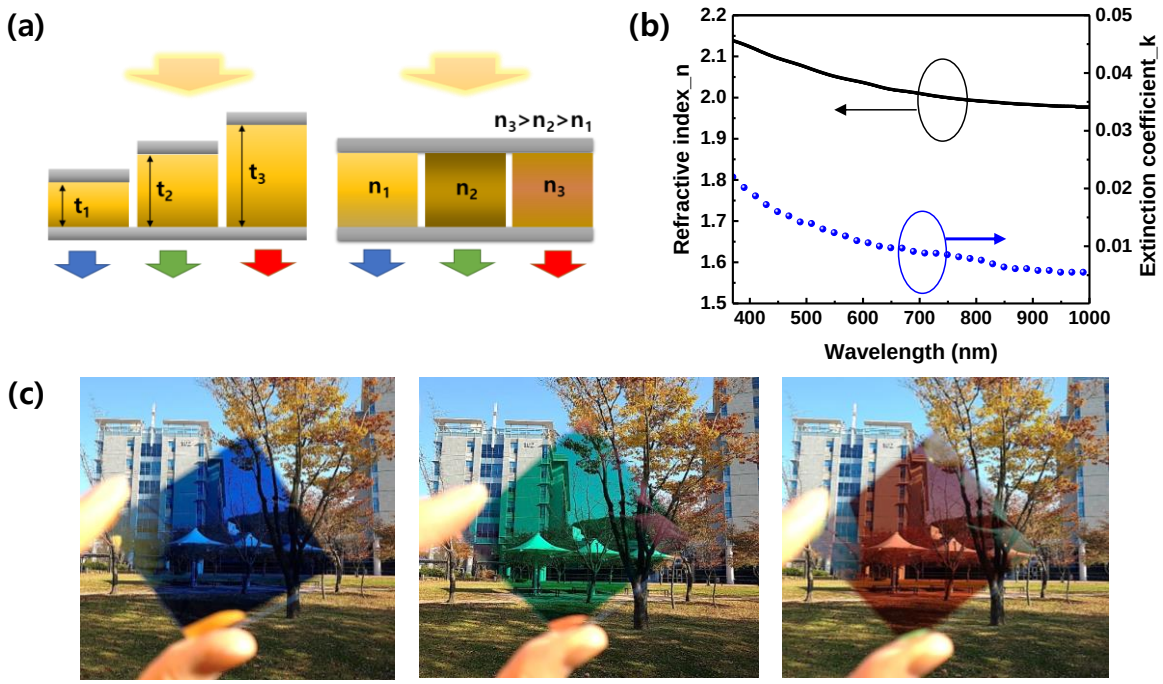

Figure 3. 1. (a) Schematic of two methods to tune the wavelength of light transmitted by an FPE structure with MDM structures. (b) Refractive index and extinction coefficient of the Sb_2O_3 cavity used in this study. (c) Photographs of fabricated blue, green, and red MDM electrodes (5 x 5 cm^2).

Furthermore, we compared transmittance of Ag/MoO_3/Ag and Ag/Sb_2O_3/Ag with varying thickness of intermediate metal oxide, MoO_3 and Sb_2O_3 layers. As shown in **Fig. 3.2**, Ag/Sb_2O_3/Ag electrodes

exhibited much higher transmittance compared to Ag/MoO_3/Ag electrodes, indicating the Sb_2O_3 based MDM electrodes can efficiently reduce parasitic absorption, leading to minimizing optical losses.

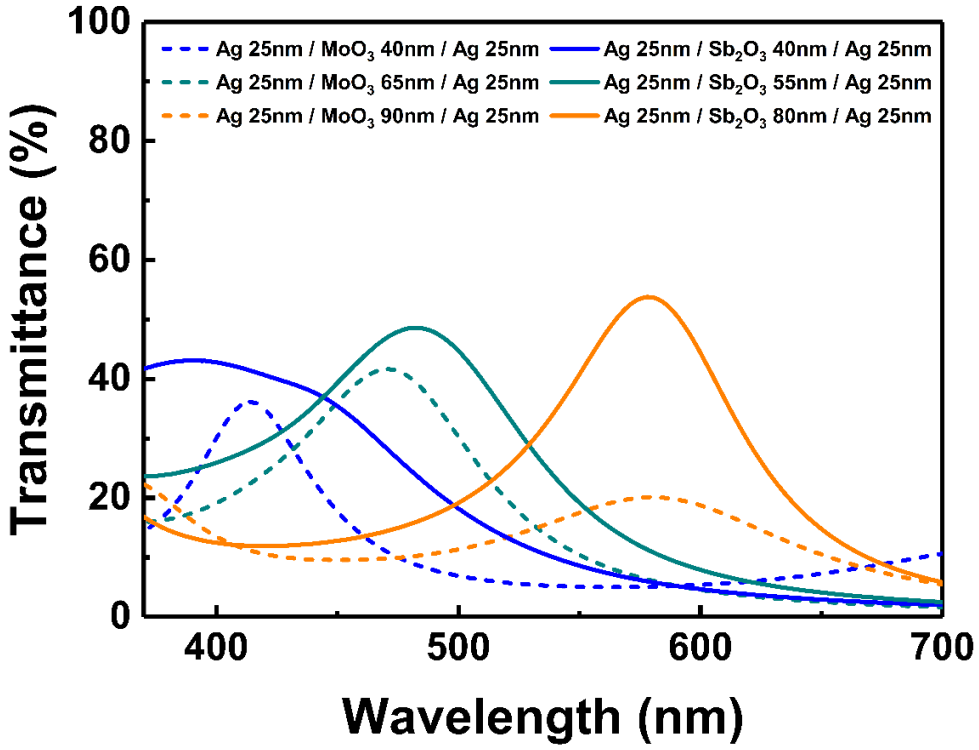

Figure 3. 2. Transmittance spectra of Ag/MoO_3/Ag and Ag/Sb_2O_3/Ag electrodes.

Thin Ag films are known to form islands and clusters. However, to achieve transparent electrodes and high-quality etalon structures, Ag thin films must have flat smooth surfaces and must be continuous to yield high electrical conductivity and avoid spurious localized surface plasmon resonance effects, which may arise from isolated Ag clusters. First, to produce high-quality Ag thin films with thicknesses of less than 30 nm, Ag was deposited onto 1-nm Au or 2-nm Sb_2O_3 seed layers. In previous studies, Au has been shown to serve as a seed layer for the deposition of high-quality thin Ag films. [231, 232] In this study, we discovered that Sb_2O_3 itself functions as an effective seed layer, thus simplifying the deposition procedure. **Figure. 3.3** shows that thermally evaporated Ag thin films with thicknesses < 25 nm (without seed layers) were found to be rough and covered with pinholes and cracks in films evaporated on bare glass. However, with Au or Sb_2O_3 seed layers, Ag thin films formed fully continuous networks without pinholes, even in the case of thin ~20-nm films. In particular, 2 nm thick Sb_2O_3 films enabled flat and pinhole-free Ag thin films to be obtained down to 15-nm of film thickness. The high quality of Ag thin films deposited on Sb_2O_3 seed layers resulted in superior transmittance as compared to Ag thin films prepared using other conditions, as shown in **Figure. 3.4**.

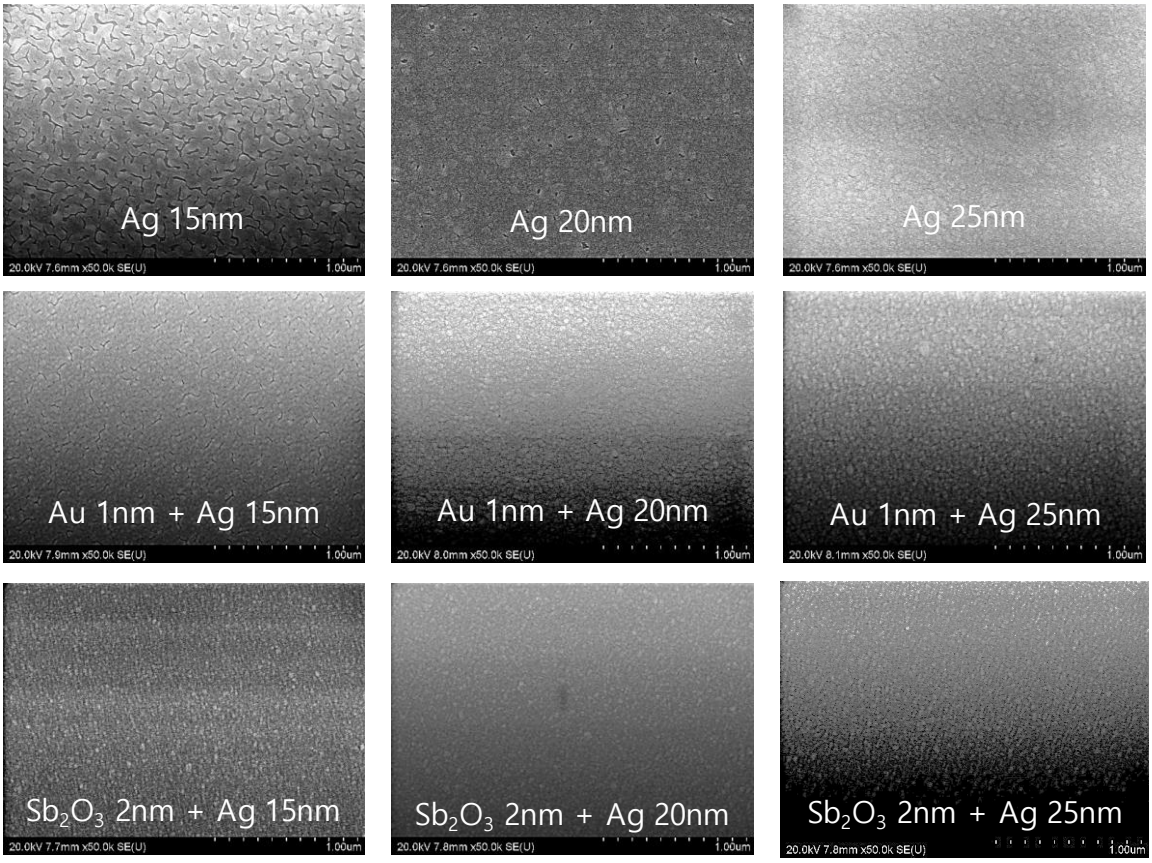

Figure 3. 3. SEM images comparing Ag thin films (15, 20, 25 nm) with and without Au or Sb_2O_3 seed layers.

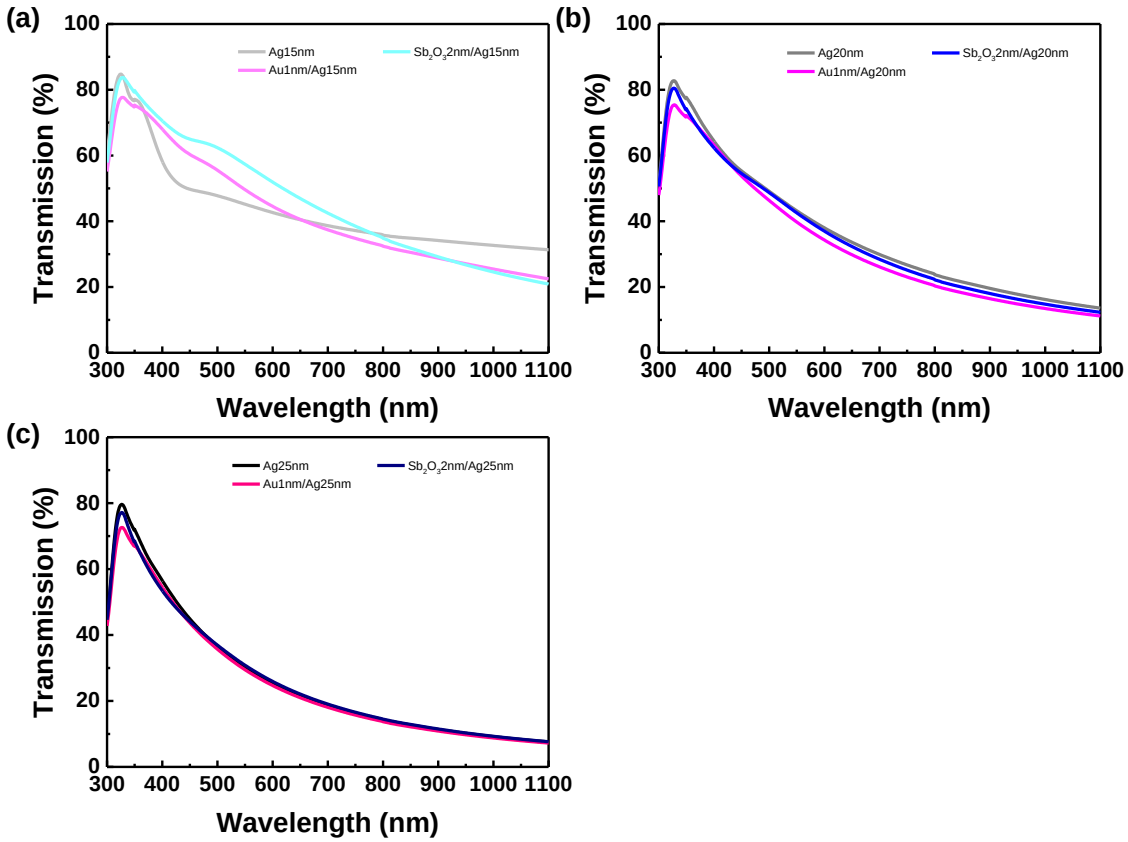

Figure 3. 4. (a–c) Comparison of transmittance spectra of Ag thin films with or without Au or Sb_2O_3 seed layers for Ag film thicknesses of 15, 20, and 25 nm, respectively.

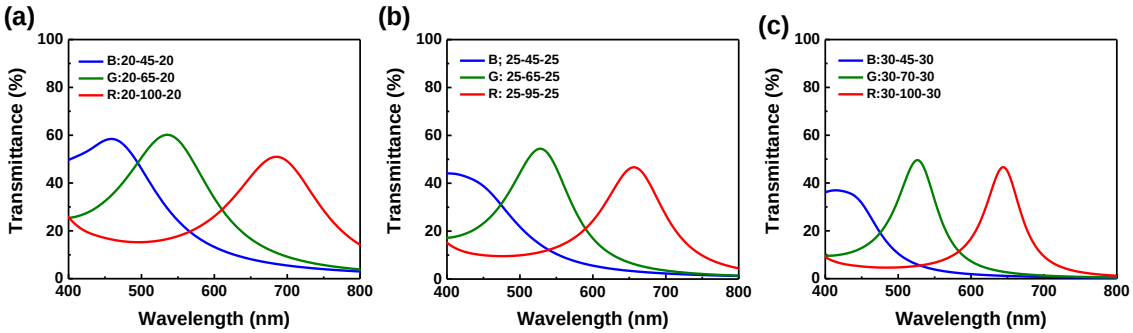

Figure 3. 5. (a–c) Measured transmittance spectra for blue, green, and red MDM electrodes with variable Ag thicknesses of 15, 20, and 25 nm, respectively.

To find optimized optical and electrical conditions for colorful semitransparent electrodes, we fabricated films with various Ag layer thicknesses, including 20, 25, and 30 nm **(Figure. 3.5)**, while the Sb_2O_3 layer thickness was varied to produce etalon structures that transmitted red, green, and blue light. Increasing the thickness of Ag films resulted in reduced transmittance and decreased full width at half maximum for transmitted bands of light. In the context of STOSCs, one must consider not only that the transmitted wavelengths of light through MDM electrodes will affect color, but that reflected light may be re-absorbed by the photoactive layer and may thus affect the current density produced by the device. Therefore, Ag films with 25-nm thickness were found to provide the best balance of optical properties and solar cell characteristics. Therefore, this thickness was selected for more detailed characterization and device studies. Photographs of corresponding blue, green, and red MDM electrodes are shown in **Figure. 3.1c**.

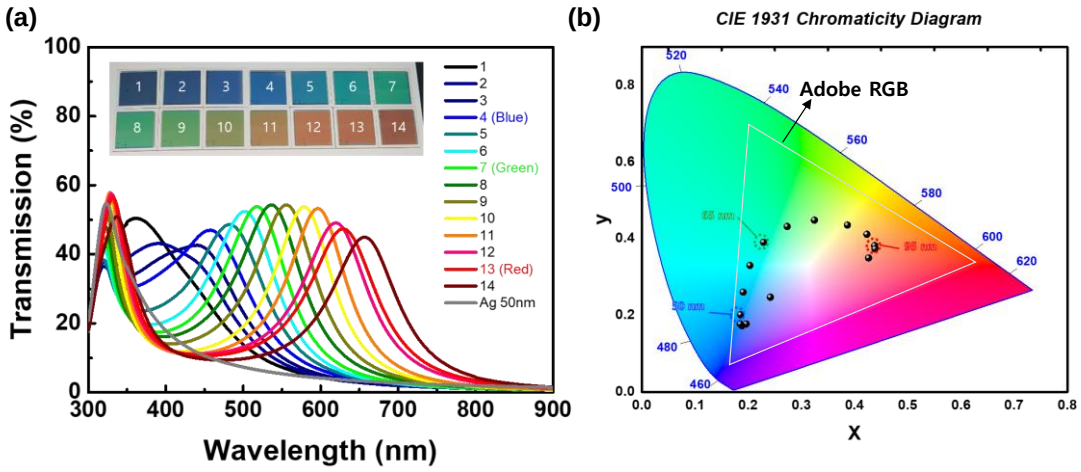

Figure 3. 6. (a) Experimental transmittance spectra of MDM electrodes with a variety of Sb_2O_3 thicknesses (Sb_2O_3 2 nm/Ag 25 nm/ Sb_2O_3 35–100 nm/Ag 25 nm) as compared to a Ag (50 nm) reference electrode. (b) Calculated color coordinates of various thicknesses of a Sb_2O_3 layer in an MDM structure on the CIE 1931 chromaticity diagram (white triangle indicates the Adobe RGB color space).

We fabricated MDM electrodes with a variety of colors by varying the thickness of the middle Sb_2O_3 layer in the etalon structure (Sb_2O_3 2 nm/Ag 25 nm/Sb_2O_3 35–100 nm/Ag 25 nm). **Figure. 3.6a** presents transmission spectra of MDM electrodes as a function of Sb_2O_3 cavity thickness. When the MDM electrode had no cavity between metallic layers (Sb_2O_3 2 nm/Ag 25 nm/Sb_2O_3 0 nm/Ag 25 nm), the structure behaved as a normal reflective metallic mirror and exhibited strong reflection throughout the visible range. However, as the Sb_2O_3 cavity layer thickness increased from 0 to 100 nm, a

transmission band with a maximum wavelength in the range of 400 to 650 nm (from bluish to reddish light) was fine-modulated. The band of transmitted light can be calculated by the following relation, which describes constructive interference modes in an etalon structure:

$$m\lambda = 2ndcos\theta \quad (3\text{-}1)$$

where *m* is the order of interference, λ is the wavelength of transmitted light, *n* is the refractive index of the cavity, *d* is the thickness of cavity, and θ is the angle of incident light. Thus, as the thickness of the Sb_2O_3 cavity increased, the wavelength of transmitted light increased following the wavelength of constructive interference modes. The measured transmission spectra shown in **Figure. 3.6a** are consistent with the aforementioned relation. For each transmission spectrum, color coordinates were calculated using international commission on illumination standards (CIE 1931). These color coordinate data are plotted in **Figure. 3.6b**. Color coordinates of MDM electrodes followed a clockwise arc through CIE space, from blue to green to red, as the thickness of the Sb_2O_3 cavity increased. Finally, the optimum blue, green and red MDM electrodes were fabricated with a configuration of Ag 25nm/Sb_2O_3 50nm/Ag25nm, Ag 25nm/Sb_2O_3 65nm/Ag25nm, and Ag 25nm/Sb_2O_3 95nm/Ag25nm, respectively.

3.4 Conclusion

In summary, we designed Sb_2O_3-cavity-based FPE electrodes that can easily be prepared by thermal evaporation, and we demonstrated their application in various color semitransparent electrodes. Various metal oxide based MDM electrodes have been reported, such as Ag/TiO_x/Ag, Ag/ITO/Ag, etc. However, TiO_x or ITO can be deposited by only e-beam evaporation or sputtering which can significantly damage the organic active layer, resulting in deterioration of device performance. However, Sb_2O_3 can be conveniently deposited by thermal evaporation to yield uniform, high-quality thin films. These attributes enable it to yield highly efficient semitransparent OSCs without damaging the active layer. The results of these are shown in Chapter 4. Furthermore, because thermally evaporated Sb_2O_3 has low parasitic absorption compared to other thermally evaporated dielectrics such as MoO_3, we were able to successfully fabricate MDM electrodes with very high transmittance, even though two 25 nm thick Ag layers were included in the electrodes.

IV. Finding Colorful (RGB) Organic Active Materials and Application Semitransparent Electrodes to OSCs.

4.1 Experimental Details

Device fabrication and characterization: OSCs were fabricated with a architecture of ITO patterned glass/PEDOT:PSS/active material/ZnO NPs/Sb_2O_3 (2 nm)/Ag (50 or 100 nm) or MDM electrodes. ITO substrates were sequentially cleaned with distilled water, acetone, and isopropanol by ultrasonication for 10 min. The substrates were dried at 100°C overnight. The cleaned ITO substrates were UV-ozone treated for 30 min and PEDOT:PSS (AI4083) layers were spin-coated onto the cleaned ITO substrate and annealed at 150 °C for 10 min in air.

Photoactive layer solutions were prepared as follows. For high efficiency colored active layers, J52:IEICO-4F:NIDCS-HO (0.9:1:0.1; 10 mg/mL for J52) in CB:1-chloronaphthalene (CN) (99:1 v/v), PTB7-Th:CO_i8DFIC:PC_{71}BM (1:1.05:0.45; 10 mg/mL for PTB7-Th) in CB:CN (99:1 v/v), PM6:Y6 (1:1.2; total of 16 mg/mL) in chloroform (CF):CN (99.5:0.5 v/v) were used to prepare red, green, and blue active layers, respectively. **Fig. 4.1** displays the molecular structures of all active materials which are used in this work.

Each blend solution was then spin-coated onto PEDOT:PSS layers at 2000 rpm for 40 s, at 2000 rpm for 40 s, at 1000 rpm for 40 s, and at 3000 rpm for 40 s for achromatic, red, green, and blue, respectively. ZnO NPs solutions were spin-coated on top of the active layer as electron transport layers. Subsequently, all devices were completed by thermal evaporation of top electrodes at pressures below 10^{-6} Torr.

The *J-V* characteristics of the devices were measured using a Keithley 2635A source measure unit in a N_2-filled glove box. A mask (4 mm^2) made of a thin metal was attached to each cell before characterization under AM 1.5 G illumination at 100 mW cm^{-2}. Light intensity dependence of the J_{SC} was measured using neutral density filters. The EQEs of the devices were measured by employing a PV measurements QE system using monochromatic light from a Xenon lamp under ambient conditions. The intensity was calibrated relative to a standard Si photodiode. To avoid overestimation by double-pass effect, the *J-V* characteristics and the EQEs of all semitransparent devices were measured on a matte black backdrop.[228] A Varian Cary 5000 spectrophotometer was used to determine the transmittance of MDM electrodes and devices.

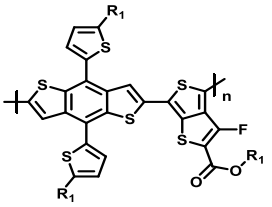

PTB7-Th

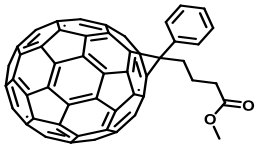

$PC_{71}BM$

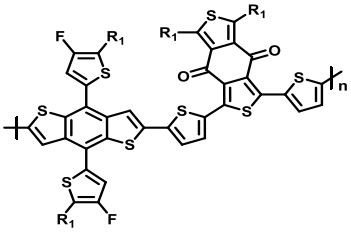

PM6

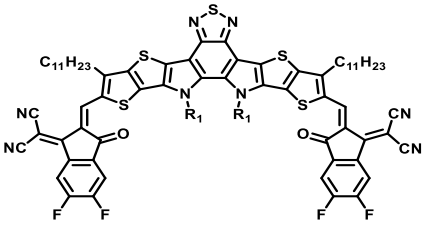

Y6

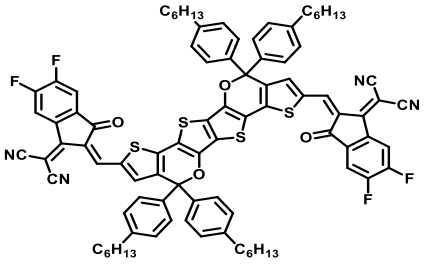

CO_i8DFIC

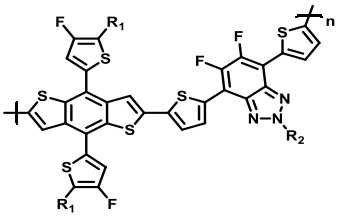

J52

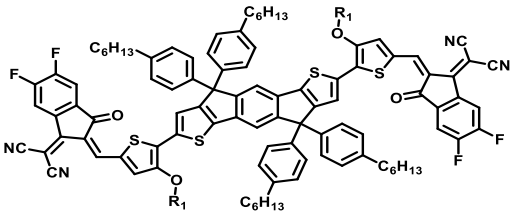

IEICO-4F

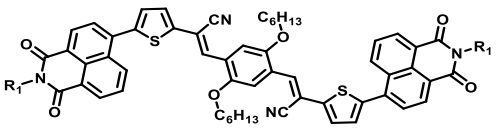

NIDCS-HO

R_1=2-ethylhexyl
R_2=2-hexyldecyl

Figure 4. 1. Molecular structures of active materials in this work.

4.2 Results and Discussion

Application MDM electrodes to OSCs

We fabricated conventional OSCs with a device configuration of glass/ITO/poly(3,4-ethylenedioxythiophene):poly(styrenesulfonate) (PEDOT:PSS)/PTB7-Th:$PC_{71}BM$/ZnO NPs/Sb_2O_3 (2 nm)/MDM electrodes or Ag (50 or 100 nm). As high color-rendering-index value materials, PTB7-Th:$PC_{71}BM$ blends were used in our studies. We prepared ~100nm thick active layer films using a PTB7-Th:$PC_{71}BM$ blends ratio was 1:1.5 (by weight). **Figure. 4.2a** shows both our device and MDM electrode structures as well as a digital photograph of devices with integrated MDM electrodes (top: reflected color, bottom: transmitted color of MDM electrodes) and **Figure. 4.2b** displays the schematic of the dichroic effect of MDM electrode structure and solar cell device architecture. Because the MDM electrodes had high transmittance at specific wavelengths and high reflectance at other wavelengths, the active layers could reabsorb a broad spectrum of light that was reflected from the MDM electrodes. [233] This contrasts with most well-known transparent electrodes such as thin metal films, graphene, Ag NWs, and ITO, which transmit broad ranges of light indiscriminately and/or parasitically absorb light. [234-239] In other words, photocurrent losses in devices with MDM electrodes can be less than in other STOSCs.

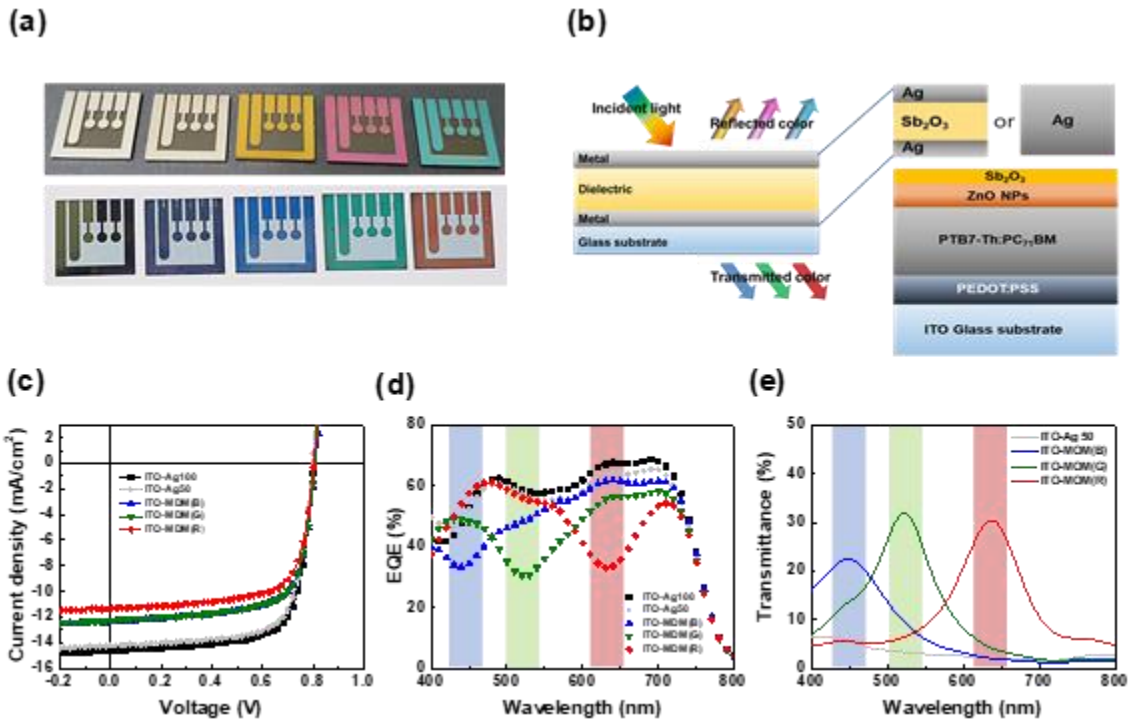

Figure 4. 2. (a) Digital photograph of devices with Ag 100 nm, Ag 50 nm, and blue, green, red MDM electrodes. The top images show reflected colors and the bottom images show transmitted colors. (b) Schematic of the dichroic effect of MDM electrode structure and solar cell device architecture.

Measured device characteristics including (c) *J-V* curves, (d) EQE spectra, and (e) transmittance of OSCs fabricated with Ag (100 nm), Ag (50 nm), blue, green, and red MDM electrodes.

Table 4. 1. Photovoltaic performance parameters and T_{MAX} of the OSCs with Ag (100 nm), Ag (50 nm), blue, green, red MDM electrodes under AM1.5G 100 mW cm^{-2} illumination.

Top electrode	J_{SC} (mA cm^{-2})	Cal. J_{sc} (mA cm^{-2})	V_{OC} (V)	FF	PCE[a)] (%)	T_{MAX} (%)
Ag 100 nm	14.63	14.68	0.80	0.72	8.49 (8.42±0.13)	-
Ag 50 nm	14.23	14.21	0.80	0.72	8.16 (8.15±0.12)	19.48 @ 325 nm
MDM (B)	12.37	12.75	0.81	0.70	7.03 (6.80±0.19)	22.50 @ 448 nm
MDM (G)	12.16	11.51	0.80	0.72	6.99 (6.92±0.09)	31.91 @ 522 nm
MDM (R)	11.36	11.86	0.80	0.71	6.43 (6.10±0.34)	30.41 @ 636 nm

[a)]Averaged PCEs and standard deviations obtained from 10 devices are stated in parenthesis.

Figure. 4.2c–e present the current density-voltage (*J-V*) curves and external quantum efficiency (EQE) spectra and transmittance of STOSCs fabricated with various electrodes including Ag (100 nm), Ag (50 nm), blue, green, and red MDM electrodes. All devices were characterized under AM 1.5 G illumination at 100 mW cm^{-2} intensity. The corresponding device parameters are summarized in **Table 4.1** The device parameters were taken from the best performing device, whereas the power conversion efficiencies (PCEs) are reported for both the champion device as well as the average of six devices. A reference device with a 100-nm thick Ag top electrode was included for comparison. The reference device exhibited a PCE of 8.49%, including a short-circuit current density (J_{sc}) of 14.63 mA cm^{-2}, open-circuit voltage (V_{oc}) of 0.80 V, and fill factor (FF) of 0.72. When the MDM electrodes had no cavity (t = 0, Ag 50 nm), a PCE of 8.16% (J_{sc} = 14.23 mA cm^{-2}, V_{oc} = 0.80 V, and FF = 0.72) was observed. The slightly lower J_{SC} and PCE could be attributed to incomplete reflection of the 50-nm-thick Ag electrode, which led to lower photocurrent generation in the active layer. Devices with blue, green, and red MDM electrodes yielded PCEs of 7.03% (J_{sc} = 12.37 mA cm^{-2}, V_{oc} = 0.81 V, and FF = 0.70), 6.99% (J_{sc} = 12.16 mA cm^{-2}, V_{oc} = 0.80 V, and FF = 0.72) and 6.43% (J_{sc} = 11.36 mA cm^{-2}, V_{oc} = 0.80 V, and FF = 0.71), respectively. Interestingly, the V_{oc} and FF of all devices were nearly identical, whereas only the J_{sc} values varied significantly. From this observation, it was apparent that devices with MDM electrodes

exhibited photocurrent losses of 15.4%, 16.9%, and 22.4% for blue, green, and red, respectively, as compared to the reference devices (Ag 100 nm). These losses were comparable to the fraction of light transmitted through the devices. **Figure. 4.2c** and **Figure. 4.2d** show the EQE and transmittance spectra of the resulting devices. Troughs in the EQE spectra occurred in the same wavelength range as the peaks in transmittance for each device. Specifically, the measured transmittance maxima were 22.50% at a wavelength of 448 nm, 31.91% at 522 nm, and 30.41% at 636 nm for the blue, green, and red devices, respectively, which again correlated well with the relative decrease in J_{SC} for each device relative to the non-transparent silver reference electrode.

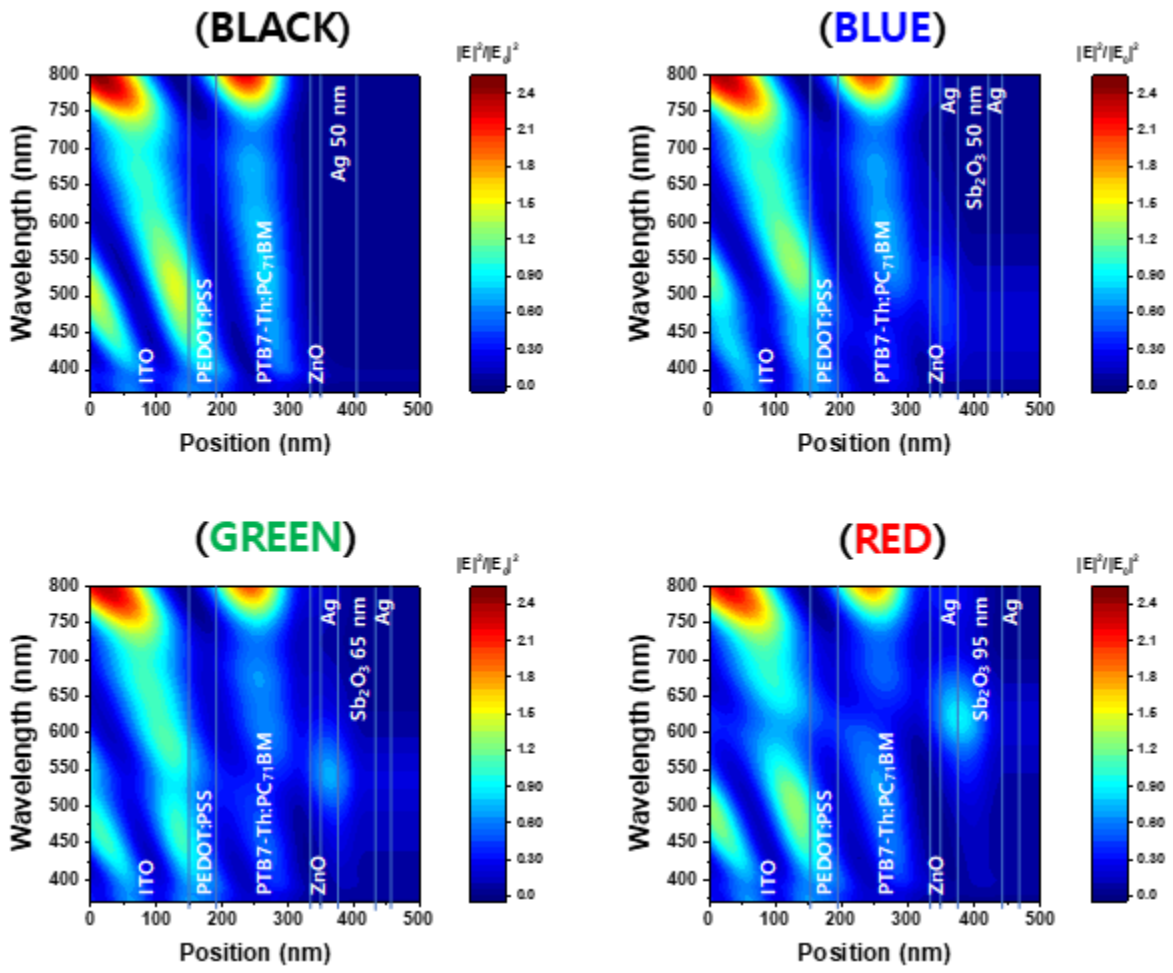

Figure 4. 3. Calculated optical field distributions of OSCs fabricated with ITO bottom electrodes and blue, green, and red MDM or Ag 50 nm top electrodes.

Spatial distributions of electric fields inside the devices were calculated using transfer matrix formalism and are shown in **Figure. 4.3**. Optical constants were taken from previously reported works or calculated from the absorption coefficients through the Kramers–Kronig relationship. [233, 240] The

structure with the reflective silver reference electrode exhibited a fairly uniform region of high field intensity spanning a wavelength range of 400 to 700 nm within the PTB7-Th:$PC_{71}BM$ layer and an optical field that quickly dropped to zero within the Ag electrode. For each colored device, the field intensity at the wavelength corresponding to its transmission maximum was significantly reduced within the active layer while being amplified within the MDM electrodes. In particular, for the blue devices, the field intensity at 400–500 nm was reduced in the PTB7-Th:$PC_{71}BM$ layer but increased for the same wavelength range within the MDM electrode. The green and red devices showed the same decrease in intensity in the active layer and the occurrence of transmission modes within the electrode at approximately 550 and 650 nm, respectively. These effects of MDM electrodes on the optical fields within the devices are consistent with the observed EQE reduction in colored devices (**Figure. 4.2c**) and observed transmittance characteristics (**Figure. 4.2d**).

Only the J_{SC} values were reduced with MDM electrodes, whereas the V_{OC} and *FF* were negligibly changed. This indicates that the MDM electrodes function well as top electrodes relative to standard Ag electrodes. To investigate whether MDM electrodes affected electronic processes within the devices, we measured the J_{SC} dependence on light intensity (I_{light}) for the photovoltaic devices with different top electrodes (including Ag (50 and 100 nm)) as well as with blue, green, and red MDM electrodes. In general, the J_{SC} values followed a power law with respect to I_{light}, thus $J_{SC} \sim I_{light}^{s}$. If *s* is close to unity, the devices have weak bimolecular recombination.[241] As **Figure. 4.4a** shows, the devices with MDM electrodes had similar *s* values of approximately 0.984 on average compared to Ag 100 nm and Ag 50 nm devices. This indicates that devices with MDM electrodes had a negligible effect on bimolecular recombination, which was like Ag electrodes. In addition, to investigate charge dissociation and collection properties, photocurrent density–effective voltage (J_{ph}–V_{eff}) properties were also investigated, where $J_{ph} = J_L - J_{dark}$ (J_L is the current density measured under illumination, whereas J_{dark} is measured under dark conditions) and $V_{eff} = V_0 - V$ (V_0 is voltage at $J_{ph} = 0$) as shown in **Figure. 4.4b**.[242] As expected, J_{ph} of all devices with MDM electrodes was slightly reduced compared to the device with reference Ag electrodes because of the fraction of light transmitted through the devices with the MDM electrodes. However, all the MDM devices showed rapid (at V_{eff} ~0.2 V) and complete saturation of photocurrent, which was comparable to Ag electrode-based reference devices. The similar photocurrent saturation indicated that charge carriers were dissociated and collected with MDM electrodes with equal efficiency as compared to Ag-based devices. These results are consistent with previous J_{SC} vs. I_{light} characteristics for the active layers used, indicating that our MDM electrodes have excellent electrical characteristics similar with Ag electrodes.

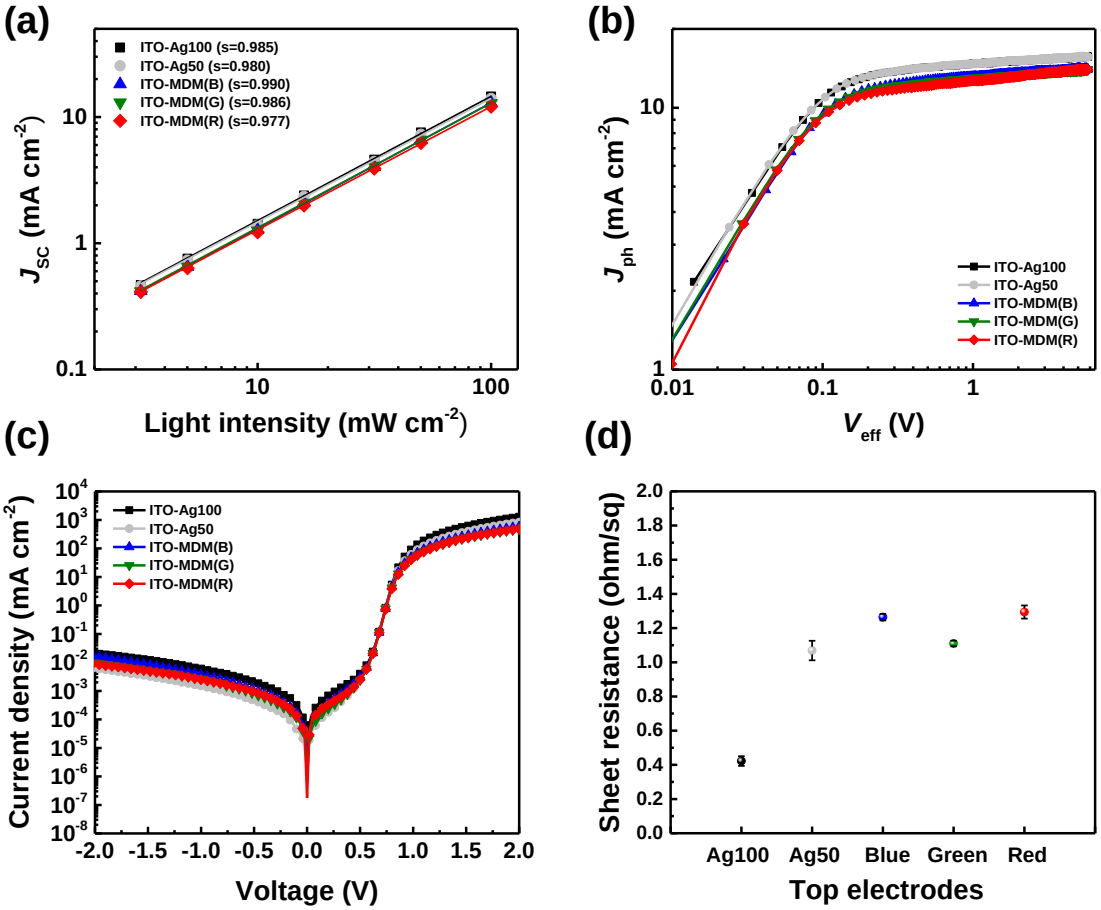

Figure 4. 4. Plots of (a) J_{SC} vs. light intensity, (b) photocurrent density vs. effective voltage (J_{ph}-V_{eff}) characteristics, and (c) dark *J*-*V* curves for the photovoltaic devices with various electrodes. (d) Average sheet resistances of the top electrodes.

Furthermore, resistance properties were investigated by analysis of dark *J*-*V* curves (**Figure. 4.4c**) of photovoltaic devices. The sheet resistances of the various electrodes are presented in **Figure. 4.4d**. Dark *J*-*V* curves of devices with MDM electrodes showed excellent diode properties with low leakage currents at reverse voltages and nearly the same rectification ratio (~10^5) as compared to Ag electrodes. In addition, suitably low sheet resistances were observed for all of the electrodes, with values of 0.42, 1.07, 1.29, 1.11, and 1.26 (Ohm/sq) on average for Ag (100 nm), Ag (50 nm), blue, green, and red MDM electrodes, respectively. These results confirm that MDM electrodes have comparably high conductivity and introduce negligible losses because of their appropriate shunt, series, and sheet resistances. The characteristics of MDM electrodes based on Sb_2O_3 demonstrate that they are outstanding color-filtering electrodes that can be used to fabricate high-efficiency STOSCs without losses in *FF* or V_{OC}.

Finally, to achieve high-efficiency STOSCs with even greater color saturation, we fabricated STOSCs in which the colors of the MDM electrodes were matched to the colors of different active layer materials. For demonstration of STOSCs using FPE-structured electrodes, we first employed PTB7-Th:$PC_{71}BM$ as an active material, because of the broad absorption covering a whole visible range, high performance and desirable optoelectronic properties of PTB7-Th:$PC_{71}BM$.[243] However, these types of semitransparent colored OSCs with active materials that absorb uniformly across the visible spectrum (such as PTB7-Th:$PC_{71}BM$) show relatively large photocurrent losses, as the band of transmitted light causes a significant decrease in EQE at the same wavelengths. To reduce this photocurrent loss, we applied MDM electrodes to active materials with low absorption coefficients at the same wavelengths as the transmission bands of the MDM electrodes.

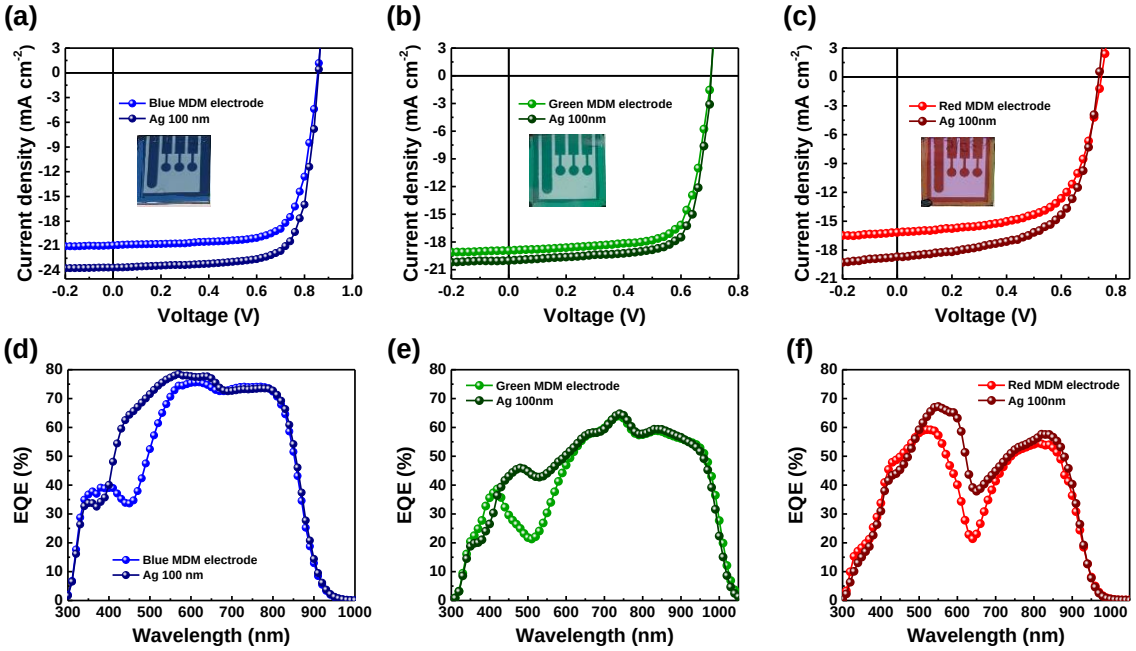

Figure 4. 5. *J-V* curves and EQE spectra of the control (Ag 100 nm) and semitransparent (blue, green, red MDM electrodes) devices based on (a, d) PM6:Y6 as blue active materials, (b, e) PTB7-Th:CO_i8DFIC:$PC_{71}BM$ as green active materials, (c, f) J52:IEICO-4F:NIDCS-HO as red active materials, respectively, under AM1.5G (100 mW cm^{-2}) illumination.

Conventional type devices were prepared with active layers consisting of PM6:Y6, PTB7-Th:CO_i8DFIC:$PC_{71}BM$, and J52:IEICO-4F:NIDCS-HO as blue, green, and red active layer materials, respectively (see molecular structures in **Fig. 4.1**). [244-246] To compare the relative photo current losses, a reference device with a Ag (100-nm) top electrode was also prepared and characterized alongside STOSCs with blue, green, and red MDM electrodes. **Fig. 4.5** reports the *J-V* curves and EQE spectra

of these devices. Corresponding transmittance spectra of these semitransparent devices are included in **Fig. 4.6**, and the device parameters are summarized in **Table 4.2.**

Table 4. 2. Photovoltaic performance parameters and T_{MAX} of the OSCs with red, green, and blue active materials and MDM electrodes under AM1.5G (100 mW cm^{-2}) illumination.

Active Materials	**Top Electrode**	J_{SC} **(mA cm^{-2})**	**Cal.** J_{SC} **(mA cm^{-2})**	V_{OC} **(V)**	**FF**	**PCE (%)**	T_{MAX} **(%)**
PM6:Y6	Ag 100 nm	23.6	22.5	0.86	0.75	15.1	-
	MDM (B)	20.9	20.5	0.86	0.74	13.3	24.6 @ 445nm
PTB7-Th: CO*i*8DFIC: $PC_{71}BM$	Ag 100 nm	20.0	19.4	0.71	0.74	10.5	-
	MDM (G)	18.9	18.0	0.70	0.73	9.71	35.4 @ 511 nm
J52: IEICO-4F: NIDCS-HO	Ag 100 nm	18.7	17.7	0.74	0.63	8.62	-
	MDM (R)	16.2	15.7	0.75	0.63	7.63	34.7 @ 633 nm

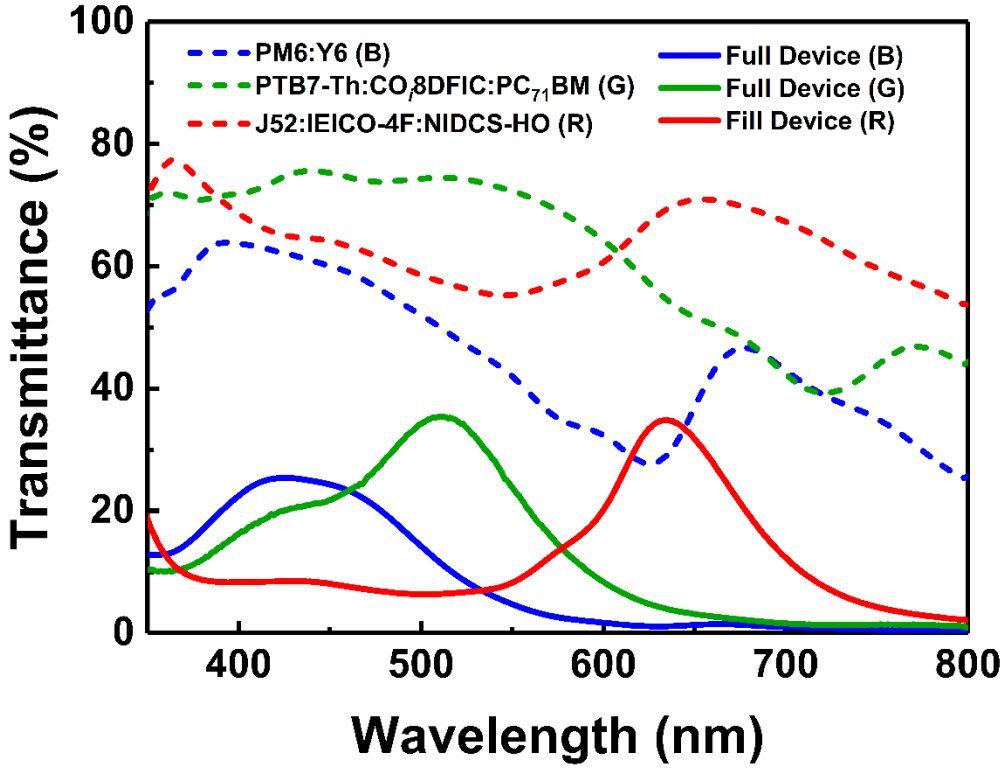

Figure 4. 6. Transmittance spectra of blue, green, and red semitransparent devices without MDM electrodes and integrating B, G, and R MDM electrodes, respectively. Different active layers were chosen to optimize the transmittance of specific wavelengths of light. (Dash line: ITO/PEDOT:PSS/Active layer/ZnO(ETL), solid line: ITO/PEDOT:PSS/Active layer/ZnO(ETL)/Sb_2O_3 /Ag/ Sb_2O_3/Ag)

As expected, the photocurrent losses of semitransparent devices with spectrally matched active layer materials were less than those for devices using PTB7-Th:$PC_{71}BM$. The spectrally matched STOSCs showed a J_{SC} loss of 11.4% (23.6→20.9 mA cm^{-2}), 5.5% (20.0→18.9 mA cm^{-2}) and 13.3% (18.7→16.2 mA cm^{-2}) for blue, green and red colored devices, respectively, compared to the reference device with a 100nm-thick Ag electrode. In comparison, semitransparent blue, green, and red STOSCs using PTB7-Th:$PC_{71}BM$ as an active material showed photocurrent losses of 15.4%, 16.9%, and 22.4%, respectively. These results demonstrate clearly that photocurrent losses in semitransparent devices can be minimized by color matching of active layer materials to the transmission bands of MDM electrodes. Using this approach, we successfully achieved outstanding PCEs of 13.3% (T_{MAX} 24.6% @ 445nm), 9.71% (T_{MAX} 35.4% @ 511nm), and 7.63% (T_{MAX} 34.7% @ 633nm) for blue, green and red STOSCs, respectively. Moreover, excellent transmittance spectra with relatively narrow but intense transmission bands at each wavelength were achieved (see **Fig. 4.6**), leading to devices with more saturated and vivid colors.

4.3 Conclusion

In this study, we investigated two types of colorful and semitransparent OSCs based on achromatic (PTB7-Th:$PC_{71}BM$) and chromatic (PM6:Y6, PTB7-Th:CO_i8DFIC:$PC_{71}BM$ and J52:IEICO-4F:NIDCS-HO as blue, green and red active materials) photoactive layers with MDM electrodes. We successfully demonstrated vivid colored, R/G/B semitransparent OSCs using achromatic active layers, showing PCEs of 7.03, 6.99 and 6.43% with blue, green, and red MDM electrodes, respectively. In addition, we demonstrated that the photocurrent losses in colorful, semitransparent OSCs could be significantly reduced by matching the chromatic active layer with the transmittance maxima of the R/G/B MDM electrodes. Optical losses were minimized by carefully selecting active layer materials such that their intrinsic transmission bands matched well with the transmission maxima of the MDM electrodes. Finally, we achieved outstanding efficiencies of as high as 13.3% in PM6:Y6 STOSCs using blue semitransparent electrodes.

References

1. The history of solar cells. https://www1.eere.energy.gov/solar/pdfs/solar_timeline.pdf.
2. best-research-cell-efficiencies. https://www.nrel.gov/pv/assets/pdfs/best-research-cell-efficiencies.20200218.pdf.
3. Global solar PV installation status and forecast (2001~2023).
4. Tang, C. W., Two-layer organic photovoltaic cell. *Applied Physics Letters* **1986,** *48* (2), 183-185.
5. Sariciftci, N. S.; Smilowitz, L.; Heeger, A. J.; Wudl, F., Photoinduced Electron Transfer from a Conducting Polymer to Buckminsterfullerene. *Science* **1992,** *258* (5087), 1474-1476.
6. Shin, D. H.; Choi, S.-H., Recent Studies of Semitransparent Solar Cells. *Coatings* **2018,** *8* (10), 329.
7. Liu, Z.; You, P.; Liu, S.; Yan, F., Neutral-Color Semitransparent Organic Solar Cells with All-Graphene Electrodes. *ACS Nano* **2015,** *9* (12), 12026-12034.
8. Chen, C.-C.; Dou, L.; Zhu, R.; Chung, C.-H.; Song, T.-B.; Zheng, Y. B.; Hawks, S.; Li, G.; Weiss, P. S.; Yang, Y., Visibly Transparent Polymer Solar Cells Produced by Solution Processing. *ACS Nano* **2012,** *6* (8), 7185-7190.
9. Chen, C.-C.; Dou, L.; Gao, J.; Chang, W.-H.; Li, G.; Yang, Y., High-performance semi-transparent polymer solar cells possessing tandem structures. *Energy & Environmental Science* **2013,** *6* (9), 2714-2720.
10. Chang, C.-Y.; Zuo, L.; Yip, H.-L.; Li, Y.; Li, C.-Z.; Hsu, C.-S.; Cheng, Y.-J.; Chen, H.; Jen, A. K.-Y., A Versatile Fluoro-Containing Low-Bandgap Polymer for Efficient Semitransparent and Tandem Polymer Solar Cells. *Advanced Functional Materials* **2013,** *23* (40), 5084-5090.
11. Chen, K.-S.; Salinas, J.-F.; Yip, H.-L.; Huo, L.; Hou, J.; Jen, A. K. Y., Semi-transparent polymer solar cells with 6% PCE, 25% average visible transmittance and a color rendering index close to 100 for power generating window applications. *Energy & Environmental Science* **2012,** *5* (11), 9551-9557.
12. Yu, W.; Jia, X.; Long, Y.; Shen, L.; Liu, Y.; Guo, W.; Ruan, S., Highly Efficient Semitransparent Polymer Solar Cells with Color Rendering Index Approaching 100 Using One-Dimensional Photonic Crystal. *ACS Applied Materials & Interfaces* **2015,** *7* (18), 9920-9928.
13. Wang, W.; Yan, C.; Lau, T.-K.; Wang, J.; Liu, K.; Fan, Y.; Lu, X.; Zhan, X., Fused Hexacyclic Nonfullerene Acceptor with Strong Near-Infrared Absorption for Semitransparent Organic Solar Cells with 9.77% Efficiency. *Advanced Materials* **2017,** *29* (31), 1701308.
14. Kim, Y.; Son, J.; Shafian, S.; Kim, K.; Hyun, J. K., Semitransparent Blue, Green, and Red Organic Solar Cells Using Color Filtering Electrodes. *Advanced Optical Materials* **2018,**

6 (13), 1800051.

15. Lu, J.-H.; Lin, Y.-H.; Jiang, B.-H.; Yeh, C.-H.; Kao, J.-C.; Chen, C.-P., Microcavity Structure Provides High-Performance (>8.1%) Semitransparent and Colorful Organic Photovoltaics. *Advanced Functional Materials* **2018,** *28* (7), 1703398.
16. Zhong, J.; Xiao, Z.; Liang, W.; Wu, Y.; Ye, Q.; Xu, H.; Deng, H.; Shen, L.; Feng, X.; Long, Y., Highly Efficient and High Peak Transmittance Colorful Semitransparent Organic Solar Cells with Hybrid-Electrode-Mirror Microcavity Structure. *ACS Applied Materials & Interfaces* **2019,** *11* (51), 47992-48001.
17. Yu, G.; Gao, J.; Hummelen, J. C.; Wudl, F.; Heeger, A. J., Polymer Photovoltaic Cells: Enhanced Efficiencies via a Network of Internal Donor-Acceptor Heterojunctions. *Science* **1995,** *270* (5243), 1789.
18. Chen, J.; Cao, Y., Development of Novel Conjugated Donor Polymers for High-Efficiency Bulk-Heterojunction Photovoltaic Devices. *Accounts of Chemical Research* **2009,** *42* (11), 1709-1718.
19. Dennler, G.; Scharber, M. C.; Brabec, C. J., Polymer-Fullerene Bulk-Heterojunction Solar Cells. *Advanced Materials* **2009,** *21* (13), 1323-1338.
20. Krebs, F. C., Fabrication and processing of polymer solar cells: A review of printing and coating techniques. *Solar Energy Materials and Solar Cells* **2009,** *93* (4), 394-412.
21. Li, C.; Liu, M.; Pschirer, N. G.; Baumgarten, M.; Müllen, K., Polyphenylene-Based Materials for Organic Photovoltaics. *Chemical Reviews* **2010,** *110* (11), 6817-6855.
22. Szarko, J. M.; Guo, J.; Liang, Y.; Lee, B.; Rolczynski, B. S.; Strzalka, J.; Xu, T.; Loser, S.; Marks, T. J.; Yu, L.; Chen, L. X., When Function Follows Form: Effects of Donor Copolymer Side Chains on Film Morphology and BHJ Solar Cell Performance. *Advanced Materials* **2010,** *22* (48), 5468-5472.
23. Chen, H.-Y.; Hou, J.; Zhang, S.; Liang, Y.; Yang, G.; Yang, Y.; Yu, L.; Wu, Y.; Li, G., Polymer solar cells with enhanced open-circuit voltage and efficiency. *Nature Photonics* **2009,** *3* (11), 649-653.
24. Liang, Y.; Xu, Z.; Xia, J.; Tsai, S.-T.; Wu, Y.; Li, G.; Ray, C.; Yu, L., For the Bright Future—Bulk Heterojunction Polymer Solar Cells with Power Conversion Efficiency of 7.4%. *Advanced Materials* **2010,** *22* (20), E135-E138.
25. Kim, J.; Yun, M. H.; Anant, P.; Cho, S.; Jacob, J.; Kim, J. Y.; Yang, C., Copolymers Comprising 2,7-Carbazole and Bis-benzothiadiazole Units for Bulk-Heterojunction Solar Cells. *Chemistry – A European Journal* **2011,** *17* (51), 14681-14688.
26. Kim, B.; Yeom, H. R.; Yun, M. H.; Kim, J. Y.; Yang, C., A Selenophene Analogue of PCDTBT: Selective Fine-Tuning of LUMO to Lower of the Bandgap for Efficient Polymer Solar Cells. *Macromolecules* **2012,** *45* (21), 8658-8664.

27. Liu, J.; Tanaka, T.; Sivula, K.; Alivisatos, A. P.; Fréchet, J. M. J., Employing End-Functional Polythiophene To Control the Morphology of Nanocrystal−Polymer Composites in Hybrid Solar Cells. *Journal of the American Chemical Society* **2004,** *126* (21), 6550-6551.
28. Li, G.; Shrotriya, V.; Huang, J.; Yao, Y.; Moriarty, T.; Emery, K.; Yang, Y., High-efficiency solution processable polymer photovoltaic cells by self-organization of polymer blends. *Nature Materials* **2005,** *4* (11), 864-868.
29. Ma, W.; Yang, C.; Gong, X.; Lee, K.; Heeger, A. J., Thermally Stable, Efficient Polymer Solar Cells with Nanoscale Control of the Interpenetrating Network Morphology. *Advanced Functional Materials* **2005,** *15* (10), 1617-1622.
30. Peet, J.; Kim, J. Y.; Coates, N. E.; Ma, W. L.; Moses, D.; Heeger, A. J.; Bazan, G. C., Efficiency enhancement in low-bandgap polymer solar cells by processing with alkane dithiols. *Nature Materials* **2007,** *6* (7), 497-500.
31. Lee, J. K.; Ma, W. L.; Brabec, C. J.; Yuen, J.; Moon, J. S.; Kim, J. Y.; Lee, K.; Bazan, G. C.; Heeger, A. J., Processing Additives for Improved Efficiency from Bulk Heterojunction Solar Cells. *Journal of the American Chemical Society* **2008,** *130* (11), 3619-3623.
32. Hoven, C. V.; Dang, X.-D.; Coffin, R. C.; Peet, J.; Nguyen, T.-Q.; Bazan, G. C., Improved Performance of Polymer Bulk Heterojunction Solar Cells Through the Reduction of Phase Separation via Solvent Additives. *Advanced Materials* **2010,** *22* (8), E63-E66.
33. Su, M.-S.; Kuo, C.-Y.; Yuan, M.-C.; Jeng, U.-S.; Su, C.-J.; Wei, K.-H., Improving Device Efficiency of Polymer/Fullerene Bulk Heterojunction Solar Cells Through Enhanced Crystallinity and Reduced Grain Boundaries Induced by Solvent Additives. *Advanced Materials* **2011,** *23* (29), 3315-3319.
34. Chen, W.; Nikiforov, M. P.; Darling, S. B., Morphology characterization in organic and hybrid solar cells. *Energy & Environmental Science* **2012,** *5* (8), 8045-8074.
35. Yip, H.-L.; Jen, A. K. Y., Recent advances in solution-processed interfacial materials for efficient and stable polymer solar cells. *Energy & Environmental Science* **2012,** *5* (3), 5994-6011.
36. Henson, Z. B.; Müllen, K.; Bazan, G. C., Design strategies for organic semiconductors beyond the molecular formula. *Nature Chemistry* **2012,** *4* (9), 699-704.
37. Scharber, M. C.; Mühlbacher, D.; Koppe, M.; Denk, P.; Waldauf, C.; Heeger, A. J.; Brabec, C. J., Design Rules for Donors in Bulk-Heterojunction Solar Cells—Towards 10 % Energy-Conversion Efficiency. *Advanced Materials* **2006,** *18* (6), 789-794.
38. Kim, G.; Yeom, H. R.; Cho, S.; Seo, J. H.; Kim, J. Y.; Yang, C., Easily Attainable Phenothiazine-Based Polymers for Polymer Solar Cells: Advantage of Insertion of S,S-dioxides into its Polymer for Inverted Structure Solar Cells. *Macromolecules* **2012,** *45* (4),

1847-1857.

39. Yang, L.; Tumbleston, J. R.; Zhou, H.; Ade, H.; You, W., Disentangling the impact of side chains and fluorine substituents of conjugated donor polymers on the performance of photovoltaic blends. *Energy & Environmental Science* **2013,** *6* (1), 316-326.
40. Wang, E.; Wang, L.; Lan, L.; Luo, C.; Zhuang, W.; Peng, J.; Cao, Y., High-performance polymer heterojunction solar cells of a polysilafluorene derivative. *Applied Physics Letters* **2008,** *92* (3), 033307.
41. Svensson, M.; Zhang, F.; Veenstra, S. C.; Verhees, W. J. H.; Hummelen, J. C.; Kroon, J. M.; Inganäs, O.; Andersson, M. R., High-Performance Polymer Solar Cells of an Alternating Polyfluorene Copolymer and a Fullerene Derivative. *Advanced Materials* **2003,** *15* (12), 988-991.
42. Blouin, N.; Michaud, A.; Gendron, D.; Wakim, S.; Blair, E.; Neagu-Plesu, R.; Belletête, M.; Durocher, G.; Tao, Y.; Leclerc, M., Toward a Rational Design of Poly(2,7-Carbazole) Derivatives for Solar Cells. *Journal of the American Chemical Society* **2008,** *130* (2), 732-742.
43. Park, S. H.; Roy, A.; Beaupré, S.; Cho, S.; Coates, N.; Moon, J. S.; Moses, D.; Leclerc, M.; Lee, K.; Heeger, A. J., Bulk heterojunction solar cells with internal quantum efficiency approaching 100%. *Nature Photonics* **2009,** *3* (5), 297-302.
44. Loser, S.; Bruns, C. J.; Miyauchi, H.; Ortiz, R. P.; Facchetti, A.; Stupp, S. I.; Marks, T. J., A Naphthodithiophene-Diketopyrrolopyrrole Donor Molecule for Efficient Solution-Processed Solar Cells. *Journal of the American Chemical Society* **2011,** *133* (21), 8142-8145.
45. Wang, T.; Pearson, A. J.; Lidzey, D. G.; Jones, R. A. L., Evolution of Structure, Optoelectronic Properties, and Device Performance of Polythiophene:Fullerene Solar Cells During Thermal Annealing. *Advanced Functional Materials* **2011,** *21* (8), 1383-1390.
46. Li, G.; Yao, Y.; Yang, H.; Shrotriya, V.; Yang, G.; Yang, Y., "Solvent Annealing" Effect in Polymer Solar Cells Based on Poly(3-hexylthiophene) and Methanofullerenes. *Advanced Functional Materials* **2007,** *17* (10), 1636-1644.
47. Miller, S.; Fanchini, G.; Lin, Y.-Y.; Li, C.; Chen, C.-W.; Su, W.-F.; Chhowalla, M., Investigation of nanoscale morphological changes in organic photovoltaics during solvent vapor annealing. *Journal of Materials Chemistry* **2008,** *18* (3), 306-312.
48. Etzold, F.; Howard, I. A.; Forler, N.; Cho, D. M.; Meister, M.; Mangold, H.; Shu, J.; Hansen, M. R.; Müllen, K.; Laquai, F., The Effect of Solvent Additives on Morphology and Excited-State Dynamics in PCPDTBT:PCBM Photovoltaic Blends. *Journal of the American Chemical Society* **2012,** *134* (25), 10569-10583.
49. Wang, E.; Hou, L.; Wang, Z.; Hellström, S.; Zhang, F.; Inganäs, O.; Andersson, M. R., An Easily Synthesized Blue Polymer for High-Performance Polymer Solar Cells. *Advanced*

Materials **2010,** *22* (46), 5240-5244.

50. Zhou, H.; Yang, L.; Price, S. C.; Knight, K. J.; You, W., Enhanced Photovoltaic Performance of Low-Bandgap Polymers with Deep LUMO Levels. *Angewandte Chemie International Edition* **2010,** *49* (43), 7992-7995.
51. Wang, Z.; Wang, E.; Hou, L.; Zhang, F.; Andersson, M.; Inganäs, O., Mixed solvents for reproducible photovoltaic bulk heterojunctions. *Journal of Photonics for Energy* **2011,** *1* (1), 011122.
52. Yamamoto, T.; Lee, B.-L.; Kokubo, H.; Kishida, H.; Hirota, K.; Wakabayashi, T.; Okamoto, H., Synthesis of a New Thiophene/Quinoxaline CT-Type Copolymer with High Solubility and Its Basic Optical Properties. *Macromolecular Rapid Communications* **2003,** *24* (7), 440-443.
53. Gadisa, A.; Mammo, W.; Andersson, L. M.; Admassie, S.; Zhang, F.; Andersson, M. R.; Inganäs, O., A New Donor–Acceptor–Donor Polyfluorene Copolymer with Balanced Electron and Hole Mobility. *Advanced Functional Materials* **2007,** *17* (18), 3836-3842.
54. Donley, C. L.; Zaumseil, J.; Andreasen, J. W.; Nielsen, M. M.; Sirringhaus, H.; Friend, R. H.; Kim, J.-S., Effects of Packing Structure on the Optoelectronic and Charge Transport Properties in Poly(9,9-di-n-octylfluorene-alt-benzothiadiazole). *Journal of the American Chemical Society* **2005,** *127* (37), 12890-12899.
55. Kronemeijer, A. J.; Gili, E.; Shahid, M.; Rivnay, J.; Salleo, A.; Heeney, M.; Sirringhaus, H., A Selenophene-Based Low-Bandgap Donor–Acceptor Polymer Leading to Fast Ambipolar Logic. *Advanced Materials* **2012,** *24* (12), 1558-1565.
56. Thompson, B. C.; Fréchet, J. M. J., Polymer–Fullerene Composite Solar Cells. *Angewandte Chemie International Edition* **2008,** *47* (1), 58-77.
57. Lee, J. K.; Wang, Y.-M.; Cho, S.; Wudl, F.; Heeger, A. J., New approach for forming bulk-heterojunction solar cells comprising a π-conjugated polymer and C60. *Organic Electronics* **2009,** *10* (7), 1223-1227.
58. Lee, J. K.; Wang, Y.-M.; Cho, S.; Wudl, F.; Heeger, A. J., New approach for forming bulk-heterojunction solar cells comprising a π-conjugated polymer and C60. *Org. Electrons.* **2009,** *10* (7), 1223-1227.
59. Chiu, M.-Y.; Jeng, U.-S.; Su, C.-H.; Liang, K. S.; Wei, K.-H., Simultaneous Use of Small- and Wide-Angle X-ray Techniques to Analyze Nanometerscale Phase Separation in Polymer Heterojunction Solar Cells. *Advanced Materials* **2008,** *20* (13), 2573-2578.
60. Chiu, M.-Y.; Jeng, U. S.; Su, M.-S.; Wei, K.-H., Morphologies of Self-Organizing Regioregular Conjugated Polymer/Fullerene Aggregates in Thin Film Solar Cells. *Macromolecules* **2010,** *43* (1), 428-432.
61. Mihailetchi, V. D.; Koster, L. J. A.; Blom, P. W. M.; Melzer, C.; de Boer, B.;

van Duren, J. K. J.; Janssen, R. A. J., Compositional Dependence of the Performance of Poly(p-phenylene vinylene):Methanofullerene Bulk-Heterojunction Solar Cells. *Advanced Functional Materials* **2005,** *15* (5), 795-801.

62. Zhao, G.; He, Y.; Xu, Z.; Hou, J.; Zhang, M.; Min, J.; Chen, H.-Y.; Ye, M.; Hong, Z.; Yang, Y.; Li, Y., Effect of Carbon Chain Length in the Substituent of PCBM-like Molecules on Their Photovoltaic Properties. *Advanced Functional Materials* **2010,** *20* (9), 1480-1487.
63. Bundgaard, E.; Krebs, F. C., Low band gap polymers for organic photovoltaics. *Solar Energy Materials and Solar Cells* **2007,** *91* (11), 954-985.
64. Yun, M. H.; Kim, G.-H.; Yang, C.; Kim, J. Y., Towards optimization of P3HT:bisPCBM composites for highly efficient polymer solar cells. *Journal of Materials Chemistry* **2010,** *20* (36), 7710-7714.
65. Yang, C.; Lee, J. K.; Heeger, A. J.; Wudl, F., Well-defined donor–acceptor rod–coil diblock copolymers based on P3HT containing C60: the morphology and role as a surfactant in bulk-heterojunction solar cells. *Journal of Materials Chemistry* **2009,** *19* (30), 5416-5423.
66. Lu, G.; Usta, H.; Risko, C.; Wang, L.; Facchetti, A.; Ratner, M. A.; Marks, T. J., Synthesis, Characterization, and Transistor Response of Semiconducting Silole Polymers with Substantial Hole Mobility and Air Stability. Experiment and Theory. *Journal of the American Chemical Society* **2008,** *130* (24), 7670-7685.
67. Sonar, P.; Singh, S. P.; Li, Y.; Soh, M. S.; Dodabalapur, A., A Low-Bandgap Diketopyrrolopyrrole-Benzothiadiazole-Based Copolymer for High-Mobility Ambipolar Organic Thin-Film Transistors. *Advanced Materials* **2010,** *22* (47), 5409-5413.
68. Mayer, A. C.; Toney, M. F.; Scully, S. R.; Rivnay, J.; Brabec, C. J.; Scharber, M.; Koppe, M.; Heeney, M.; McCulloch, I.; McGehee, M. D., Bimolecular Crystals of Fullerenes in Conjugated Polymers and the Implications of Molecular Mixing for Solar Cells. *Advanced Functional Materials* **2009,** *19* (8), 1173-1179.
69. Xin, H.; Guo, X.; Ren, G.; Watson, M. D.; Jenekhe, S. A., Efficient Phthalimide Copolymer-Based Bulk Heterojunction Solar Cells: How the Processing Additive Influences Nanoscale Morphology and Photovoltaic Properties. *Advanced Energy Materials* **2012,** *2* (5), 575-582.
70. Yang, X.; van Duren, J. K. J.; Janssen, R. A. J.; Michels, M. A. J.; Loos, J., Morphology and Thermal Stability of the Active Layer in Poly(p-phenylenevinylene)/Methanofullerene Plastic Photovoltaic Devices. *Macromolecules* **2004,** *37* (6), 2151-2158.
71. Yang, X.; van Duren, J. K. J.; Rispens, M. T.; Hummelen, J. C.; Janssen, R. A. J.; Michels, M. A. J.; Loos, J., Crystalline Organization of a Methanofullerene as Used for Plastic Solar-Cell Applications. *Advanced Materials* **2004,** *16* (9-10), 802-806.

72. Erb, T.; Zhokhavets, U.; Gobsch, G.; Raleva, S.; Stühn, B.; Schilinsky, P.; Waldauf, C.; Brabec, C. J., Correlation Between Structural and Optical Properties of Composite Polymer/Fullerene Films for Organic Solar Cells. *Advanced Functional Materials* **2005,** *15* (7), 1193-1196.

73. Cates, N. C.; Gysel, R.; Beiley, Z.; Miller, C. E.; Toney, M. F.; Heeney, M.; McCulloch, I.; McGehee, M. D., Tuning the Properties of Polymer Bulk Heterojunction Solar Cells by Adjusting Fullerene Size to Control Intercalation. *Nano Letters* **2009,** *9* (12), 4153-4157.

74. Cates, N. C.; Gysel, R.; Dahl, J. E. P.; Sellinger, A.; McGehee, M. D., Effects of Intercalation on the Hole Mobility of Amorphous Semiconducting Polymer Blends. *Chemistry of Materials* **2010,** *22* (11), 3543-3548.

75. Li, Y.; Sonar, P.; Singh, S. P.; Zeng, W.; Soh, M. S., 3,6-Di(furan-2-yl)pyrrolo[3,4-c]pyrrole-1,4(2H,5H)-dione and bithiophene copolymer with rather disordered chain orientation showing high mobility in organic thin film transistors. *Journal of Materials Chemistry* **2011,** *21* (29), 10829-10835.

76. Lee, O. P.; Yiu, A. T.; Beaujuge, P. M.; Woo, C. H.; Holcombe, T. W.; Millstone, J. E.; Douglas, J. D.; Chen, M. S.; Fréchet, J. M. J., Efficient Small Molecule Bulk Heterojunction Solar Cells with High Fill Factors via Pyrene-Directed Molecular Self-Assembly. *Adv. Mater.* **2011,** *23* (45), 5359-5363.

77. Yang, L.; Sontag, S. K.; LaJoie, T. W.; Li, W.; Huddleston, N. E.; Locklin, J.; You, W., Surface-Initiated Poly(3-methylthiophene) as a Hole-Transport Layer for Polymer Solar Cells with High Performance. *ACS Applied Materials & Interfaces* **2012,** *4* (10), 5069-5073.

78. Xu, Z.; Chen, L.-M.; Yang, G.; Huang, C.-H.; Hou, J.; Wu, Y.; Li, G.; Hsu, C.-S.; Yang, Y., Vertical Phase Separation in Poly(3-hexylthiophene): Fullerene Derivative Blends and its Advantage for Inverted Structure Solar Cells. *Advanced Functional Materials* **2009,** *19* (8), 1227-1234.

79. Hsieh, C.-H.; Cheng, Y.-J.; Li, P.-J.; Chen, C.-H.; Dubosc, M.; Liang, R.-M.; Hsu, C.-S., Highly Efficient and Stable Inverted Polymer Solar Cells Integrated with a Cross-Linked Fullerene Material as an Interlayer. *Journal of the American Chemical Society* **2010,** *132* (13), 4887-4893.

80. Chen, L.-M.; Hong, Z.; Li, G.; Yang, Y., Recent Progress in Polymer Solar Cells: Manipulation of Polymer:Fullerene Morphology and the Formation of Efficient Inverted Polymer Solar Cells. *Advanced Materials* **2009,** *21* (14-15), 1434-1449.

81. Cheng, Y.-J.; Hsieh, C.-H.; He, Y.; Hsu, C.-S.; Li, Y., Combination of Indene-C60 Bis-Adduct and Cross-Linked Fullerene Interlayer Leading to Highly Efficient Inverted Polymer Solar Cells. *Journal of the American Chemical Society* **2010,** *132* (49), 17381-17383.

82. Sun, Y.; Takacs, C. J.; Cowan, S. R.; Seo, J. H.; Gong, X.; Roy, A.; Heeger, A. J., Efficient, Air-Stable Bulk Heterojunction Polymer Solar Cells Using MoOx as the Anode Interfacial Layer. *Advanced Materials* **2011,** *23* (19), 2226-2230.

83. Small, C. E.; Chen, S.; Subbiah, J.; Amb, C. M.; Tsang, S.-W.; Lai, T.-H.; Reynolds, J. R.; So, F., High-efficiency inverted dithienogermole–thienopyrrolodione-based polymer solar cells. *Nature Photonics* **2012,** *6* (2), 115-120.

84. Tan, Z. a.; Zhang, W.; Zhang, Z.; Qian, D.; Huang, Y.; Hou, J.; Li, Y., High-Performance Inverted Polymer Solar Cells with Solution-Processed Titanium Chelate as Electron-Collecting Layer on ITO Electrode. *Advanced Materials* **2012,** *24* (11), 1476-1481.

85. Shih, P.-I.; Shu, C.-F.; Tung, Y.-L.; Chi, Y., Efficient white-light-emitting diodes based on poly(N-vinylcarbazole) doped with blue fluorescent and orange phosphorescent materials. *Applied Physics Letters* **2006,** *88* (25), 251110.

86. Cheng, Y.-J.; Yang, S.-H.; Hsu, C.-S., Synthesis of Conjugated Polymers for Organic Solar Cell Applications. *Chemical Reviews* **2009,** *109* (11), 5868-5923.

87. Günes, S.; Neugebauer, H.; Sariciftci, N. S., Conjugated Polymer-Based Organic Solar Cells. *Chemical Reviews* **2007,** *107* (4), 1324-1338.

88. Yu, G.; Gao, J.; Hummelen, J. C.; Wudl, F.; Heeger, A. J., Polymer Photovoltaic Cells: Enhanced Efficiencies via a Network of Internal Donor-Acceptor Heterojunctions. *Science* **1995,** *270* (5243), 1789-1791.

89. Kim, J.; Yun, M. H.; Anant, P.; Cho, S.; Jacob, J.; Kim, J. Y.; Yang, C., Copolymers Comprising 2,7-Carbazole and Bis-benzothiadiazole Units for Bulk-Heterojunction Solar Cells. *Chemistry – A European Journal* **2011,** *17* (51), 14681-14688.

90. Cheedarala, R. K.; Kim, G.-H.; Cho, S.; Lee, J.; Kim, J.; Song, H.-K.; Kim, J. Y.; Yang, C., Ladder-type heteroacene polymers bearing carbazole and thiophene ring units and their use in field-effect transistors and photovoltaic cells. *Journal of Materials Chemistry* **2011,** *21* (3), 843-850.

91. Wang, E.; Ma, Z.; Zhang, Z.; Vandewal, K.; Henriksson, P.; Inganäs, O.; Zhang, F.; Andersson, M. R., An Easily Accessible Isoindigo-Based Polymer for High-Performance Polymer Solar Cells. *Journal of the American Chemical Society* **2011,** *133* (36), 14244-14247.

92. Price, S. C.; Stuart, A. C.; Yang, L.; Zhou, H.; You, W., Fluorine Substituted Conjugated Polymer of Medium Band Gap Yields 7% Efficiency in Polymer−Fullerene Solar Cells. *Journal of the American Chemical Society* **2011,** *133* (12), 4625-4631.

93. Huo, L.; Zhang, S.; Guo, X.; Xu, F.; Li, Y.; Hou, J., Replacing Alkoxy Groups with Alkylthienyl Groups: A Feasible Approach To Improve the Properties of Photovoltaic Polymers. *Angewandte Chemie International Edition* **2011,** *50* (41), 9697-9702.

94. Piliego, C.; Holcombe, T. W.; Douglas, J. D.; Woo, C. H.; Beaujuge, P. M.; Fréchet, J.

M. J., Synthetic Control of Structural Order in N-Alkylthieno[3,4-c]pyrrole-4,6-dione-Based Polymers for Efficient Solar Cells. *Journal of the American Chemical Society* **2010,** *132* (22), 7595-7597.

95. Chen, H.-Y.; Hou, J.; Zhang, S.; Liang, Y.; Yang, G.; Yang, Y.; Yu, L.; Wu, Y.; Li, G., Polymer solar cells with enhanced open-circuit voltage and efficiency. *Nature Photonics* **2009,** *3* (11), 649-653.
96. Zhao, G.; He, Y.; Li, Y., 6.5% Efficiency of Polymer Solar Cells Based on poly(3-hexylthiophene) and Indene-C60 Bisadduct by Device Optimization. *Advanced Materials* **2010,** *22* (39), 4355-4358.
97. Cheng, Y.-J.; Hsieh, C.-H.; He, Y.; Hsu, C.-S.; Li, Y., Combination of Indene-C60 Bis-Adduct and Cross-Linked Fullerene Interlayer Leading to Highly Efficient Inverted Polymer Solar Cells. *Journal of the American Chemical Society* **2010,** *132* (49), 17381-17383.
98. He, Z.; Zhong, C.; Huang, X.; Wong, W.-Y.; Wu, H.; Chen, L.; Su, S.; Cao, Y., Simultaneous Enhancement of Open-Circuit Voltage, Short-Circuit Current Density, and Fill Factor in Polymer Solar Cells. *Advanced Materials* **2011,** *23* (40), 4636-4643.
99. Jørgensen, M.; Norrman, K.; Krebs, F. C., Stability/degradation of polymer solar cells. *Solar Energy Materials and Solar Cells* **2008,** *92* (7), 686-714.
100. Sun, Y.; Seo, J. H.; Takacs, C. J.; Seifter, J.; Heeger, A. J., Inverted Polymer Solar Cells Integrated with a Low-Temperature-Annealed Sol-Gel-Derived ZnO Film as an Electron Transport Layer. *Advanced Materials* **2011,** *23* (14), 1679-1683.
101. Hau, S. K.; Yip, H.-L.; Leong, K.; Jen, A. K. Y., Spraycoating of silver nanoparticle electrodes for inverted polymer solar cells. *Organic Electronics* **2009,** *10* (4), 719-723.
102. Park, S. H.; Roy, A.; Beaupré, S.; Cho, S.; Coates, N.; Moon, J. S.; Moses, D.; Leclerc, M.; Lee, K.; Heeger, A. J., Bulk heterojunction solar cells with internal quantum efficiency approaching 100%. *Nature Photonics* **2009,** *3* (5), 297-302.
103. Blouin, N.; Michaud, A.; Gendron, D.; Wakim, S.; Blair, E.; Neagu-Plesu, R.; Belletête, M.; Durocher, G.; Tao, Y.; Leclerc, M., Toward a Rational Design of Poly(2,7-Carbazole) Derivatives for Solar Cells. *Journal of the American Chemical Society* **2008,** *130* (2), 732-742.
104. Svensson, M.; Zhang, F.; Veenstra, S. C.; Verhees, W. J. H.; Hummelen, J. C.; Kroon, J. M.; Inganäs, O.; Andersson, M. R., High-Performance Polymer Solar Cells of an Alternating Polyfluorene Copolymer and a Fullerene Derivative. *Advanced Materials* **2003,** *15* (12), 988-991.
105. Cho, S.; Seo, J. H.; Park, S. H.; Beaupré, S.; Leclerc, M.; Heeger, A. J., A Thermally Stable Semiconducting Polymer. *Advanced Materials* **2010,** *22* (11), 1253-1257.
106. Cadogan, J. I. G.; Cameron-Wood, M.; Mackie, R. K.; Searle, R. J. G., 896. The reactivity

of organophosphorus compounds. Part XIX. Reduction of nitro-compounds by triethyl phosphite: a convenient new route to carbazoles, indoles, indazoles, triazoles, and related compounds. *Journal of the Chemical Society (Resumed)* **1965,** (0), 4831-4837.

107. Padhy, H.; Huang, J.-H.; Sahu, D.; Patra, D.; Kekuda, D.; Chu, C.-W.; Lin, H.-C., Synthesis and applications of low-bandgap conjugated polymers containing phenothiazine donor and various benzodiazole acceptors for polymer solar cells. *Journal of Polymer Science Part A: Polymer Chemistry* **2010,** *48* (21), 4823-4834.
108. Sang, G.; Zou, Y.; Li, Y., Two Polythiophene Derivatives Containing Phenothiazine Units: Synthesis and Photovoltaic Properties. *The Journal of Physical Chemistry C* **2008,** *112* (31), 12058-12064.
109. Liu, Y.; Cao, H.; Li, J.; Chen, Z.; Cao, S.; Xiao, L.; Xu, S.; Gong, Q., Synthesis and electroluminescent properties of a phenothiazine-based polymer for nondoped polymer light-emitting diodes with a stable orange-red emission. *Journal of Polymer Science Part A: Polymer Chemistry* **2007,** *45* (21), 4867-4878.
110. Cho, N. S.; Park, J.-H.; Lee, S.-K.; Lee, J.; Shim, H.-K.; Park, M.-J.; Hwang, D.-H.; Jung, B.-J., Saturated and Efficient Red Light-Emitting Fluorene-Based Alternating Polymers Containing Phenothiazine Derivatives. *Macromolecules* **2006,** *39* (1), 177-183.
111. Kong, X.; Kulkarni, A. P.; Jenekhe, S. A., Phenothiazine-Based Conjugated Polymers: Synthesis, Electrochemistry, and Light-Emitting Properties. *Macromolecules* **2003,** *36* (24), 8992-8999.
112. Liu, B.; Najari, A.; Pan, C.; Leclerc, M.; Xiao, D.; Zou, Y., New Low Bandgap Dithienylbenzothiadiazole Vinylene Based Copolymers: Synthesis and Photovoltaic Properties. *Macromolecular Rapid Communications* **2010,** *31* (4), 391-398.
113. Kamtekar, K. T.; Dahms, K.; Batsanov, A. S.; Jankus, V.; Vaughan, H. L.; Monkman, A. P.; Bryce, M. R., Synthesis and characterization of fluorene-based oligomers and polymers incorporating N-arylphenothiazine-S,S-dioxide units. *Journal of Polymer Science Part A: Polymer Chemistry* **2011,** *49* (5), 1129-1137.
114. Scharber, M. C.; Mühlbacher, D.; Koppe, M.; Denk, P.; Waldauf, C.; Heeger, A. J.; Brabec, C. J., Design Rules for Donors in Bulk-Heterojunction Solar Cells—Towards 10 % Energy-Conversion Efficiency. *Advanced Materials* **2006,** *18* (6), 789-794.
115. Brabec, C. J.; Cravino, A.; Meissner, D.; Sariciftci, N. S.; Fromherz, T.; Rispens, M. T.; Sanchez, L.; Hummelen, J. C., Origin of the Open Circuit Voltage of Plastic Solar Cells. *Advanced Functional Materials* **2001,** *11* (5), 374-380.
116. Kang, S.-M.; Leblebici, Y., *CMOS Digital Integrated Circuits Analysis & Design*. McGraw-Hill, Inc.: 2002.
117. Chen, L.-M.; Hong, Z.; Li, G.; Yang, Y., Recent Progress in Polymer Solar Cells:

Manipulation of Polymer:Fullerene Morphology and the Formation of Efficient Inverted Polymer Solar Cells. *Advanced Materials* **2009,** *21* (14-15), 1434-1449.

118. Sun, Y.; Takacs, C. J.; Cowan, S. R.; Seo, J. H.; Gong, X.; Roy, A.; Heeger, A. J., Efficient, Air-Stable Bulk Heterojunction Polymer Solar Cells Using MoOx as the Anode Interfacial Layer. *Advanced Materials* **2011,** *23* (19), 2226-2230.
119. Ma, H.; Yip, H.-L.; Huang, F.; Jen, A. K.-Y., Interface Engineering for Organic Electronics. *Advanced Functional Materials* **2010,** *20* (9), 1371-1388.
120. Zhang, Y.; Hau, S. K.; Yip, H.-L.; Sun, Y.; Acton, O.; Jen, A. K. Y., Efficient Polymer Solar Cells Based on the Copolymers of Benzodithiophene and Thienopyrroledione. *Chemistry of Materials* **2010,** *22* (9), 2696-2698.
121. Hsieh, C.-H.; Cheng, Y.-J.; Li, P.-J.; Chen, C.-H.; Dubosc, M.; Liang, R.-M.; Hsu, C.-S., Highly Efficient and Stable Inverted Polymer Solar Cells Integrated with a Cross-Linked Fullerene Material as an Interlayer. *Journal of the American Chemical Society* **2010,** *132* (13), 4887-4893.
122. Waldauf, C.; Morana, M.; Denk, P.; Schilinsky, P.; Coakley, K.; Choulis, S. A.; Brabec, C. J., Highly efficient inverted organic photovoltaics using solution based titanium oxide as electron selective contact. *Applied Physics Letters* **2006,** *89* (23), 233517.
123. van Duren, J. K. J.; Yang, X.; Loos, J.; Bulle-Lieuwma, C. W. T.; Sieval, A. B.; Hummelen, J. C.; Janssen, R. A. J., Relating the Morphology of Poly(p-phenylene vinylene)/Methanofullerene Blends to Solar-Cell Performance. *Advanced Functional Materials* **2004,** *14* (5), 425-434.
124. Wienk, M. M.; Kroon, J. M.; Verhees, W. J. H.; Knol, J.; Hummelen, J. C.; van Hal, P. A.; Janssen, R. A. J., Efficient Methano[70]fullerene/MDMO-PPV Bulk Heterojunction Photovoltaic Cells. *Angewandte Chemie International Edition* **2003,** *42* (29), 3371-3375.
125. Sariciftci, N. S.; Smilowitz, L.; Heeger, A. J.; Wudl, F., Photoinduced Electron Transfer from a Conducting Polymer to Buckminsterfullerene. *Science* **1992,** *258* (5087), 1474-1476.
126. Li, G.; Shrotriya, V.; Huang, J.; Yao, Y.; Moriarty, T.; Emery, K.; Yang, Y., High-efficiency solution processable polymer photovoltaic cells by self-organization of polymer blends. *Nature Materials* **2005,** *4* (11), 864-868.
127. Ma, W.; Yang, C.; Gong, X.; Lee, K.; Heeger, A. J., Thermally Stable, Efficient Polymer Solar Cells with Nanoscale Control of the Interpenetrating Network Morphology. *Advanced Functional Materials* **2005,** *15* (10), 1617-1622.
128. Peet, J.; Kim, J. Y.; Coates, N. E.; Ma, W. L.; Moses, D.; Heeger, A. J.; Bazan, G. C., Efficiency enhancement in low-bandgap polymer solar cells by processing with alkane dithiols. *Nature Materials* **2007,** *6* (7), 497-500.

129. Coffin, R. C.; Peet, J.; Rogers, J.; Bazan, G. C., Streamlined microwave-assisted preparation of narrow-bandgap conjugated polymers for high-performance bulk heterojunction solar cells. *Nature Chemistry* **2009,** *1* (8), 657-661.

130. Blouin, N.; Michaud, A.; Leclerc, M., A Low-Bandgap Poly(2,7-Carbazole) Derivative for Use in High-Performance Solar Cells. *Advanced Materials* **2007,** *19* (17), 2295-2300.

131. Cho, S.; Seo, J. H.; Park, S. H.; Beaupré, S.; Leclerc, M.; Heeger, A. J., A Thermally Stable Semiconducting Polymer. *Advanced Materials* **2010,** *22* (11), 1253-1257.

132. Park, S. H.; Roy, A.; Beaupré, S.; Cho, S.; Coates, N.; Moon, J. S.; Moses, D.; Leclerc, M.; Lee, K.; Heeger, A. J., Bulk heterojunction solar cells with internal quantum efficiency approaching 100%. *Nature Photonics* **2009,** *3* (5), 297-302.

133. Blouin, N.; Michaud, A.; Gendron, D.; Wakim, S.; Blair, E.; Neagu-Plesu, R.; Belletête, M.; Durocher, G.; Tao, Y.; Leclerc, M., Toward a Rational Design of Poly(2,7-Carbazole) Derivatives for Solar Cells. *Journal of the American Chemical Society* **2008,** *130* (2), 732-742.

134. Alem, S.; Chu, T.-Y.; Tse, S. C.; Wakim, S.; Lu, J.; Movileanu, R.; Tao, Y.; Bélanger, F.; Désilets, D.; Beaupré, S.; Leclerc, M.; Rodman, S.; Waller, D.; Gaudiana, R., Effect of mixed solvents on PCDTBT:PC70BM based solar cells. *Organic Electronics* **2011,** *12* (11), 1788-1793.

135. Moon, J. S.; Jo, J.; Heeger, A. J., Nanomorphology of PCDTBT:PC70BM Bulk Heterojunction Solar Cells. *Advanced Energy Materials* **2012,** *2* (3), 304-308.

136. Cheng, Y.-J.; Wu, J.-S.; Shih, P.-I.; Chang, C.-Y.; Jwo, P.-C.; Kao, W.-S.; Hsu, C.-S., Carbazole-Based Ladder-Type Heptacylic Arene with Aliphatic Side Chains Leading to Enhanced Efficiency of Organic Photovoltaics. *Chemistry of Materials* **2011,** *23* (9), 2361-2369.

137. Wu, J.-S.; Cheng, Y.-J.; Dubosc, M.; Hsieh, C.-H.; Chang, C.-Y.; Hsu, C.-S., Donor–acceptor polymers based on multi-fused heptacyclic structures: synthesis, characterization and photovoltaic applications. *Chemical Communications* **2010,** *46* (19), 3259-3261.

138. Cheedarala, R. K.; Kim, G.-H.; Cho, S.; Lee, J.; Kim, J.; Song, H.-K.; Kim, J. Y.; Yang, C., Ladder-type heteroacene polymers bearing carbazole and thiophene ring units and their use in field-effect transistors and photovoltaic cells. *Journal of Materials Chemistry* **2011,** *21* (3), 843-850.

139. Heeney, M.; Zhang, W.; Crouch, D. J.; Chabinyc, M. L.; Gordeyev, S.; Hamilton, R.; Higgins, S. J.; McCulloch, I.; Skabara, P. J.; Sparrowe, D.; Tierney, S., Regioregular poly(3-hexyl)selenophene: a low band gap organic hole transporting polymer. *Chemical Communications* **2007,** (47), 5061-5063.

140. Patra, A.; Bendikov, M., Polyselenophenes. *Journal of Materials Chemistry* **2010,** *20* (3), 422-433.

141. Yamamoto, N.; Ito, R.; Geerts, Y.; Nomura, K., Synthesis of All-Trans High Molecular Weight Poly(N-alkylcarbazole-2,7-vinylene)s and Poly(9,9-dialkylfluorene-2,7-vinylene)s by Acyclic Diene Metathesis (ADMET) Polymerization Using Ruthenium−Carbene Complex Catalysts. *Macromolecules* **2009,** *42* (14), 5104-5111.

142. Dennler, G.; Scharber, M. C.; Brabec, C. J., Polymer-Fullerene Bulk-Heterojunction Solar Cells. *Advanced Materials* **2009,** *21* (13), 1323-1338.

143. Zade, S. S.; Bendikov, M., From Oligomers to Polymer: Convergence in the HOMO−LUMO Gaps of Conjugated Oligomers. *Organic Letters* **2006,** *8* (23), 5243-5246.

144. Wang, E.; Hou, L.; Wang, Z.; Hellström, S.; Zhang, F.; Inganäs, O.; Andersson, M. R., An Easily Synthesized Blue Polymer for High-Performance Polymer Solar Cells. *Advanced Materials* **2010,** *22* (46), 5240-5244.

145. Wienk, M. M.; Turbiez, M.; Gilot, J.; Janssen, R. A. J., Narrow-Bandgap Diketo-Pyrrolo-Pyrrole Polymer Solar Cells: The Effect of Processing on the Performance. *Advanced Materials* **2008,** *20* (13), 2556-2560.

146. Kronemeijer, A. J.; Gili, E.; Shahid, M.; Rivnay, J.; Salleo, A.; Heeney, M.; Sirringhaus, H., A Selenophene-Based Low-Bandgap Donor–Acceptor Polymer Leading to Fast Ambipolar Logic. *Advanced Materials* **2012,** *24* (12), 1558-1565.

147. Shahid, M.; McCarthy-Ward, T.; Labram, J.; Rossbauer, S.; Domingo, E. B.; Watkins, S. E.; Stingelin, N.; Anthopoulos, T. D.; Heeney, M., Low band gap selenophene–diketopyrrolopyrrole polymers exhibiting high and balanced ambipolar performance in bottom-gate transistors. *Chemical Science* **2012,** *3* (1), 181-185.

148. Chattopadhyaya, M.; Sen, S.; Alam, M. M.; Chakrabarti, S., The role of relativity and dispersion controlled inter-chain interaction on the band gap of thiophene, selenophene, and tellurophene oligomers. *The Journal of Chemical Physics* **2012,** *136* (9), 094904.

149. Patra, A.; Wijsboom, Y. H.; Leitus, G.; Bendikov, M., Tuning the Band Gap of Low-Band-Gap Polyselenophenes and Polythiophenes: The Effect of the Heteroatom. *Chemistry of Materials* **2011,** *23* (3), 896-906.

150. Zade, S. S.; Zamoshchik, N.; Bendikov, M., From Short Conjugated Oligomers to Conjugated Polymers. Lessons from Studies on Long Conjugated Oligomers. *Accounts of Chemical Research* **2011,** *44* (1), 14-24.

151. Scharber, M. C.; Mühlbacher, D.; Koppe, M.; Denk, P.; Waldauf, C.; Heeger, A. J.; Brabec, C. J., Design Rules for Donors in Bulk-Heterojunction Solar Cells—Towards 10 % Energy-Conversion Efficiency. *Advanced Materials* **2006,** *18* (6), 789-794.

152. Li, J.; Grimsdale, A. C., Carbazole-based polymers for organic photovoltaic devices. *Chemical*

Society Reviews **2010,** *39* (7), 2399-2410.

153. Chu, T.-Y.; Alem, S.; Tsang, S.-W.; Tse, S.-C.; Wakim, S.; Lu, J.; Dennler, G.; Waller, D.; Gaudiana, R.; Tao, Y., Morphology control in polycarbazole based bulk heterojunction solar cells and its impact on device performance. *Applied Physics Letters* **2011,** *98* (25), 253301.
154. Saadeh, H. A.; Lu, L.; He, F.; Bullock, J. E.; Wang, W.; Carsten, B.; Yu, L., Polyselenopheno[3,4-b]selenophene for Highly Efficient Bulk Heterojunction Solar Cells. *ACS Macro Letters* **2012,** *1* (3), 361-365.
155. Erb, T.; Zhokhavets, U.; Gobsch, G.; Raleva, S.; Stühn, B.; Schilinsky, P.; Waldauf, C.; Brabec, C. J., Correlation Between Structural and Optical Properties of Composite Polymer/Fullerene Films for Organic Solar Cells. *Advanced Functional Materials* **2005,** *15* (7), 1193-1196.
156. Dennler, G.; Scharber, M. C.; Brabec, C. J., Polymer-Fullerene Bulk-Heterojunction Solar Cells. *Advanced Materials* **2009,** *21* (13), 1323-1338.
157. Kim, Y.; Yeom, H. R.; Kim, J. Y.; Yang, C., High-efficiency polymer solar cells with a cost-effective quinoxaline polymer through nanoscale morphology control induced by practical processing additives. *Energy & Environmental Science* **2013,** *6* (6), 1909-1916.
158. Kaltenbrunner, M.; White, M. S.; Głowacki, E. D.; Sekitani, T.; Someya, T.; Sariciftci, N. S.; Bauer, S., Ultrathin and lightweight organic solar cells with high flexibility. *Nature Communications* **2012,** *3* (1), 770.
159. Park, S. H.; Roy, A.; Beaupré, S.; Cho, S.; Coates, N.; Moon, J. S.; Moses, D.; Leclerc, M.; Lee, K.; Heeger, A. J., Bulk heterojunction solar cells with internal quantum efficiency approaching 100%. *Nature Photonics* **2009,** *3* (5), 297-302.
160. Yu, G.; Gao, J.; Hummelen, J. C.; Wudl, F.; Heeger, A. J., Polymer Photovoltaic Cells: Enhanced Efficiencies via a Network of Internal Donor-Acceptor Heterojunctions. *Science* **1995,** *270* (5243), 1789-1791.
161. Service, R. F., Outlook Brightens for Plastic Solar Cells. *Science* **2011,** *332* (6027), 293-293.
162. Sun, Y.; Seo, J. H.; Takacs, C. J.; Seifter, J.; Heeger, A. J., Inverted Polymer Solar Cells Integrated with a Low-Temperature-Annealed Sol-Gel-Derived ZnO Film as an Electron Transport Layer. *Advanced Materials* **2011,** *23* (14), 1679-1683.
163. Norrman, K.; Madsen, M. V.; Gevorgyan, S. A.; Krebs, F. C., Degradation Patterns in Water and Oxygen of an Inverted Polymer Solar Cell. *Journal of the American Chemical Society* **2010,** *132* (47), 16883-16892.
164. Li, G.; Chu, C.-W.; Shrotriya, V.; Huang, J.; Yang, Y., Efficient inverted polymer solar cells. *Applied Physics Letters* **2006,** *88* (25), 253503.
165. Tao, C.; Ruan, S.; Zhang, X.; Xie, G.; Shen, L.; Kong, X.; Dong, W.; Liu, C.;

Chen, W., Performance improvement of inverted polymer solar cells with different top electrodes by introducing a MoO3 buffer layer. *Applied Physics Letters* **2008,** *93* (19), 193307.

166. Waldauf, C.; Morana, M.; Denk, P.; Schilinsky, P.; Coakley, K.; Choulis, S. A.; Brabec, C. J., Highly efficient inverted organic photovoltaics using solution based titanium oxide as electron selective contact. *Applied Physics Letters* **2006,** *89* (23), 233517.
167. Choi, H.; Park, J. S.; Jeong, E.; Kim, G.-H.; Lee, B. R.; Kim, S. O.; Song, M. H.; Woo, H. Y.; Kim, J. Y., Combination of Titanium Oxide and a Conjugated Polyelectrolyte for High-Performance Inverted-Type Organic Optoelectronic Devices. *Advanced Materials* **2011,** *23* (24), 2759-2763.
168. Chang, Y.-M.; Leu, C.-Y., Conjugated polyelectrolyte and zinc oxide stacked structure as an interlayer in highly efficient and stable organic photovoltaic cells. *Journal of Materials Chemistry A* **2013,** *1* (21), 6446-6451.
169. Seo, J. H.; Gutacker, A.; Sun, Y.; Wu, H.; Huang, F.; Cao, Y.; Scherf, U.; Heeger, A. J.; Bazan, G. C., Improved High-Efficiency Organic Solar Cells via Incorporation of a Conjugated Polyelectrolyte Interlayer. *Journal of the American Chemical Society* **2011,** *133* (22), 8416-8419.
170. Yang, H.; Zhu, S.; Pan, N., Studying the mechanisms of titanium dioxide as ultraviolet-blocking additive for films and fabrics by an improved scheme. *Journal of Applied Polymer Science* **2004,** *92* (5), 3201-3210.
171. Kyaw, A. K. K.; Wang, D. H.; Gupta, V.; Zhang, J.; Chand, S.; Bazan, G. C.; Heeger, A. J., Efficient Solution-Processed Small-Molecule Solar Cells with Inverted Structure. *Advanced Materials* **2013,** *25* (17), 2397-2402.
172. He, Z.; Zhong, C.; Su, S.; Xu, M.; Wu, H.; Cao, Y., Enhanced power-conversion efficiency in polymer solar cells using an inverted device structure. *Nature Photonics* **2012,** *6* (9), 591-595.
173. Zhou, Y.; Fuentes-Hernandez, C.; Shim, J.; Meyer, J.; Giordano, A. J.; Li, H.; Winget, P.; Papadopoulos, T.; Cheun, H.; Kim, J.; Fenoll, M.; Dindar, A.; Haske, W.; Najafabadi, E.; Khan, T. M.; Sojoudi, H.; Barlow, S.; Graham, S.; Brédas, J.-L.; Marder, S. R.; Kahn, A.; Kippelen, B., A Universal Method to Produce Low–Work Function Electrodes for Organic Electronics. *Science* **2012,** *336* (6079), 327-332.
174. Beek, W. J. E.; Slooff, L. H.; Wienk, M. M.; Kroon, J. M.; Janssen, R. A. J., Hybrid Solar Cells Using a Zinc Oxide Precursor and a Conjugated Polymer. *Advanced Functional Materials* **2005,** *15* (10), 1703-1707.
175. Seo, J. H.; Yang, R.; Brzezinski, J. Z.; Walker, B.; Bazan, G. C.; Nguyen, T.-Q., Electronic Properties at Gold/Conjugated-Polyelectrolyte Interfaces. *Advanced Materials* **2009,** *21* (9), 1006-1011.

176. You, J.; Li, X.; Xie, F.-x.; Sha, W. E. I.; Kwong, J. H. W.; Li, G.; Choy, W. C. H.; Yang, Y., Surface Plasmon and Scattering-Enhanced Low-Bandgap Polymer Solar Cell by a Metal Grating Back Electrode. *Advanced Energy Materials* **2012,** *2* (10), 1203-1207.

177. Hedley, G. J.; Ward, A. J.; Alekseev, A.; Howells, C. T.; Martins, E. R.; Serrano, L. A.; Cooke, G.; Ruseckas, A.; Samuel, I. D. W., Determining the optimum morphology in high-performance polymer-fullerene organic photovoltaic cells. *Nature Communications* **2013,** *4* (1), 2867.

178. Kaune, G.; Ruderer, M. A.; Metwalli, E.; Wang, W.; Couet, S.; Schlage, K.; Röhlsberger, R.; Roth, S. V.; Müller-Buschbaum, P., In Situ GISAXS Study of Gold Film Growth on Conducting Polymer Films. *ACS Applied Materials & Interfaces* **2009,** *1* (2), 353-360.

179. Santoro, G.; Yu, S.; Schwartzkopf, M.; Zhang, P.; Vayalil, S. K.; Risch, J. F. H.; Rübhausen, M. A.; Hernández, M.; Domingo, C.; Roth, S. V., Silver substrates for surface enhanced Raman scattering: Correlation between nanostructure and Raman scattering enhancement. *Applied Physics Letters* **2014,** *104* (24), 243107.

180. Hollars, C. W.; Dunn, R. C., Evaluation of thermal evaporation conditions used in coating aluminum on near-field fiber-optic probes. *Review of Scientific Instruments* **1998,** *69* (4), 1747-1752.

181. Uda, M.; Nakamura, A.; Yamamoto, T.; Fujimoto, Y., Work function of polycrystalline Ag, Au and Al. *Journal of Electron Spectroscopy and Related Phenomena* **1998,** *88-91*, 643-648.

182. Chen, L.-M.; Hong, Z.; Li, G.; Yang, Y., Recent Progress in Polymer Solar Cells: Manipulation of Polymer:Fullerene Morphology and the Formation of Efficient Inverted Polymer Solar Cells. *Advanced Materials* **2009,** *21* (14-15), 1434-1449.

183. Seo, J. H.; Kim, H.; Cho, S., Build-up of symmetry breaking using a titanium suboxide in bulk-heterojunction solar cells. *Physical Chemistry Chemical Physics* **2012,** *14* (12), 4062-4065.

184. Meier, D. L.; Schroder, D. K., Contact resistance: Its measurement and relative importance to power loss in a solar cell. *IEEE Transactions on Electron Devices* **1984,** *31* (5), 647-653.

185. Proctor, C. M.; Kuik, M.; Nguyen, T.-Q., Charge carrier recombination in organic solar cells. *Progress in Polymer Science* **2013,** *38* (12), 1941-1960.

186. Umbrajkar, S. M.; Schoenitz, M.; Dreizin, E. L., Control of Structural Refinement and Composition in Al-MoO3 Nanocomposites Prepared by Arrested Reactive Milling. *Propellants, Explosives, Pyrotechnics* **2006,** *31* (5), 382-389.

187. Burkhard, G. F.; Hoke, E. T.; McGehee, M. D., Accounting for Interference, Scattering, and Electrode Absorption to Make Accurate Internal Quantum Efficiency Measurements in Organic and Other Thin Solar Cells. *Advanced Materials* **2010,** *22* (30), 3293-3297.

188. Pettersson, L. A. A.; Roman, L. S.; Inganäs, O., Modeling photocurrent action spectra of photovoltaic devices based on organic thin films. *Journal of Applied Physics* **1999,** *86* (1), 487-496.

189. Peumans, P.; Yakimov, A.; Forrest, S. R., Small molecular weight organic thin-film photodetectors and solar cells. *Journal of Applied Physics* **2003,** *93* (7), 3693-3723.

190. Kim, J.; Kang, J.; Jeong, U.; Kim, H.; Lee, H., Catalytic, Conductive, and Transparent Platinum Nanofiber Webs for FTO-Free Dye-Sensitized Solar Cells. *ACS Applied Materials & Interfaces* **2013,** *5* (8), 3176-3181.

191. Hsu, P.-C.; Kong, D.; Wang, S.; Wang, H.; Welch, A. J.; Wu, H.; Cui, Y., Electrolessly Deposited Electrospun Metal Nanowire Transparent Electrodes. *Journal of the American Chemical Society* **2014,** *136* (30), 10593-10596.

192. Ishii, T.; Masuda, A., Annual degradation rates of recent crystalline silicon photovoltaic modules. *Progress in Photovoltaics: Research and Applications* **2017,** *25* (12), 953-967.

193. Yim, J. H.; Joe, S.-y.; Pang, C.; Lee, K. M.; Jeong, H.; Park, J.-Y.; Ahn, Y. H.; de Mello, J. C.; Lee, S., Fully Solution-Processed Semitransparent Organic Solar Cells with a Silver Nanowire Cathode and a Conducting Polymer Anode. *ACS Nano* **2014,** *8* (3), 2857-2863.

194. Krebs, F. C., Fabrication and processing of polymer solar cells: A review of printing and coating techniques. *Solar Energy Materials and Solar Cells* **2009,** *93* (4), 394-412.

195. Yu, G.; Gao, J.; Hummelen, J. C.; Wudl, F.; Heeger, A. J., Polymer Photovoltaic Cells: Enhanced Efficiencies via a Network of Internal Donor-Acceptor Heterojunctions. *Science* **1995,** *270* (5243), 1789.

196. Günes, S.; Neugebauer, H.; Sariciftci, N. S., Conjugated Polymer-Based Organic Solar Cells. *Chemical Reviews* **2007,** *107* (4), 1324-1338.

197. Kim, J. Y.; Lee, K.; Coates, N. E.; Moses, D.; Nguyen, T.-Q.; Dante, M.; Heeger, A. J., Efficient Tandem Polymer Solar Cells Fabricated by All-Solution Processing. *Science* **2007,** *317* (5835), 222.

198. Chen, J.; Cao, Y., Development of Novel Conjugated Donor Polymers for High-Efficiency Bulk-Heterojunction Photovoltaic Devices. *Accounts of Chemical Research* **2009,** *42* (11), 1709-1718.

199. Dennler, G.; Scharber, M. C.; Brabec, C. J., Polymer-Fullerene Bulk-Heterojunction Solar Cells. *Advanced Materials* **2009,** *21* (13), 1323-1338.

200. Søndergaard, R.; Hösel, M.; Angmo, D.; Larsen-Olsen, T. T.; Krebs, F. C., Roll-to-roll fabrication of polymer solar cells. *Materials Today* **2012,** *15* (1), 36-49.

201. Darling, S. B.; You, F., The case for organic photovoltaics. *RSC Advances* **2013,** *3* (39), 17633-17648.

202. Ko, J.; Song, J.; Choi, W. T.; Kim, T.-H.; Han, Y.-S.; Lim, J.; Lee, C.; Char, K., Significance of Polymeric Nanowire-Network Structures for Stable and Efficient Organic Solar Cells. *Macromolecular Research* **2018,** *26* (7), 623-629.

203. Meng, L.; Zhang, Y.; Wan, X.; Li, C.; Zhang, X.; Wang, Y.; Ke, X.; Xiao, Z.; Ding, L.; Xia, R.; Yip, H.-L.; Cao, Y.; Chen, Y., Organic and solution-processed tandem solar cells with 17.3% efficiency. *Science* **2018,** *361* (6407), 1094.

204. Bailey-Salzman, R. F.; Rand, B. P.; Forrest, S. R.; P., P.; A., Y.; R., F. S., Semitransparent organic photovoltaic cells. *Applied Physics Letters* **2006,** *88* (23), 233502.

205. Huang, J.; Li, G.; Yang, Y., A Semi-transparent Plastic Solar Cell Fabricated by a Lamination Process. *Advanced Materials* **2008,** *20* (3), 415-419.

206. Koeppe, R.; Hoeglinger, D.; Troshin, P. A.; Lyubovskaya, R. N.; Razumov, V. F.; Sariciftci, N. S., Organic Solar Cells with Semitransparent Metal Back Contacts for Power Window Applications. *ChemSusChem* **2009,** *2* (4), 309-313.

207. Ameri, T.; Dennler, G.; Waldauf, C.; Azimi, H.; Seemann, A.; Forberich, K.; Hauch, J.; Scharber, M.; Hingerl, K.; Brabec, C. J., Fabrication, Optical Modeling, and Color Characterization of Semitransparent Bulk-Heterojunction Organic Solar Cells in an Inverted Structure. *Advanced Functional Materials* **2010,** *20* (10), 1592-1598.

208. Lee, Y.-Y.; Tu, K.-H.; Yu, C.-C.; Li, S.-S.; Hwang, J.-Y.; Lin, C.-C.; Chen, K.-H.; Chen, L.-C.; Chen, H.-L.; Chen, C.-W., Top Laminated Graphene Electrode in a Semitransparent Polymer Solar Cell by Simultaneous Thermal Annealing/Releasing Method. *ACS Nano* **2011,** *5* (8), 6564-6570.

209. Sergeant, N. P.; Hadipour, A.; Niesen, B.; Cheyns, D.; Heremans, P.; Peumans, P.; Rand, B. P., Design of Transparent Anodes for Resonant Cavity Enhanced Light Harvesting in Organic Solar Cells. *Advanced Materials* **2012,** *24* (6), 728-732.

210. Chen, C.-C.; Dou, L.; Gao, J.; Chang, W.-H.; Li, G.; Yang, Y., High-performance semi-transparent polymer solar cells possessing tandem structures. *Energy & Environmental Science* **2013,** *6* (9), 2714-2720.

211. Tai, Q.; Yan, F., Emerging Semitransparent Solar Cells: Materials and Device Design. *Advanced Materials* **2017,** *29* (34), 1700192.

212. Chang, S.-Y.; Cheng, P.; Li, G.; Yang, Y., Transparent Polymer Photovoltaics for Solar Energy Harvesting and Beyond. *Joule* **2018,** *2* (6), 1039-1054.

213. Xue, Q.; Xia, R.; Brabec, C. J.; Yip, H.-L., Recent advances in semi-transparent polymer and perovskite solar cells for power generating window applications. *Energy & Environmental Science* **2018,** *11* (7), 1688-1709.

214. Xia, R.; Brabec, C. J.; Yip, H.-L.; Cao, Y., High-Throughput Optical Screening for Efficient Semitransparent Organic Solar Cells. *Joule* **2019,** *3* (9), 2241-2254.

215. Nguyen, T. L.; Song, S.; Ko, S.-J.; Choi, H.; Jeong, J.-E.; Kim, T.; Hwang, S.; Kim, J. Y.; Woo, H. Y., Benzodithiophene-thiophene-based photovoltaic polymers with different side-chains. *Journal of Polymer Science Part A: Polymer Chemistry* **2015,** *53* (7), 854-862.

216. Hong, L.; Yao, H.; Wu, Z.; Cui, Y.; Zhang, T.; Xu, Y.; Yu, R.; Liao, Q.; Gao, B.; Xian, K.; Woo, H. Y.; Ge, Z.; Hou, J., Eco-Compatible Solvent-Processed Organic Photovoltaic Cells with Over 16% Efficiency. *Advanced Materials* **2019,** *31* (39), 1903441.

217. Cui, Y.; Yang, C.; Yao, H.; Zhu, J.; Wang, Y.; Jia, G.; Gao, F.; Hou, J., Efficient Semitransparent Organic Solar Cells with Tunable Color enabled by an Ultralow-Bandgap Nonfullerene Acceptor. *Advanced Materials* **2017,** *29* (43), 1703080.

218. Bi, Y.-G.; Liu, Y.-F.; Zhang, X.-L.; Yin, D.; Wang, W.-Q.; Feng, J.; Sun, H.-B., Ultrathin Metal Films as the Transparent Electrode in ITO-Free Organic Optoelectronic Devices. *Advanced Optical Materials* **2019,** *7* (6), 1800778.

219. Su, W.; Fan, Q.; Guo, X.; Wu, J.; Zhang, M.; Li, Y., Efficient as-cast semi-transparent organic solar cells with efficiency over 9% and a high average visible transmittance of 27.6%. *Physical Chemistry Chemical Physics* **2019,** *21* (20), 10660-10666.

220. Upama, M. B.; Wright, M.; Elumalai, N. K.; Mahmud, M. A.; Wang, D.; Xu, C.; Uddin, A., High-Efficiency Semitransparent Organic Solar Cells with Non-Fullerene Acceptor for Window Application. *ACS Photonics* **2017,** *4* (9), 2327-2334.

221. Sun, G.; Shahid, M.; Fei, Z.; Xu, S.; Eisner, F. D.; Anthopolous, T. D.; McLachlan, M. A.; Heeney, M., Highly-efficient semi-transparent organic solar cells utilising non-fullerene acceptors with optimised multilayer MoO3/Ag/MoO3 electrodes. *Materials Chemistry Frontiers* **2019,** *3* (3), 450-455.

222. Lee, J. Y.; Lee, K.-T.; Seo, S.; Guo, L. J., Decorative power generating panels creating angle insensitive transmissive colors. *Scientific Reports* **2014,** *4*, 4192.

223. Li, Z.; Butun, S.; Aydin, K., Large-Area, Lithography-Free Super Absorbers and Color Filters at Visible Frequencies Using Ultrathin Metallic Films. *ACS Photonics* **2015,** *2* (2), 183-188.

224. Zhong, J.; Xiao, Z.; Liang, W.; Wu, Y.; Ye, Q.; Xu, H.; Deng, H.; Shen, L.; Feng, X.; Long, Y., Highly Efficient and High Peak Transmittance Colorful Semitransparent Organic Solar Cells with Hybrid-Electrode-Mirror Microcavity Structure. *ACS Applied Materials & Interfaces* **2019,** *11* (51), 47992-48001.

225. Lee, K.-T.; Fukuda, M.; Joglekar, S.; Guo, L. J., Colored, see-through perovskite solar cells employing an optical cavity. *Journal of Materials Chemistry C* **2015,** *3* (21), 5377-5382.

226. Kim, Y.; Son, J.; Shafian, S.; Kim, K.; Hyun, J. K., Semitransparent Blue, Green, and Red Organic Solar Cells Using Color Filtering Electrodes. *Advanced Optical Materials* **2018,**

6 (13), 1800051.

227. Lu, J.-H.; Lin, Y.-H.; Jiang, B.-H.; Yeh, C.-H.; Kao, J.-C.; Chen, C.-P., Microcavity Structure Provides High-Performance (>8.1%) Semitransparent and Colorful Organic Photovoltaics. *Advanced Functional Materials* **2018,** *28* (7), 1703398.
228. Yang, C.; Liu, D.; Bates, M.; Barr, M. C.; Lunt, R. R., How to Accurately Report Transparent Solar Cells. *Joule* **2019,** *3* (8), 1803-1809.
229. Zorabedian, P., 8 - Tunable External-Cavity Semiconductor Lasers. In *Tunable Lasers Handbook*, Duarte, F. J., Ed. Academic Press: San Diego, 1995; pp 349-442.
1. 230 Weir, H.; Edel, J. B.; Kornyshev, A. A.; Sikdar, D., Towards Electrotuneable Nanoplasmonic Fabry–Perot Interferometer. *Scientific Reports* **2018,** *8* (1), 565.
230. Campbell, C. T., Ultrathin metal films and particles on oxide surfaces: structural, electronic and chemisorptive properties. *Surface Science Reports* **1997,** *27* (1), 1-111.
231. Xu, G.; Shen, L.; Cui, C.; Wen, S.; Xue, R.; Chen, W.; Chen, H.; Zhang, J.; Li, H.; Li, Y.; Li, Y., High-Performance Colorful Semitransparent Polymer Solar Cells with Ultrathin Hybrid-Metal Electrodes and Fine-Tuned Dielectric Mirrors. *Advanced Functional Materials* **2017,** *27* (15), 1605908.
232. Yeom, H. R.; Heo, J.; Kim, G.-H.; Ko, S.-J.; Song, S.; Jo, Y.; Kim, D. S.; Walker, B.; Kim, J. Y., Optimal top electrodes for inverted polymer solar cells. *Physical Chemistry Chemical Physics* **2015,** *17* (3), 2152-2159.
233. Bae, S.; Kim, H.; Lee, Y.; Xu, X.; Park, J.-S.; Zheng, Y.; Balakrishnan, J.; Lei, T.; Ri Kim, H.; Song, Y. I.; Kim, Y.-J.; Kim, K. S.; Özyilmaz, B.; Ahn, J.-H.; Hong, B. H.; Iijima, S., Roll-to-roll production of 30-inch graphene films for transparent electrodes. *Nature Nanotechnology* **2010,** *5* (8), 574-578.
234. Kang, S.; Kim, T.; Cho, S.; Lee, Y.; Choe, A.; Walker, B.; Ko, S.-J.; Kim, J. Y.; Ko, H., Capillary Printing of Highly Aligned Silver Nanowire Transparent Electrodes for High-Performance Optoelectronic Devices. *Nano Letters* **2015,** *15* (12), 7933-7942.
235. Cho, K.-S.; Kim, E.; Kim, D.-W.; Kim, H.-K., Highly flexible and semi-transparent Ag–Cu alloy electrodes for high performance flexible thin film heaters. *RSC Advances* **2017,** *7* (72), 45484-45494.
236. Liu, Z.; Li, J.; Sun, Z.-H.; Tai, G.; Lau, S.-P.; Yan, F., The Application of Highly Doped Single-Layer Graphene as the Top Electrodes of Semitransparent Organic Solar Cells. *ACS Nano* **2012,** *6* (1), 810-818.
237. Liu, Z.; You, P.; Liu, S.; Yan, F., Neutral-Color Semitransparent Organic Solar Cells with All-Graphene Electrodes. *ACS Nano* **2015,** *9* (12), 12026-12034.
238. You, P.; Liu, Z.; Tai, Q.; Liu, S.; Yan, F., Efficient Semitransparent Perovskite Solar Cells with Graphene Electrodes. *Advanced Materials* **2015,** *27* (24), 3632-3638.

239. Pettersson, L. A. A.; Roman, L. S.; Inganäs, O., Modeling photocurrent action spectra of photovoltaic devices based on organic thin films. *Journal of Applied Physics* **1999,** *86* (1), 487-496.

240. Kyaw, A. K. K.; Wang, D. H.; Gupta, V.; Leong, W. L.; Ke, L.; Bazan, G. C.; Heeger, A. J., Intensity Dependence of Current–Voltage Characteristics and Recombination in High-Efficiency Solution-Processed Small-Molecule Solar Cells. *ACS Nano* **2013,** *7* (5), 4569-4577.

241. Li, Y.; Ko, S.-J.; Park, S. Y.; Choi, H.; Nguyen, T. L.; Uddin, M. A.; Kim, T.; Hwang, S.; Kim, J. Y.; Woo, H. Y., Quinoxaline–thiophene based thick photovoltaic devices with an efficiency of ~8%. *Journal of Materials Chemistry A* **2016,** *4* (25), 9967-9976.

242. Shafian, S.; Son, J.; Kim, Y.; Hyun, J. K.; Kim, K., Active-Material-Independent Color-Tunable Semitransparent Organic Solar Cells. *ACS Applied Materials & Interfaces* **2019,** *11* (21), 18887-18895.

243. Pan, M.-A.; Lau, T.-K.; Tang, Y.; Wu, Y.-C.; Liu, T.; Li, K.; Chen, M.-C.; Lu, X.; Ma, W.; Zhan, C., 16.7%-efficiency ternary blended organic photovoltaic cells with PCBM as the acceptor additive to increase the open-circuit voltage and phase purity. *Journal of Materials Chemistry A* **2019,** *7* (36), 20713-20722.

244. Wang, W.; Zhao, B.; Cong, Z.; Xie, Y.; Wu, H.; Liang, Q.; Liu, S.; Liu, F.; Gao, C.; Wu, H.; Cao, Y., Nonfullerene Polymer Solar Cells Based on a Main-Chain Twisted Low-Bandgap Acceptor with Power Conversion Efficiency of 13.2%. *ACS Energy Letters* **2018,** *3* (7), 1499-1507.

245. Xiao, Z.; Jia, X.; Ding, L., Ternary organic solar cells offer 14% power conversion efficiency. *Science Bulletin* **2017,** *62* (23), 1562-1564.

246. Reproduced in part with permission from Kim, Y.; Yeom, H.; Kim, J. Y.; Yang, C., High-efficiency polymer solar cells with a cost-effective quinoxaline polymer through nanoscale morphology control induced by practical processing additives. *Energy Environ. Sci.* **2013,** *6*, 1909-1916.

247. Reproduced in part with permission from Kim, G.; Yeom, H.; Cho, S.; Seo, J.; Kim, J.; Yang, C., Easily Attainable Phenothiazine-Based Polymers for Polymer Solar Cells: Advantage of Insertion ofS,S-dioxides into its Polymer for Inverted Structure Solar Cells. *Macromolecules* **2012,** *45*, 1847-1857.

248. Reproduced in part with permission from Kim, B.; Yeom, H.; Yun, M.; Kim, J.; Yang, C., A Selenophene Analogue of PCDTBT: Selective Fine-Tuning of LUMO to Lower of the Bandgap for Efficient Polymer Solar Cells. *Macromolecules* **2012,** *45*, 8658-8664.

249. Reproduced in part with permission from Yeom, H.; Heo, J.; Kim, G.; Ko, S.-J.; Song, S.; Jo, Y.; Kim, D.; Walker, B.; Kim, J., Optimal top electrodes for inverted polymer solar

cells. *Physical chemistry chemical physics : PCCP* **2014,** *17*.

Acknowledgements

The fear of the Load is the beginning of the knowledge. (Provebs 1:7)

2011년 1월 NGEL의 멤버가 되어 어느덧 10년이 지났네요, 그 누구보다 긴 시간을 NGEL과 함께 했기에 감사할 사람이 많아 긴 감사의 글이 될 것 같습니다 ^^

먼저는 기나긴 석. 박 과정을 끝까지 포기하지 않고 마칠 수 있도록 기다려 주시고, 지지해주신 지도교수님 김진영교수님께 감사의 말씀을 드립니다. 저는 UNIST에 들어와서 인륜지대사를 모두 치른 듯합니다^^; 그 모든 시간 가운데, 교수님의 위로와 격려가 없었더라면, 저는 진작에 학위를 포기했을 것 같습니다. 육아와 학위를 동시에 하는 것이 너무나 버거워서 몇 번 이나 학위를 포기하려 할 때 마다, “지금 포기하면 나중에 정말 후회할꺼야,,, 그냥 차라리 휴학을 해서 조금 쉬고 다시 시작해보자.” 하며 붙잡아 주셨고, 스스로 너무 부족하다 느껴져 포기하고 싶을 때면, “대학원 생활은 버티는 거야, 잘하는 놈보다 끝까지 버티는 놈이 박사학위 받는 거야. 끝까지 버텨라. 버티기 위해선 건강해야해. 건강 잘 챙기고!” 해 주셨던 말씀들이 저를 버틸 수 있게 해주었던 것 같습니다. 지난시간, 많은 배움들이 있었지만, 한가지를 꼽자면, 다른 사람을 포용해주고 기다려주는 것이 누군가에겐 인생에 큰 기회를 주게 되는, 결코 작지 않은 일이 될 수 있다는 걸 배우게 됩니다. 교수님, 정말 감사합니다. 교수님은 정말 좋은 분 이세요….*^^*

다음으로는 기꺼이 졸업논문 심사위원으로 응해 주신 송명훈교수님, 권태혁교수님, 서정화교수님, 김동석센터장님 진심으로 감사드립니다. “아줌마가 학위 한다고 고생 많다”며 다들 따뜻한 응원과 격려해주시고, 귀한 조언들 해주신 덕분에 지난 긴 학위 과정의 연구들을 잘 정리할 수 있었고, 졸업논문을 완성할 수 있었습니다. 특히 긴 시간 내주셔서 인생상담까지 해 주셨던 권태혁 교수님, 교수님께서 해 주셨던 조언들은 제 삶에 두고두고 귀한 양분이 될 것입니다. 연구에 아직 감도 없던 1학년때 논문을 쓸 수 있는 연구가 무엇인지를 알려주셨던 양창덕교수님, 학위 마지막 공동연구를 통해 논문을 잘 쓰는 방법들을 가르쳐 주신 우한영교수님, 수아를 임신했을 때 혹여나 제가 학위를 포기하진 않을까…염려하시며, 부부 박사의 결혼과 육아를 경험하셨기에 어려움을 이미 알고 진심 어린 조언들을 해 주셨던 송현곤교수님, 지금은 UNIST에 계시지 않지만, 임현오빠의 지도교수님으로 저희 부부를 많이 아껴 주셨던 전용석 교수님, 화학과 물리를 넘나들며 어떠한 질문에도 늘 친절히 쉽게 풀어 가르쳐 주셨던 NGEL의 천사 Bright 교수님. It was a great blessing for NGEL members to meet Professor Bright at NGEL and see and learn from you :) 여성 과학자로 학위 중간중간 많은 조언을 해 주셨던 서정화교수님, 송수희박사님께도 감사한 마음을 전해드리고 싶습니다. UNIST에 와서 정말 좋은 과학자(교수님, 박사님)분들 많이 만날 수 있었던 건 제 인생에 큰 축복이었습니다. 다시 한번 귀한 가르침들에 깊은 감사를 드립니다.

지난 10년간 제가 가장 마음을 많이 나누고 애정했던 우리 NGEL 식구들에게도 감사의 마음을

전하고 싶습니다. 오랜시간 NGEL의 현역으로 있었던 만큼 감사해야 할 사람들이 참 많네요. 위에서부터 내려갈께요~~ㅋ 먼저 우리 NGEL의 맏형 기환이행님^^ 오빠 진짜 고마워요~ 처음 1학년땐 호랑이같이 무서웠던 오빠 덕분에 눈물 쏙 빼며 배웠던 기억이 큰데, 제가 선배가 되고 나니 오빠의 깊은 뜻을 많이 깨닫네요. 오빠가 NGEL을 얼마나 아끼고 있고 후배들을 잘 끌어주고 싶은 마음에서 했던 수고들이었단 걸 선배가 되어보고 나니 가슴깊이 느끼고 더 더 감사하게되요. 글고 무엇보다… 임현오빠와 저의 오작교가 되어주신 오빠의 은혜는 평생 잊지 않을께요^^ 오빠 안목짱~!!ㅋㅋㅋ 늘~오빠한테 감사해 하라는 오빠말 ㅋㅋㅋ 우끼긴 하지만…진짜 진심으로 그렇게 생각하고 있어요. 오빠 많이 고마워요. 다음으론 저의 Angel of NGEL 명희언니^^ 언니 덕분에 이렇게 좋은랩에 컨텍하게 되고 처음부터 지금까지 끌어주고 때때마다 힘이 되어주셔서 정말 고마워요. 가만히 돌아보면 정말 힘들때나, 기쁠때나, 언니가 항상 제게 힘이 되어주고 많이 응원해준 덕분에 지금까지 잘 버틸 수 있었어요. 언니가 틈틈히 제 책상위에 올려두었던 응원의 쪽지들은 지금도 모아두고 한번씩 꺼내봐요♡ 우리 랩 맏언니로 여학생들에게 귀감이 되어 주셔서 정말 감사해요. 다음으로 NGEL의 전설 같은 선배 효성오빠, 대학원 생활에 시간을 어떻게 가장 효율적으로 쓸 수 있는지 정석을 보여주셔서 많이 배웠습니다 감사해요^^. NGEL의 성실의 아이콘 서진오빠, 1학년땐 오빠가 참 어려운 선배였는데, 시간이 지날수록 누구보다 오빠에게 정이 많이 쌓여가네요^^ 오빠를 보며 성실과 가족을 생각하는 따뜻한 마음을 배웠었어요. 오빠 덕분에 제가 많이 성장할 수 있었답니다. 많이 고마웠어요. 나의 동기들~ 태효미, 씸빰^^ 이젠 어엿한 정출연 박사님이 되셨지만,,,태효오빠는 내겐 영원한 태효미, 그리고 내게 복음을 전해준 영혼의 은인 씸빰.너와 UNIST에서 함께했던 시간은 몹시 짧았지만, 내 인생에 너가 전해준 보석은 그 무엇보다 크구나. 정말 정말 고맙고 애정해요 내 동기들♡. 다음으론 나의 입학 후배이자 졸업 선배님들^^ 무엇이든 물어보면 친절히 답해주는 엔젤의 검색엔진 학범오빠, 항상 밝고 씩씩한 긍정의 에너지로 동생이지만 언니처럼 날 끌어주는 세영이, 묵묵히 할 일을 하지만 마음을 따뜻하게 만들어주는 재기오빠, 센스와 재치를 겸비한 말들로 무엇이든 친절히 도와주는 똑똑이 정우, 조용히 자기 할 일을 척척해 내는 택호, 선배들에게도 후배들에게도 참 잘하고 일도 잘하는 다재다능한 송이까지. 여러분 덕분에 저 졸업합니다~^^ 마지막으로 나의 귀여운 후배님들, 이젠 귀엽다고 하기엔 나이가 꽤 들어버린 후배들 강택, 영진, 나경, 함께 졸업하게 되어 영광입니다 ^^ NGEL의 웃음바이러스 재원이 항상 우리를 유쾌하게 만들어줘서 고맙다, 묵묵히 궂은일을 도맡아 하는 형수, 뒤에서 남몰래 누나를 응원하고 있었다는 말로 누나 맘 따뜻하게 해주었던 귀여운 윤섭이 힘들 때 많이 힘이 되었었어 고맙다, 힘든 순간 묵묵히 잘 견뎌주고 폴리머 팀에 중심이 되어주어서 고마운 혜원이, 무엇이든 넵! 하고 잘 따라와주는 귀염둥이 폴리머팀 누나들의 우리지우, 육아하면서 학위하기 많이 힘들지…그래도 잘하고 있다 화이팅이다 종득아, NGEL의 막둥이들 우진, 도훈, 중건, 찬범, 현서, 진희, 태희까지.

감사의 글을 적으려 지난 10년을 가만히 뒤돌아보니, NGEL은 저를 많이 성장하게 해준 든든한 집과 같았고, 실험실 사람들은 제게 그런 성장을 함께 해주는 식구들이었습니다. 몇달 후면 NGEL을 떠날 생각을 하니 만감이 교차한다는 말이 뭔 지 정확히 알 것만 같습니다. 늘 우리 교수님이, 우리 NGEL 식구들 모두가 잘 되었으면 좋겠습니다. NGEL을 떠나서도 NGEL을 생각하며

기도하겠습니다.

특별히 다시한번, 여러 번의 휴.복학으로 감 못 잡고 헤맬 때, 그때마다 큰 도움 주었던 명희언니, 세영이, 정우, 송이, 나경이 모두모두 정말 고마워요^^ 참 손이 많이 가는 아줌마였는데, 다들 싫은 내색 한번없이 친절하게 제 일처럼 마음 써주고 함께 해줘서 모든 학위 마무리 지을 수 있었습니다 ^^♡

사랑하는 우리 가족들에게 역시 깊은 감사의 마음을 전하고 싶습니다.

먼저는 낳아주고 길러준 우리 엄마, 아빠, 감사해요. 아이를 낳고 보니 이만큼 사람을 길러낸다는 것이 얼마나 큰 희생이 필요하고 어려운 일이라는 걸 알게 되었어요. 어릴 적부터 꾸었던 과학자의 꿈을 이룰 수 있게 응원해주고 지지해 주셔서 감사해요. 사랑해요.

저의 또 하나의 부모님 울 어무니 아부지, 정말 감사해요. 어린 저를 길러주신 건 저의 부모님이 셨지만, 지금의 저를 만들어 주신 건 두분 이세요. 두 분을 뵈며 저렇게 살아야지, 저런 부모가 되어야지 많이 배우고 늘 힘을 얻습니다. 학위 기간 내내 모든 부분에서 망설임없이 도움을 주셨던 어무니 아부지 정말 정말 감사드려요. 어무니 아부지 덕분에 수아도 은우도 이만큼 키울 수 있었고, 수아아빠도, 저도 학위 무사히 잘 마칠 수 있었습니다. 그리고, 미라언니 늘 예쁜 미소 예쁜 말로 좋은 누나 좋은 고모 되어 주셔서 감사해요. 사랑합니다.

사랑하는 여보♡ 고마워요. 언제나 나의 든든한 울타리와 버팀목이 되어주는 당신.
내가 몇 번이나 학위 포기하겠다고 할 때마다 어르고 달래 주고 기도해준 덕분에 지금까지 올 수 있었네.. 여보도 나랑 똑같이 학위하며 육아하며, 취업하며, 많이 힘들었을텐데, 힘든 내색 안하고 항상 밝은 모습으로 “아~ 좋다. 아~ 감사하다.” 라고 이야기하며 긍정의 에너지를 주는 당신♡ 진짜 당신 아니었음 이 모든 것 못 해 냈을 거야. 정말 고마워요. 매일 어제보다 오늘 더 사랑할께.

마지막으로 엄마의 보물들 조수아 조은우♡ 공부중에 수아랑 은우를 얻어 엄마로 학생으로 동시에 살아내느라 힘든 순간도 있었지만, 우리 딸 아들의 엄마로 살아내면서 누리는 행복과 기쁨이 훨씬 컸기에 너네는 엄마에게 이 공부를 끝까지 마칠 수 있게 해준 힘이 되었단다 ^^ 엄마가 공부하는 엄마라 온전히 함께 못 있어줄 때도 많았는데, 우애 좋게 건강하게 바르게 잘 자라줘서 고마워♡ 이제 엄마랑 더 실컷 많~이 놀자 ^^ 사랑한다 우리 아가들♡

이 밖에도 조인규초원지기님, 이영엽목녀님, 승진언니, 언식오빠, 이니언니, 목장식구들(한별오빠, 이래언니, 태우오빠, 정혜, 지윤이, 희정이, 정수오빠, 선영이, 희영언니, 나경언니, 수연이, 충선오빠, 아림언니, 혜승이), 초원식구들을 비롯하여, 함께 연구했던 김이호차장님, 경식오빠, 보람이, 룸메 지연이, 호정이, 매주 수요일 함께 찬양했던 현진쌤, 지혜쌤, 그리고 지혜언니와 예나네 가족들까지..

많은 분들의 도움이 있었기에 이렇게 박사학위를 받을 수 있었습니다.

다시 한번 진심으로 감사드립니다.